Insights into active site structures for Pd-based bimetallic heterogeneous catalysts

By

Madelyn R. B. Ball

A dissertation submitted in partial fulfillment of
the requirements of the degree of

Doctor of Philosophy
(Chemical Engineering)

at the
UNIVERSITY OF WISCONSIN-MADISON
2019

Date of final oral examination: 6/10/2019

The dissertation has been approved by the following members of the Final Oral Committee:

James A. Dumesic, Professor, Chemical and Biological Engineering
Ive Hermans, Professor, Chemistry
George W. Huber, Professor, Chemical and Biological Engineering
David M. Lynn, Professor, Chemical and Biological Engineering

Insights into active site structures for Pd-based bimetallic heterogeneous catalysts

Madelyn R. B. Ball

Under the supervision of Prof. James A. Dumesic at the University of Wisconsin-Madison

Abstract

Catalytic reactions play a large role in the production of energy and products used in our modern society. In order to improve the efficiency of existing processes and make the conversion of new feedstocks, such as biomass and natural gas, possible, there exists the need for improved catalytic materials. Many active catalysts have complex active sites containing multiple components; therefore, fundamental understanding of active sites and structure-performance relationships is needed to rationally design new catalysts. The work in this dissertation is focused on catalytic synthesis of well-controlled bimetallic catalysts in order to develop structure-activity and structure-selectivity relations for different chemical transformations. A controlled surface reaction synthesis approach is used to deposit Pd onto Au, Ag, or Cu parent catalysts. These Pd bimetallic catalysts are then studied for reactions where selectivity is a main challenge, and the selective Pd structure is identified.

First, AuPd/TiO_2 catalysts are studied for the gas phase amination of 1-hexanol using ammonia. It was determined via chemisorption, X-ray absorption spectroscopy (XAS), energy dispersive X-ray spectroscopy (EDS), and CO infrared spectroscopy (FTIR) analysis that there are no monometallic Pd structures on the catalysts. The Pd atoms are well diluted in the Au nanoparticles at low loadings and as the Pd loading increases, more contiguous Pd sites are formed. From reactivity studies, it is determined that both the Au and Pd contribute to the overall hexanol conversion, however the activity in enhanced for the bimetallic catalysts compared to the monometallic catalysts. This rate improvement is attributed to a geometric effect where surface intermediates are not stabilized by hydrogen bonding to adsorbed ammonia in close proximity. Furthermore, the selectivity to primary amines is increased as the loading of Pd increases

in the AuPd catalysts, while lower Pd loadings favor more substituted products. The selectivity trends are hypothesized to be related to both geometric and electronic effects present in the AuPd catalyst system.

Next, AgPd catalysts were studied for the hydrodechlorination of 1,2-dichloroethane. The role of the support in the formation of well-controlled bimetallic nanoparticles was investigated and it was determined that well-mixed AgPd particles were formed on a TiO_2 support, while some monometallic Pd particles were also formed on C and SiO_2 supports. Again, using chemisorption, XAS, and CO-FTIR, it was determined that isolated Pd atoms within the Ag nanoparticles are formed on the TiO_2 support at low loadings. On the SiO_2 supported catalysts, contiguous Pd species are formed. The isolated Pd species are highly selective to ethylene while the contiguous Pd species are selective to the undesired ethane. Thus, the support was determined to play an important role in tuning the AgPd structure and the resulting selectivity for hydrodechlorination. The rate of 1,2-dichloroethane conversion was determined to be related to the selectivity, with the ethylene selective catalysts exhibiting the highest turnover frequencies. Thus, controlled surface reactions on different supports were used to create catalysts with a range of surface structures to investigate the desired structure for selective hydrodechlorination.

Finally, AgPd and CuPd catalysts were investigated for the selective hydrogenation of acetylene. Both TiO_2 and SiO_2 supported catalysts were studied, and it was determined by EDS analysis that the CuPd nanoparticle composition distribution was more uniform on the SiO_2 support than on the TiO_2 support. Infrared spectroscopic studies were used to characterize the catalyst surfaces in the presence of different adsorbates. From CO-FTIR, the bimetallic catalysts adsorb CO on atop sites which suggest Pd present in isolated species, diluted by the Ag or Cu parent. However, in FTIR studies of adsorbed ethylene, the presence of di-σ-bonded ethylene is observed which requires neighboring Pd atoms. IR spectra of the catalyst surface after being exposed to reaction conditions indicate the presence of numerous spectator species and it is determined that there are less sites covered by spectators for the bimetallic catalysts compared to a monometallic Pd catalyst. On the TiO_2 support, the bimetallic catalysts exhibit the highest rates per gram of Pd and high ethylene selectivites above 99%. The monometallic catalysts are less than 95% selective to ethane, indicating that the alloy formation improves the ethylene selectivity; the enhanced

selectivity is attributed to electronic effects in the bimetallic nanoparticles. Thus, the investigation of Pd bimetallic catalysts with Au, Ag, or Cu, synthesized by a controlled surface reaction approach facilitated the development of structure-activity and structure-selectivity relationships for different catalytic reactions.

This work enabled the development of detailed active site hypotheses for different Pd based bimetallic catalysts and provided insights into the desired structures to inform rational catalyst design. The controlled surface reaction synthesis approach and general characterization methodology can be applied to a broad range of catalyst and reaction systems to improve chemical transformations for improved production of chemicals and fuels for modern society.

Acknowledgements

There are many people to whom I owe immense gratitude – without their support, I would not be where I am today. First, I want to acknowledge my advisor, Prof. James Dumesic. It has been an honor to be a part of his research group and I am grateful for all the opportunities he has given me to learn and explore different aspects of catalysis research. His mentorship, brilliance, passion, and confidence in me have helped me to become a successful researcher and I cannot thank him enough for that. He taught me how to approach research with the right questions, starting from the fundamentals and that with the right enthusiasm you can end up with a few more answers than questions. These last years have been truly enjoyable because of his guidance and I know that I will take the many lessons I have learned from him every step forward in my career.

I also want to thank Prof. George W. Huber, Prof. Manos Mavrikakis, Prof. Ive Hermans, Prof. Christos Maravelias, Prof. David Lynn, and Prof. Brian Pfleger for their mentorship and for serving on my committees over these years. I have learned so much from being a part of the collaborative catalysis community at UW and am grateful for having so many trusted mentors. I am also grateful for the work and support from Dr. Eric Stangland at Dow who made the dechlorination study possible.

I also want to thank all the past and current Dumesic group members for their support, guidance, and friendship over these past five years. In particular, I am very grateful to Prof. Tom Schwartz for his guidance on a variety of lab techniques and for teaching me to “not ask questions you don’t want the answer to.” I am immensely thankful for Prof. Ana Alba-Rubio in passing on her expertise about the microscope and many enjoyable hours in doing so. I would also like to thank both Tom and Ana for sharing their perspectives about academic life. I want to thank Dr. Ronald Carrasquillo-Flores for his willingness to teach me the basics when I first joined the group and immense patience in doing so, Dr. Canan Sener for her immense knowledge about catalyst synthesis, Dr. Max Mellmer for his help with presentations and reminding me not to take anything too seriously, and Dr. Zach Brentzel for his help with flow reactors and great friendship. I also want to thank Dr. Insoo Ro for many enjoyable collaborations (even when they involved fixing vacuum systems), Dr. Mrunmayi Kumbhalkar for her scientific guidance and friendship, and Keishla Rivera-Dones for being willing and excited to attempt XAS with me. I have been so grateful to be surrounded by people who make every day enjoyable and want to thank Dr. Yifei Liu, Dr. Ali Hussain Motagamwala, Dr. Duygu Gerceker, Dr. David Martin Alonso, Dr. Victor Freitas, Dr. Isaias Barbosa Arago, Dr. Tony Plauck, Dr. Lang Xu, Siddarth Krishna, Lifeng Zhang, Bengi Demir, Elise Gilcher, Hochan Chang, Leida Vasquez-Ramos, and Dr. Dan McClelland for all of their advice, guidance, and discussions over these past years. I also want to thank the many undergraduate and high school students who put in many hours to make my work possible: Kindle, Rice, Lupe, Edgard, Sam, Cole, Cammy, and Meghana. Being able to mentor such enthusiastic students is a large part of why I want to continue in academia.

I want to give special thanks to Judy Lewison who keeps the Dumesic group running and has been a great source of support over these past five years (and keeps us all fed with her delicious baked goods!). I also am immensely grateful for all of the CBE department staff, in particular Dr. Eric Codner for his immense technical knowledge and willingness to help troubleshoot equipment as well as Steve Schumacher for his craftsmanship on many pieces of equipment. I also want to thank Kathy Heinzen, Kate Fanis, Russ Poyner, and Lynn Robinson.

I am very grateful to have an amazing, supportive group of people outside of lab that have made my time in Madison so enjoyable. Many thanks to Nat, Kayla, Siddarth, Hugh, Peter, Emily, Elise, and Sarah for many great adventures!

I am so incredibly grateful for the love and support that my family has given me over the years. From a young age, my parents instilled an excitement for science in me and it is because of their encouragement that I am here today. My mom in particular has been an incredible role model for me, helping me to find chemical engineering in the first place and then encouraging me to explore research and eventually pursue my Ph.D. She has been an amazing example of how to thrive as a woman in engineering and inspires me to be a mentor and role model in my own career. I am without a doubt where I am today because of my parents' guidance and the opportunities they provided for me and I am so thankful for all that they have done for me.

And finally, I want to thank Juan for being my foundation and for bringing so much joy to my life. His drive and passion for science are contagious and he inspires me to be a better scientist and a better person each and every day. I cannot imagine having gone through the past five years without him by my side and am so grateful for his unending support through both the challenges and the successes that come with research. It has been an incredible journey and I am so excited for our future together.

Table of Contents

List of Figures

List of Tables

Chapter 1. Introduction

1.1 Motivation

Catalytic reactions play a vital role in the production of fuels and chemicals for our growing world, enabling the transformation of both fossil and renewable resources into valuable goods and energy sources. Around 90% of chemical processes use catalysts[1] and over 80% of all manufactured products involve catalysis at some point in their processing.[2] Catalytic processes also play a major role in the world economy with estimates predicting that catalysis contributes to more than 35% of global GDP.[1] The scale of the chemical industry as a whole and, in particular, processes involving catalysts, indicate the importance of developing effective catalytic materials for a range of transformations. As an example, the Haber-Bosch process enabled the production of ammonia from hydrogen and nitrogen over an iron based catalyst and its subsequent use in synthetic fertilizer led to the growth of the world population to its current levels.[3–5] Additionally, both the selective catalytic reduction of NO_x over Cu zeolite catalysts to remove hazardous nitrogen oxides from automotive exhaust[6,7] and the catalytic cracking of petroleum to form gasoline and other fuel products[8,9] enable the ease of transportation in our modern society. These processes, among many others, are used to meet the global demands for fuels and chemicals. As our population continues to grow and the standard of living improves for the billions of people on the planet, the demands for these products will continue to increase. Thus, there exists motivation to improve the efficiency and feasibility of the conversion of a broad range of resources. One avenue through which the transformation of raw feedstocks and platform molecules into valuable products can be enhanced is through catalyst improvement and new catalyst development.

In particular, we aim to improve the activity, selectivity, and stability of catalytic materials for various transformations. The development of new catalysts for chemical transformations, however, is hindered by system complexity. Many state-of-the-art catalysts involve numerous components and promoters and are often identified by trial and error approaches. In order to identify appropriate and improved catalysts for various chemical conversions, we aim to develop detailed structure-activity relationships. By elucidating the controlling factors of catalyst performance, we can work to design the best catalyst structure for a particular transformation. The ability to rationally design catalysts for any given reaction would facilitate important improvements to reactions for energy, chemical, and environmental applications.

In order to understand the relationship between catalyst structure and performance, it is crucial to understand what the active site of the catalyst is for a given reaction. With an understanding of the active site, synthetic methods can then be developed to create a catalyst with the desired structures. The aim of identifying the particular nature of active sites in heterogeneous catalysts has been a topic of discussion for many decades.[10] For transition metal catalysts, nanoparticles have a number of terrace surfaces, steps, and edges that comprise the active surface and the total number of active sites can often be approximated as the total number of binding sites for a probe molecule such as CO. This is not always the case, however, as has been determined for Au catalysts for formic acid decomposition[11] and Cu catalysts for methanol synthesis,[12] as well as other systems that bind species weakly. Based on Sabatier's principle, the best catalyst for a given reaction will bind the reactive species neither too weakly nor too strongly. For metals such as Au, the active sites for many reactions have been determined to be the most undercoordinated sites at the steps and edges of nanoparticles. For metals such as Pt and Pd, however, actives sites often bind species too strongly, leading to deactivation. By understanding what the ideal binding strength of key intermediates are, catalyst changes can be applied such that the binding strength of intermediates on the metals is modulated. Changes can be induced in a variety of ways, such adding a second metal, promoters, or support which interact with the metal[13] and as a result, catalyst activity can be modified.

These catalyst modifications, while they offer improved performance and are widely used in a range of industrial processes, make the identification of the active site more complicated. Without a fundamental understanding of the active site, iteratively improving the catalyst further remains challenging. In some cases, the assumed catalytic active site may remain the same, but a particular step of the overall reaction takes place on the promoting material. This is the case for the water gas shift reaction over PtMo catalysts, where water and hydroxyl species are stabilized on the promoting Mo while CO binding occurs on Pt.[14] In Fisher-Tropsch synthesis, for example, Na_2S promoted iron carbide catalysts have increased olefin production and decreased methane production due to an increase in adsorption of reactive intermediates on iron sites rather than carbon sites.[15] In other catalyst systems, however, both the components may be active and therefore the definition of the active site must include both species. For example, CuCo catalysts have been studied for alcohol synthesis processes which combine a methanol synthesis copper catalyst with a Fischer-Tropsch cobalt catalyst.[16] Since both components are used as catalysts on their own, both should be considered in the active site definition. It is also possible for interfaces between catalyst components to act as active sites for 2nd order reaction steps where intermediates adsorbed on the different components react.[17] Thus, the range of mechanisms through which catalyst promoters modify the active sites involved in these chemical transformations and enhance the reactivity are diverse. In this work, the focus will be on the use of bimetallic catalysts to change interactions between reactive species and a catalyst surface in advantageous ways.

1.2 Bimetallic Catalysts

Heterogeneous, bimetallic catalysts often provide improved activity, selectivity, and stability compared to their monometallic counterparts.[18] In order to understand these enhancements, two primary effects are reported – ensemble effects and electronic effects.[19] Ensemble, or geometric, effects refer to the arrangement of atoms in a bimetallic structure. For example, the improved selectivity to hexenes in the hydrogenation of hexyne over PdAu catalysts was attributed to the isolation of Pd atoms in a Au matrix.[20] Additionally, it has been reported that contiguous Pd atoms may be required for CO oxidation over AuPd catalysts but that the spillover of atomic oxygen from Pd to Au sites decreases the temperature required for the reaction to take place.[21] Pt atoms, atomically dispersed in a Cu matrix have been shown to be active for the water gas shift reaction and the activity is attributed to the ability for the interface between the copper oxide support and Pt atoms to dissociate water.[22] Thus, the specific geometric requirements for a catalyst depend on the chemistry involved.

Electronic, or ligand, effects refer to the transfer of partial charge between two metals in a system or rehybridization of orbitals of one or both metals, changing the electron density of the active sites.[18,23] As an example, in layered PdCu catalysts, charge transfer between the metals is measured and determined to increase as the Pd thickness is increased. This electronic effect increased the stability of the catalysts for electrochemical formic acid oxidation.[24] Electronic effects have also been discussed by comparing the dissolution of hydrogen on Pd and Pd_3Fe alloys.[25–27] Although the environment of H on a Pd_6 site in the alloy appears identical to a H atom on a monometallic Pd site, the enthalpy of dissolution on the alloy is more than 30 kJ/mol higher, indicating that the density of states is changed such that interaction with H is greatly weakened. Also, for hydrogenolysis chemistry, it is suggested that the neighboring atoms to the active site are critical to the electronic properties of the active site itself. For ethane to bind to a Ni dimer site, the neighboring atoms must also be Ni; if the near neighboring atoms are replaced by Cu, strong bonds between the ethane C and Ni cannot be formed and the hydrogenolysis activity decreases.[25] Thus, the catalytic activity is modulated by the change in electron density of the Ni site due to the bimetallic nature of the surrounding catalyst.

It is also important to note that although either geometric or electronic effects may dominate over one another for a given system, it is typically not possible to change either structure of the metals in a bimetallic system without changing the other.[28] In a number of cases, improved catalytic performance for bimetallic systems is attributed to both electronic and geometric effects,[25] including CO oxidation[29,30] and direct synthesis of hydrogen peroxide[31–34] over AuPd catalysts. Additionally, density functional theory calculations have been used to deconvolute the effects of electronic and ensemble effects by considering a number of adsorption structures on several surface compositions.[35] On Au/Pd(111) surfaces, the adsorption energy of CO on the top of Pd atoms was measured as the surrounding atoms were changed, thus quantifying the electronic effect of the AuPd bimetallic system. Subsequently, the adsorption site was changed, measuring CO adsorption energy on top, hollow, and bridge sites, and then the electronic effect was subtracted to measure the influence of the geometric effect alone on CO adsorption energies. Using this approach, it was concluded that CO adsorption is influenced by both electronic and geometric factors on bimetallic AuPd surfaces. Thus, as bimetallic catalysts are studied more broadly, the relative roles of both electronic and geometric modifications to the active sites must be considered in rational design of catalytic structures.

Bimetallic catalysts can be synthesized in a variety of ways, resulting in a number of different morphologies. Incipient wetness impregnation and wet impregnation are often used due to their simple procedure but typically result in nanoparticles with a broad size and composition distribution.[36,37] Strong electrostatic adsorption offers improved control over the nanoparticle size and composition by using the differences in surface potential between the support and metal oxides at a range of pH values.[38] Colloidal and sol gel techniques also offer more control over the nanoparticle size, and can even yield shape specific nanocubes or nanooctahedra, however structure directing agents are necessary and can be challenging to remove after synthesis.[39,40] Atomic layer deposition has been used for well controlled formation of bimetallic catalysts and can form core shell as well as well mixed nanoparticles.[41–43] From the variety of synthesis approaches, the resulting structure of a bimetallic nanoparticle depends on many factors, including the surface energies of each of the elements, the relative atomic size of each component, and the strength of binding to various surface species.[44] Figure 1.1 shows example cross section structures of nanoparticles that can be formed for bimetallic systems, including core-shell and well mixed structures.

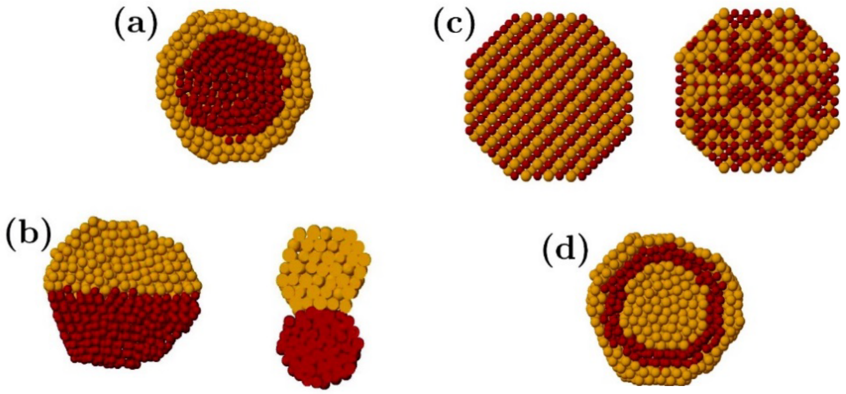

Figure 1.1. Schematic of possible bimetallic nanoparticle structures, including (a) core-shell, (b) segregated clusters, (c) mixed, and (d) multiple shell. This figure was reproduced with permission from Reference 44. Copyright 2008 American Chemical Society.

Among bimetallic catalysts, Pd-based catalysts are widely used for a variety of chemical transformations. The broad scope of reactions that are catalyzed by Pd-containing systems originate from the high activity of Pd as a transition metal, coupled with advantageous electronic and/or geometric effects from the second metal. Alone, Pd is an active catalyst for hydrogenation,[45,46] carbon-carbon coupling,[47,48] and oxidation reactions.[49,50] These reactions are often enhanced by the addition of a second metal, such as the addition of silver, tin, or gold for hydrogenation chemistry[51,52] and addition of gold for oxidation reactions.[53–56] Both vinyl acetate synthesis[57–59] and low temperature CO oxidation[18,21,60,61] are enhanced over AuPd surfaces. Bimetallic Pd systems enhance the selectivity to desired products for aldehyde hydrogenation[62] and direct synthesis of hydrogen peroxide.[63,64] Thus it is well established that Pd catalysts, promoted by another metal, have advantageous catalytic properties for a wide scope of chemical transformations.

In order to inform the rational design of catalysts to improve different reactions, it is important to understand what the active site on these bimetallic catalysts is. Thus, synthesizing catalysts with a uniform distribution of structures can facilitate the elucidation of catalytic active sites for multi-component materials. This is a key challenge in the field of catalysis that this work aims to address.

1.3 Dissertation Scope

The work reported in this dissertation aims to use Pd based bimetallic catalysts, synthesized in a well-controlled manner, to develop fundamental structure-activity and structure-selectivity relationships. The controlled surface reaction synthesis approach deposits Pd onto a parent metal catalyst to facilitate its uniform deposition. A range of *in situ* and *ex situ* characterization techniques are applied in order to understand the catalyst structure both as synthesized and under reaction conditions. These Pd-based catalysts are studied for three reactions of industrial relevance and the origins of improved performance are explored for each system, as compared to monometallic catalysts.

Chapter 2 will first outline the catalyst synthesis and characterization techniques used throughout this work. The controlled surface reaction approach to synthesizing Pd-containing bimetallic catalysts is discussed and the characterization techniques which allow us to confirm the bimetallic nature of the catalysts and describe the surface structures are detailed.

In Chapter 3, the use of AuPd catalysts for the amination of 1-hexanol is discussed. In this example, both the Au and Pd species are active for the catalytic conversion, however an enhanced rate is observed over the bimetallic system and is attributed to primarily ensemble effects. STEM-EDS analysis is used to confirm the uniform, bimetallic nature of the catalysts. FTIR studies of adsorbed CO on the catalysts indicate that both electronic and geometric effects may be present in the AuPd system, where Pd is diluted in the Au nanoparticle and the strength of CO binding to the Pd sites is altered. The changes in selectivity to amine products as the Au:Pd ratio is altered are studied and it is determined that the formation of primary amine products is enhanced at higher Pd ratios. At lower Au:Pd ratios, as Pd is increasingly diluted in Au, the selectivity to 2° and 3° amines increases. This work also demonstrates the challenges in identifying the proper active site for rate normalization when both components of a bimetallic catalyst system are independently active.

In Chapter 4, AgPd catalyst systems are studied for the hydrodechlorination of 1,2-dichloroethane. The role of the support in the synthesis of uniform bimetallic nanoparticles is investigated and determined that AgPd structures can be most effectively formed on a TiO_2 support. The uptake of Pd onto the support is measured using UV vis spectroscopy and determined to be dependent on the concentration used during synthesis. X-ray absorption spectroscopy is used to qualitatively measure the degree to which the Ag and Pd are well mixed in the nanoparticles. Using CO chemisorption and FTIR studies, it is determined that the Pd in the AgPd/TiO_2 catalyst is primarily isolated from other Pd atoms and these structures are highly selective to the desired ethylene. On the SiO_2 support, contiguous Pd species are formed and these structures are selective to the undesired ethane. Thus, by synthesizing a range of Pd-containing bimetallic structures, the selectivity to the desired product can be tuned.

Then, in Chapter 5, AgPd and CuPd catalysts are studied for the selective hydrogenation of acetylene. Similarly, CO adsorption is used to characterize the Pd surface structure, and it is determined that by alloying Pd with either Ag or Cu, the Pd species are isolated from each other. FTIR studies were also expanded to investigate the adsorption of ethylene as well as the reaction mixture of ethylene, acetylene, and hydrogen. It was determined that ethylene, ethylidyne, and vinylidene species are present as spectator species under reaction conditions on the monometallic Pd catalysts and that the coverage of these species is decreased on the bimetallic catalysts. Both AgPd and CuPd catalysts achieve nearly 100% selectivity to ethylene at low conversion. The measured activity of the AgPd catalysts, however, is greater than that of the CuPd catalysts. The differences in acetylene conversion rate are attributed to the differences in Pd dispersion and the distribution of Pd between the surface and bulk of nanoparticles between the two bimetallic systems. This work highlights the importance of understanding the catalyst surface under reaction conditions, as the presence of adsorbates can change the surface structure and therefore the active site structure.

Chapter 6 summarizes the main conclusions from this work and discusses implications of these results, as well as future research directions in the area of well-controlled bimetallic catalysts. By synthesizing catalysts in a well-controlled manner, relationships between the structure, both as synthesized and under relevant reaction conditions can be determined. This fundamental understanding of catalyst active sites can inform the improved design and synthesis of new catalytic materials.

1.4 References

(1) Catalysis Helps Society Do More With Less http://www.americanchemistry.com/Catalysis-Roadmap.

(2) Catlow, C. R. A.; Davidson, M. G.; Hardacre, C.; Hutchings, G. J. *Philos. Trans. R. Soc. A Math. Phys. Eng. Sci.* **2016**, *374*, 20150358.

(3) Hagen, J. *Industrial Catalysis*; Wiley-VCH Verlag GmbH & Co. KGaA, 2015.

(4) Smil, V. *Nature* **1999**, *400*, 415.

(5) Erisman, J. W.; Sutton, M. A.; Galloway, J.; Klimont, Z.; Winiwarter, W. *Nat. Geosci.* **2008**, *1*, 636–639.

(6) Kwak, J. H.; Tonkyn, R. G.; Kim, D. H.; Szanyi, J.; Peden, C. H. F. *J. Catal.* **2010**, *275*, 187–190.

(7) Paolucci, C.; Khurana, I.; Parekh, A. A.; Li, S.; Shih, A. J.; Li, H.; Di Iorio, J. R.; Albarracin-Caballero, J. D.; Yezerets, A.; Miller, J. T.; Delgass, W. N.; Ribeiro, F. H.; Schneider, W. F.; Gounder, R. *Science (80-.).* **2017**, *357*, 898–903.

(8) Lewis, W. K.; Gilliland, E. R. Conversion of hydrocarbons with suspended catalyst. 2498088, 1950.

(9) Vogt, E. T. C.; Weckhuysen, B. M. *Chem. Soc. Rev.* **2015**, *44*, 7342–7370.

(10) Nørskov, J. K.; Bligaard, T.; Hvolbæk, B.; Abild-Pedersen, F.; Chorkendorff, I.; Christensen, C. H. *Chem. Soc. Rev.* **2008**, *37*, 2163.

(11) Singh, S.; Li, S.; Carrasquillo-Flores, R.; Alba-Rubio, A. C.; Dumesic, J. A. **2014**, *60*, 1303–1319.

(12) Chinchen, G. C.; Waugh, K. C.; Whan, D. A. *Appl. Catal.* **1986**, *25*, 101–107.

(13) Motagamwala, A. H.; Ball, M. R.; Dumesic, J. A. **2018**, 1–38.

(14) Sener, C.; Wesley, T. S.; Alba-Rubio, A. C.; Kumbhalkar, M. D.; Hakim, S. H.; Ribeiro, F. H.; Miller, J. T.; Dumesic, J. A. *ACS Catal.* **2016**, *6*, 1334–1344.

(15) Xie, J.; Yang, J.; Dugulan, A. I.; Holmen, A.; Chen, D.; De Jong, K. P.; Louwerse, M. J. *ACS Catal.* **2016**, *6*, 3147–3157.

(16) Xu, X. C.; Su, J.; Tian, P.; Fu, D.; Dai, W.; Mao, W.; Yuan, W. K.; Xu, J.; Han, Y. F. *J. Phys. Chem. C* **2015**, *119*, 216–227.

(17) Andersen, M.; Medford, A. J.; Nørskov, J. K.; Reuter, K. *ACS Catal.* **2017**, *7*, 3960–3967.

(18) Gao, F.; Goodman, D. W. *Chem. Soc. Rev.* **2012**, *41*, 8009.

(19) Sinfelt, J. H. *Acc. Chem. Res.* **1977**, *10*, 15–20.

(20) Liu, J.; Shan, J.; Lucci, F. R.; Cao, S.; Sykes, E. C. H.; Flytzani-Stephanopoulos, M. *Catal. Sci. Technol.* **2017**, *7*, 4276–4284.

(21) Gao, F.; Wang, Y.; Goodman, D. W. *J. Am. Chem. Soc.* **2009**, *131*, 5734–5735.

(22) Therrien, A. J.; Groden, K.; Hensley, A. J. R.; Schilling, A. C.; Hannagan, R. T.; Marcinkowski, M. D.; Pronschinske, A.; Lucci, F. R.; Sykes, E. C. H.; McEwen, J.-S. *J. Catal.* **2018**, *364*, 166–173.

(23) Kugler, E. L.; Boudart, M. *J. Catal.* **1979**, *59*, 201–210.

(24) Hu, S.; Scudiero, L.; Ha, S. *Electrochim. Acta* **2012**, *83*, 354–358.

(25) Burch, R. *Acc. Chem. Res.* **1982**, *15*, 24–31.

(26) Flanagan, T. B.; Majchrzak, S.; Baranowski, B. *Philos. Mag.* **1972**, *25*, 257–262.

(27) Carlow, J. S.; Meads, R. E. *J. Phys. F Met. Phys.* **1972**, *2*, 982–984.

(28) Kitchin, J. R.; Nørskov, J. K.; Barteau, M. A.; Chen, J. G. *Phys. Rev. Lett.* **2004**, *93*, 4–7.

(29) Gao, F.; Wang, Y.; Goodman, D. W. *J. Am. Chem. Soc.* **2009**, *131*, 5734–5735.

(30) Xu, J.; White, T.; Li, P.; He, C.; Yu, J.; Yuan, W.; Han, Y. *J. Am. Chem. Soc.* **2010**, *132*, 10398–10406.

(31) Ouyang, L.; Da, G.; Tian, P.; Chen, T.; Liang, G.; Xu, J.; Han, Y.-F. *J. Catal.* **2014**, *311*, 129–136.

(32) Ham, H. C.; Hwang, G. S.; Han, J.; Nam, S. W.; Lim, T. H. *J. Phys. Chem. C* **2007**, *42*, 1465–1469.

(33) Menegazzo, F.; Signoretto, M.; Manzoli, M.; Boccuzzi, F.; Cruciani, G.; Pinna, F.; Strukul, G. *J. Catal.* **2009**, *268*, 122–130.

(34) Edwards, J. K.; Pritchard, J.; Piccinini, M.; Shaw, G.; He, Q.; Carley, A. F.; Kiely, C. J.; Hutchings, G. J. *J. Catal.* **2012**, *292*, 227–238.

(35) Liu, P.; Nørskov, J. K. *Phys. Chem. Chem. Phys.* **2001**, *3*, 3814–3818.

(36) Tengco, J.; Tavakoli Mehrabadi, B.; Zhang, Y.; Wongkaew, A.; Regalbuto, J.; Weidner, J.; Monnier, J. *Catalysts* **2016**, *6*, 83.

(37) Liu, J.; Tao, R.; Guo, Z.; Regalbuto, J. R.; Marshall, C. L.; Klie, R. F.; Miller, J. T.; Meyer, R. J. **2013**, 3665–3672.

(38) D’Souza, L.; Regalbuto, J. R. *Stud. Surf. Sci. Catal.* **2010**, *175*, 715–718.

(39) Lyu, Z.; Xie, M.; Aldama, E.; Zhao, M.; Qiu, J.; Zhou, S.; Xia, Y. *ACS Appl. Nano Mater.* **2019**, *2*, 1533–1540.

(40) Gu, J.; Zhang, Y. W.; Tao, F. *Chem. Soc. Rev.* **2012**, *41*, 8050–8065.

(41) Lu, J.; Low, K.-B.; Lei, Y.; Libera, J. A.; Nicholls, A.; Stair, P. C.; Elam, J. W. *Nat. Commun.* **2014**, *5*, 3264.

(42) Weber, M. J.; MacKus, A. J. M.; Verheijen, M. A.; Van Der Marel, C.; Kessels, W. M. M. *Chem. Mater.* **2012**, *24*, 2973–2977.

(43) Singh, J. A.; Yang, N.; Liu, X.; Tsai, C.; Stone, K. H.; Johnson, B.; Koh, A. L.; Bent, S. F. *J. Phys. Chem. C* **2018**, *122*, 2184–2194.

(44) Ferrando, R.; Jellinek, J.; Johnston, R. L. *Chem. Rev.* **2008**, *108*, 845–910.

(45) Gonzo, E. E.; Boudart, M. *J. Catal.* **1978**, *52*, 462–471.

(46) Borodzinski, A. *Catal. Letters* **1999**, *63*, 35–42.

(47) Yin, L.; Liebscher, J. *Chem. Rev.* **2007**, *107*, 133–173.

(48) Molnár, Á. *Chem. Rev.* **2011**, *111*, 2251–2320.

(49) Hackett, S. F. J.; Brydson, R. M.; Gass, M. H.; Harvey, I.; Newman, A. D.; Wilson, K.; Lee, A. F. *Angew. Chemie - Int. Ed.* **2007**, *46*, 8593–8596.

(50) Savara, A.; Rossetti, I.; Chan-Thaw, C. E.; Prati, L.; Villa, A. *ChemCatChem* **2016**, *8*, 2482–2491.

(51) El Kolli, N.; Delannoy, L.; Louis, C. *J. Catal.* **2013**, *297*, 79–92.

(52) Sales, E. A.; Jove, J.; Mendes, M. D. J. **2000**, *95*, 88–95.

(53) Lee, A. F.; Ellis, C. V.; Wilson, K.; Hondow, N. S. *Catal. Today* **2010**, *157*, 243–249.

(54) Rodriguez, A. A.; Williams, C. T.; Monnier, J. R. *Appl. Catal. A Gen.* **2014**, *475*, 161–168.

(55) Dimitratos, N.; Villa, A.; Wang, D.; Porta, F.; Su, D.; Prati, L. *J. Catal.* **2006**, *244*, 113–121.

(56) Ketchie, W. C.; Murayama, M.; Davis, R. J. *J. Catal.* **2007**, *250*, 264–273.

(57) Thuening, T.; Tysoe, W. T. *Catal. Letters* **2018**, *148*, 79–89.

(58) Han, Y. F.; Wang, J. H.; Kumar, D.; Yan, Z.; Goodman, D. W. *J. Catal.* **2005**, *232*, 467–475.

(59) Hanrieder, E. K.; Jentys, A.; Lercher, J. A. *ACS Catal.* **2015**, *5*, 5776–5786.

(60) Ward, T.; Delannoy, L.; Hahn, R.; Kendell, S.; Pursell, C. J.; Louis, C.; Chandler, B. D. *ACS Catal.* **2013**, *3*, 2644–2653.

(61) Bukhtiyarov, A. V.; Prosvirin, I. P.; Saraev, A. A.; Klyushin, A. Y.; Knop-Gericke, A.; Bukhtiyarov, V. I. *Faraday Discuss.* **2018**, *208*, 255–268.

(62) Aich, P.; Wei, H.; Basan, B.; Kropf, A. J.; Schweitzer, N. M.; Marshall, C. L.; Miller, J. T.; Meyer, R. *J. Phys. Chem. C* **2015**, *119*, 18140–18148.

(63) Edwards, J. K.; Freakley, S. J.; Carley, A. F.; Kiely, C. J.; Hutchings, G. J. *Acc. Chem. Res.* **2014**, *47*, 845–854.

(64) Edwards, J. K.; Solsona, B.; Ntainjua N, E.; Carley, A. F.; Herzing, A. A.; Kiely, C. J.; Hutchings, G. J. *Science (80-.).* **2009**, *323*, 1037–1041.

Chapter 2. Experimental Methods

2.1 Catalyst preparation and synthesis methods

2.1.1 Support pretreatment

Fumed silica (Cabosil EH5) was acid washed prior to use. Approximately 15 g were added to ~1L 0.1 M HNO_3 and the slurry was mixed for 2 hours. The silica was then filtered and washed with 18 MΩ MilliQ water, then dried in air at 383 K overnight. Once dry, the silica was crushed and sieved to between 60 and 100 mesh.

Activated carbon (Darco MRX) was pretreated at high temperatures prior to use. The carbon was treated under H_2 (Industrial Grade, Airgas) flow at 1173 K for 6 h (heating rate 20 K/min) and then cooled to room temperature and purged with inert gas prior to storage in air.

Titania (Degussa P25) was used as received.

2.1.2 Impregnation

Monometallic Pd catalysts were synthesized using incipient wetness impregnation. An aqueous solution of palladium nitrate hydrate ($Pd(NO_3)_2$, 40% Pd basis, Sigma Aldrich) was added dropwise to the support (TiO_2, C, or SiO_2) and continuously mixed until the incipient wetness point was reached. The catalyst was then dried in air overnight at 383 K, reduced under flowing hydrogen at 533 K for 6 hours (with heating rate of 1 K min^{-1}), and finally passivated with flowing 1% O_2 in He (Airgas).

The parent Ag/C catalyst was synthesized by wet impregnation. The desired amount of $AgNO_3$ was dissolved in excess ethanol (Fisher Chemical), added to the carbon, and stirred overnight at room temperature. The catalyst was then dried in air at 383 K. The Ag catalyst was reduced at 623 K in H_2 for 6 h (heating rate 1.5 K/min). After cooling to room temperature, the catalysts were passivated in 1% O_2 in He.

2.1.3 Ion exchange and deposition precipitation

A monometallic, Au/TiO_2 parent catalyst was synthesized using a deposition precipitation method, as described by Li, et al. to achieve small Au particles.[1] Briefly, TiO_2 was added to deionized (to a resistivity of 18.2 MΩ cm) water and stirred for 30 minutes. The pH of this slurry was adjusted to pH 10 using 0.1 M sodium hydroxide (NaOH, 97%, Sigma Aldrich) and then stirred for 90 minutes. A 0.2 M solution of gold chloride hydrate ($HAuCl_4$, 99.995%, Sigma Aldrich) containing the desired quantity of gold was added to 15 mL of 0.01 M NaOH solution and let sit for 30 minutes. The Au solution and 0.1 M NaOH were then added to the TiO_2 slurry simultaneously such that the pH remained constant at 10. The slurry was stirred for 2 hours, then centrifuged and washed with water. The Au/TiO_2 catalyst was dried in a vacuum desiccator overnight, and then reduced under flowing hydrogen at 623 K for 6 hours (with a heating rate of 1.5 K min) and finally passivated with flowing 1 mol% O_2 in He.

Ag/SiO_2 and Ag/TiO_2 catalysts were synthesized by deposition precipitation. The desired amount of silver nitrate ($AgNO_3$) (99+%, Sigma-Aldrich) in DI water was added to a slurry of SiO_2 or TiO_2 and was heated to 353 K. 0.1 M NaOH was added to adjust the pH of the slurry to 9 then stirred for 2 h. The catalyst was filtered and washed with excess water then dried at 383 K for 12 h. The Ag catalyst was then reduced at 623 K in H_2 for 6 h (heating rate 1.5 K/min). After cooling to room temperature, the catalysts were passivated in 1% O_2 in He.

The parent Cu/TiO_2 and Cu/SiO_2 catalysts were synthesized using ion exchange. The desired amount of tetraammine copper sulfate ($[Cu(NH_3)_4]SO_4 \cdot xH_2O$, Strem) was added to 18 MΩ water. A 5% ammonium hydroxide (NH_3OH, Sigma-Aldrich) solution was added to the copper solution to dissolve. Separately, either the TiO_2 or the SiO_2 was added to 18 MΩ water and then the copper solution was added to the slurry. 2 M sulfuric acid (H_2SO_4, Sigma-Aldrich) was added to adjust the pH to 9. The slurry was stirred overnight then filtered and washed with excess water. The final catalyst was dried in a 333 K vacuum oven overnight. The dried Cu catalyst was treated first for 30 min at 573 K under Ar (Industrial Grade, Airgas) flow (heating rate 5 K/min) then at 673 K for 3 h under H_2 flow (heating rate 5 K/min). The catalyst was held at 673 K for an additional hour under Ar flow before cooling to room temperature and passivating in 1% O_2 in He.

2.1.4 Controlled surface reactions

Bimetallic AuPd/TiO_2 catalysts were synthesized using controlled surface reactions, a method developed in previous work for other multimetallic systems.[2–6] The general procedure is shown in Figure 2.1 below.

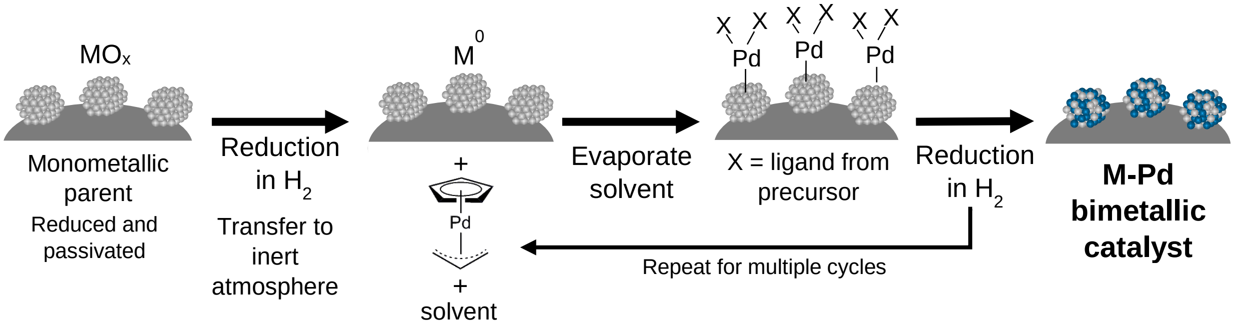

Figure 2.1. Schematic of controlled surface reaction approach to synthesizing supported bimetallic catalysts. The parent metal is denoted as M. Pd is deposited using a cyclopentadienyl Pd allyl organometallic precursor.

A portion of the parent catalyst, synthesized as described above, was reduced in H_2 then cooled to room temperature and purged with inert gas. The catalyst was then sealed and transferred to an inert atmosphere glove box (Vacuum Atmospheres) using Schlenk techniques. The desired amount of cyclopentadienyl palladium allyl (Cp(Pd)allyl, 98%, Strem Chemicals) was dissolved in anhydrous *n*-pentane (≥99%, Sigma Aldrich) and then added to the Schlenk tube containing the parent catalyst. The slurry was stirred for 1 hour, then the catalyst was allowed to settle and a small portion of the solution was removed for UV vis analysis. The remaining pentane was evaporated using Schlenk techniques and then the catalyst was reduced in flowing hydrogen without exposure to air. When multiple cycles were used, catalysts were returned to the glove box after reduction and the synthesis repeated. Equal amounts of Cp(Pd)allyl were used in each cycle to maintain a low concentration of precursor during synthesis, which, as discussed below in more detail, promotes selective bimetallic formation (as opposed to Pd deposition on the support). After reduction, the final catalysts were passivated in 1% O_2 in He. The bimetallic catalysts are designated MPd_x/support where M is the parent metal and x is the atomic Pd/M ratio as measured by inductively coupled plasma-optical emission spectroscopy.

For the AuPd system, the Au/TiO_2 catalyst was reduced prior to synthesis at 623 K under hydrogen flow for 6 hours (heating at 1.5 K min^{-1}). After Pd deposition and solvent removal, the catalyst was reduced under flowing hydrogen at 673 K for 6 hours (with a heating rate of 1.5 K min^{-1}) and passivated with flowing 1% O_2 in He.

For the AgPd system in the hydrodechlorination study, the selected Ag parent catalyst was re-reduced in H_2 at 623 K for 6 h (heating rate 1.5 K/min) prior to synthesis. The final catalyst after addition of Pd was reduced in flowing H_2 at 673 K for 6 h (heating rate 1.5 K/min) and then passivated in 1% O_2 in He.

For the AgPd and CuPd catalysts used in the acetylene hydrogenation study, a portion of the selected Ag or Cu parent catalyst was re-reduced in H_2 for 4 h (heating rate 5 K/min) at 673 K for Ag and 573 K for Cu. The final catalyst after Pd addition was reduced in H_2 at 673 K for 4 h (heating rate 5 K/min) and then passivated in 1% O_2 in He.

Control experiments were carried out where palladium was introduced to the support alone. The TiO_2, SiO_2, or C support was treated hydrogen flow using the same conditions as the relevant bimetallic synthesis then transferred to an inert atmosphere glovebox. Following the same procedure as described above, Cp(Pd)allyl was introduced in a *n*-pentane solution and mixed with the support, then the remaining pentane was evaporated, and the final material was treated in hydrogen at 673 K.

2.2 Catalyst Characterization

2.2.1 CO chemisorption

The Pd dispersion was measured by CO (CP Grade, Airgas) chemisorption using a custom volumetric and gas-handling apparatus. CO was purified by passing over copper turnings at 503 K to remove metal carbonyls and 4 Å molecular sieves to remove water prior to use. Catalyst samples were reduced in flowing hydrogen (Industrial Grade, Airgas), typically between 473 and 533 K, prior to analysis. After reduction, the samples were evacuated to 10^{-5} Torr and cooled to room temperature to collect the isotherms. CO adsorption was carried out at 293 K and the catalyst sample was evacuated for 30 minutes between collection of the first and second isotherms. The Pd site density is reported as the irreversible CO uptake using a stoichiometry of 1 Pd:1 CO and is discussed further below.

2.2.2 N_2O titration

Surface Ag sites were measured using N_2O titration, following the methods of Seyedmonir et al.[7] Catalysts were reduced at 473 K in H_2 for 6 h (heading rate 0.75 K/min) and then evacuated to 10^{-5} Torr. N_2O was introduced to the catalyst samples at 443 K and oxidized the Ag surface by the following stoichiometry $N_2O + Ag_s \rightarrow Ag_sO + N_2$, where *s* represents a surface atom. Surface Cu sites were also measured using N_2O titration, following the methods of Evans et al.[8] Catalysts were reduced at 473 K in H_2 for 6 h (heating rate 0.75 K/min) and then N_2O was introduced to the sample at 363 K. The Cu surface was oxidized by the following stoichiometry $N_2O + 2Cu_s \rightarrow (Cu_s)_2O + N_2$. N_2O (CP Grade, Matheson) was purified by passing over Drierite prior to use. The pressure of N_2 was determined using a Baratron pressure gauge after condensing the remaining N_2O in a liquid nitrogen trap.

2.2.3 Fourier transform infrared spectroscopy

Infrared spectra of probe molecules adsorbed on catalyst samples were collected using a Nicolet 6700 spectrometer connected to a custom vacuum manifold. Catalyst samples were pressed into self-supporting pellets and loaded into a transmission cell described elsewhere.[9,10] Typically, samples were reduced in flowing hydrogen (Industrial Grade, Airgas) between 473-573 K then cooled to room temperature and evacuated to 10^{-5} Torr or purged with argon (UHP, Airgas). A background scan was collected with a resolution of 4 cm^{-1} and typically averaging 256 scans. Details on the experimental conditions used for each catalyst system are described in the following chapters.

2.2.4 Inductively coupled plasma-optical emission spectroscopy

The total metal content of catalysts was determined using a Varian Vista-MPX CCD Simultaneous inductively coupled plasma-optical emission spectrometer (ICP-OES). Calibrations for ICP analysis were obtained by analyzing dilutions of commercial ICP standards (Fluka, 1000 mg L^{-1}).

2.2.5 UV-visible absorption spectroscopy

UV-visible absorption spectra of cyclopentadienyl Pd allyl in *n*-pentane were collected using a Thermo Scientific Evolution 300 UV-visible spectrometer. Spectra were collected over wavelengths ranging from 190 to 600 nm using a 1 cm path-length quartz cuvette to contain the samples. Solutions were prepared inside an inert glove box and then transferred to the cuvette in air for analysis. A control experiment using a sealed cuvette which was loaded in the glove box and then analyzed without exposing the solution to air showed the same spectra as the same solution exposed to air to transfer to a cuvette (Appendix Figure B.1), indicating negligible decomposition of the Cp(Pd)allyl precursor.

2.2.6 Scanning transmission electron microscopy – energy dispersive X-ray spectroscopy

Scanning transmission electron microscopy (STEM) imaging was performed using a FEI Titan STEM with Cs aberration correction operated at 200 kV in high-angle annular dark field (HAADF) mode. Energy dispersive X-ray spectroscopy (EDS) data was collected using the same microscope with an EDAX SiLi detector. Particle composition distributions of each sample were determined by EDS analysis of at least 30 particles. Samples were prepared by dropping the passivated catalyst, suspended in ethanol, on a holey carbon coated Cu grid. For EDS analysis of Cu-containing samples, holey carbon coated Au grids were used. The samples were plasma cleaned before loading in the microscope.

2.2.7 X-ray absorption spectroscopy

X-ray absorption spectroscopy (XAS) measurements were taken at MRCAT facilities (beamlines 10-BM and 10-ID) at the Advanced Photon Source at Argonne National Laboratory. Measurements were taken at the Pd-K edge (24350 eV), Ag-K edge (25514 eV), and Au-L_3 edge (11919 eV). Samples were pressed into wafers inside a stainless-steel sample holder, which was placed inside a quartz tube with Kapton windows on each end and fittings to allow for gas flow through the cell. The pretreatment and analysis conditions as well as fitting parameters for each system are described in the following chapters. Spectra of Au, Ag, or Pd foils were collected with each sample to calibrate the energy.

2.3 Reactivity Studies

2.3.1 Gas phase amination of 1-hexanol using ammonia

Reactivity studies for the gas-phase amination of 1-hexanol using ammonia were conducted in a 0.7-inch OD fixed bed, borosilicate glass flow reactor operated in a down-flow configuration. Prior to each reaction, catalysts were reduced under flowing H_2 (Industrial Grade, Airgas) at 533 K for 1 h with a heating rate of 2 K min^{-1}. All reactions were conducted at 503 K and 1 atmosphere total pressure with a gas composition of 0.07 kPa hexanol, 2.5 kPa NH_3, 51 kPa H_2, and balance He. To trap all products, the reactor effluent was fed to a borosilicate glass trap filled with 1-butanol (99.9% HPLC Grade, Sigma-Aldrich) and immersed in an ice-water bath. To quantify product formation, the reactor was periodically (approximately every 2 h) isolated, during which time the butanol-containing product trap was replaced with another equivalent one. The butanol solution from the just-removed trap was then injected on a gas chromatograph (Shimadzu GC-2010) equipped with a flame-ionization detector (GC-FID) and a Zebron ZB-s50 column (30 m x 0.25 mm OD, Phenomenex). After each reaction, the reactor was cleaned by soaking in nitric acid to be used again. Additional details are provided in Section 3.4.3.

2.3.2 Hydrodechlorination of 1,2-dichloroethane

Reactivity studies for the hydrodechlorination of 1,2-dichloroethane over AgPd catalysts were conducted in a fixed bed stainless steel reactor. Catalysts were pressed and sieved to 20/40 mesh and diluted twice by weight with similarly sized alpha alumina. A cylindrical aluminum block, with imbedded cartridge heaters, was clamped around the middle of the reactor and served as the heating source for the reactor. He, N_2, and H_2 (Research Grade, Airgas), delivered by mass flow controller (Brooks 5890E), and liquid dichloroethane (99%, Aldrich), delivered via syringe pump (ISCO), were used without further purification. Reactant and product analysis was performed by Siemens Maxum GC with argon carrier gas using a TCD detector for analysis of N_2, H_2, ethane, ethylene, and methane and an FID detector for analysis of dichloroethane and ethyl chloride. All measurements were carried out at a 1,2-DCA conversion of less than 2% and rate and selectivity values represent averages over 4 hours time on stream, during which time the rate remained constant within 10%. Additional details are provided in Section 4.4.3.

2.3.3 Acetylene hydrogenation

For reactivity studies of acetylene hydrogenation, catalysts were diluted in silica gel then loaded into a 1/2-inch outer diameter, stainless steel reactor between quartz wool (Ohio Valley Specialty) and silica chips (Sigma-Aldrich). He (Industrial Grade, Airgas), H_2 (Industrial Grade, Airgas), C_2H_4 (CP Grade, Airgas), and C_2H_2 (Industrial Grade, Airgas) were delivered by mass flow controller (Brooks SLA5800) and used without further purification. Prior to reaction, the catalyst bed was calcined in air (Breathing Air, Airgas) at 723 K for 90 minutes (heating rate 10 K/min) and then reduced in H_2 (Industrial Grade, Airgas) at 473 K for 3 hours. The reactor was purged with inert gas at 473 K for 30 minutes then cooled to reaction temperature (typically 313 K). Reactant and product analysis was performed by Shimadzu GC-2014 with He carrier gas using an FID detector and an RT Alumina Bond column for analysis of ethane, ethylene, and acetylene. Additional details are provided in Section 5.4.3.

2.4 References

(1) Li, W.; Comotti, M.; Schuth, F. *J. Catal.* **2006**, *237*, 190–196.

(2) Aragão, I. B.; Ro, I.; Liu, Y.; Ball, M.; Huber, G. W.; Zanchet, D. *Appl. Catal. B Environ.* **2018**, *222*, 1–2.

(3) Liu, Y.; Göeltl, F.; Ro, I.; Ball, M. R.; Sener, C.; Aragão, I. B.; Zanchet, D.; Huber, G. W.; Mavrikakis, M.; Dumesic, J. A. *ACS Catal.* **2017**, *7*, 4550–4563.

(4) Ro, I.; Liu, Y.; Ball, M. R.; Jackson, D. H. K.; Chada, J. P.; Sener, C.; Kuech, T. F.; Madon, R. J.; Huber, G. W.; Dumesic, J. A. *ACS Catal.* **2016**, *6*, 7040–7050.

(5) Sener, C.; Wesley, T. S.; Alba-Rubio, A. C.; Kumbhalkar, M. D.; Hakim, S. H.; Ribeiro, F. H.; Miller, J. T.; Dumesic, J. A. *ACS Catal.* **2016**, *6*, 1334–1344.

(6) Hakim, S. H.; Sener, C.; Alba-Rubio, A. C.; Gostanian, T. M.; O'Neill, B. J.; Ribeiro, F. H.; Miller, J. T.; Dumesic, J. A. *J. Catal.* **2015**, *328*, 75–90.

(7) Seyedmonir, S. R.; Strohmayer, D. E.; Geoffroy, G. L.; Vannice, M. A.; Young, H. W.; Linowski, J. W. *J. Catal.* **1984**, *87*, 424–436.

(8) Evans, J. W.; Wainwright, M. S.; Bridgewater, A. J.; Young, D. J. *Appl. Catal.* **1983**, *7*, 75–83.

(9) Shen, J.; Hill, J. M.; Watwe, R. M.; Spiewak, B. E.; Dumesic, J. A. *J. Phys. Chem. B* **1999**, *103*, 3923–3934.

(10) Carrasquillo-Flores, R.; Ro, I.; Kumbhalkar, M. D.; Burt, S.; Carrero, C. A.; Alba-Rubio, A. C.; Miller, J. T.; Hermans, I.; Huber, G. W.; Dumesic, J. A. *J. Am. Chem. Soc.* **2015**, *137*, 10317–10325.

Chapter 3. Amination of 1-Hexanol on Bimetallic AuPd/TiO_2 Catalysts

This chapter is adapted from: Ball, M. R.; Wesley, T. S.; Rivera-Dones, K. R.; Huber, G. W.; Dumesic, J. A. *Green Chem.* **2018**, *20*, 4695–4709.

3.1 Introduction

Amines are widely used in the chemical industry in the production of a range of useful chemicals, including pharmaceuticals, solvents, polymers, and dyes.[1–3] Typical amine syntheses are carried out using nitrile, carboxylic acid, halide, or carbonyl compounds as feedstocks, and current processes typically involve toxic species and create salt residues as a byproduct.[3–5] Thus, there exists motivation for development of more environmentally friendly processes for amine synthesis. One potentially attractive process for amine synthesis is the direct amination of alcohols to amines using ammonia. Alcohols, which are widely produced in environmentally friendly biorefinery processes, can thus be converted to amines with water formed as the only byproduct.[3–5] Thus, direct amination of alcohols offers a less toxic and more sustainable route for production of amines. This work focuses on the gas-phase amination of an aliphatic alcohol *(i.e.*, 1-hexanol) with ammonia via “hydrogen borrowing” chemistry using AuPd/TiO_2 catalysts.

“Hydrogen borrowing” generally refers to atom-efficient reactions that navigate through dehydrogenated intermediates. These intermediates are subsequently reduced using hydrogen temporarily “borrowed” by the catalyst from the reactants, such that no net hydrogen is consumed.[6,7] In the case of alcohol amination, it is generally viewed that the alcohol is oxidized to its corresponding ketone or aldehyde, which undergoes nucleophilic attack by the reactant amine to form water (the only byproduct) and an imine. The imine, in turn, is hydrogenated to the product amine. This chemistry has been widely implemented in industry, with most commercial aliphatic amine syntheses relying on Co-, Ni-, Cu-, and Zrbased catalysts and ammonia as the aminating agent.[8–10]

Several studies have investigated heterogeneously-catalyzed amination of aliphatic alcohols using ammonia.[7] Shimizu et al. demonstrated the use of Ni/Al_2O_3 for the amination of various alcohols with NH_3, achieving more than 68% selectivity to the corresponding primary amine.[3] Recently, Dumon et al. studied *n*-octanol amination using ammonia over Ni and Pd catalysts.[4] Density functional theory (DFT) calculations for the amination of methanol were carried out on Ni and Pd surfaces, and they found adsorbed ammonia to be key in predicting reactivity. The use of Ni catalysts for alcohol amination was further investigated by Tomer et al., employing a mixed metal oxide support or cyclodextrin complexes to increase conversion and selectivity to the primary amine by improving the reducibility and dispersion of nickel oxide species.[2,11] The role of Pd in amination reactivity is less well understood, and thus we have studied the impact of Pd structure on catalytic activity. Bimetallic catalysts offer an important approach to tuning the reactivity of metal catalysts, having exhibited improved or tunable reactivity, selectivity, or stability for a wide variety of reactions ranging from chemistries such as hydrogenation,[12–15] hydrogenolysis,[16–19] and hydrogen production,[20–25] to more recent efforts targeting the production of renewable chemicals and fuels via biomass upgrading[26–29] and electrochemical processes.[30–33]

The effects of bimetallic formation on amination reactions have been investigated in the literature for selected cases. Recently, Takanashi et al. demonstrated synergy between rhodium and indium for the amination of 1,2-propanediol.[34,35] The rate promotion was attributed to an electronic perturbation of rhodium sites by indium that weakens the binding of ammonia. However, they also observed reduced activity at high indium loadings, and they attributed this behavior to an ensemble effect impeding the adsorption of propanediol. $Pt\text{-}Sn/\gamma\text{-}Al_2O_3$ has also been shown to be effective for the conversion of alcohols to secondary and tertiary amines, with Sn promoting both overall reactivity as well as selectivity to amines over imines.[36,37]

Here, we use AuPd catalysts to modify the Pd structure with the goal of understanding bimetallic effects for amination chemistry. To develop robust design principles for optimizing multimetallic catalysts, it is necessary to understand the implications of intermetallic bonding on the properties of catalytic surfaces and, in turn, how these features dictate surface chemistry.[38,39] Although supported Au-Pd catalysts have not yet to our knowledge been applied to the direct amination of aliphatic alcohols using ammonia, they have been applied to similar reactions. Ono and Ishida investigated the amination of phenols with ammonia using Pd/Al_2O_3-based catalysts, and they observed that the addition of Au to Pd improved catalyst stability, with a negligible effect on initial mass-specific rates.[40] More recently, Sankar, et al. employed titania-supported Au-Pd and Ru-Pd alloy catalysts for the one-pot synthesis of *N*-benzylideneaniline and *N*-benzylaniline from nitrobenzene and benzyl alcohol via initial transfer hydrogenation to form aniline and benzaldehyde intermediates.[41] Both alloys were shown to be more active than monometallic Pd for the conversion of the limiting reagent, nitrobenzene. The increased activity of Au-Pd bimetallics was attributed to an electronic effect whereby the rate of benzyl alcohol dehydrogenation, the suggested rate-limiting step, was increased. The high activity of Ru-Pd catalysts was hypothesized to arise from a stabilization of Pd by the Ru in small nanoparticles.

Here, we report reactivity and selectivity trends for a series of $AuPd/TiO_2$ catalysts for the gas-phase amination of 1-hexanol using ammonia. The catalysts were synthesized using controlled surface reactions to achieve bimetallic formation, and catalysts were characterized using CO chemisorption, Fourier transform infrared (FTIR) spectroscopy of adsorbed CO, scanning transmission electron microscopy (STEM), energy-dispersive X-ray spectroscopy (EDS), and X-ray absorption spectroscopy (XAS) techniques. We show that the addition of Pd to Au catalysts initially promotes the formation of primary products, followed by a promotion of secondary amine formation. Based on reaction kinetics studies and spectroscopic evidence, we suggest that ensemble effects likely predominate over electronic effects.

3.2 Results and Discussion

3.2.1 Selective Deposition of Pd

The loadings of the Au, Pd, and AuPd catalysts are shown in Table 3.1. Up to a Pd/Au ratio of about 0.5, the Pd/Au molar ratio as determined by ICP agrees with the ratio targeted during synthesis, indicating that most of the Pd introduced during the synthesis procedure was taken up by the Au/TiO_2 parent catalyst.

Table 3.1. Compositions of Au/TiO_2, Pd/TiO_2, and AuPd/TiO_2 catalysts.

Catalyst	Targeted Atomic Ratio Pd/Au	ICP Atomic Ratio Pd/Au	ICP Au (wt%)	ICP Pd (wt%)
Au/TiO_2	-	-	1.09%	-
$AuPd_{0.06}/TiO_2$	0.05	0.06	1.06%	0.03%
$AuPd_{0.23}/TiO_2$	0.2	0.23	1.25%	0.16%
$AuPd_{0.55}/TiO_2$[a]	0.5	0.55	1.09%	0.31%
$AuPd_{0.67}/TiO_2$[a]	1	0.67	1.03%	0.37%
Pd/TiO_2	-	-	-	0.47%

[a] Synthesized in two cycles with equal amounts of Pd deposited during each cycle

This conclusion is corroborated by UV-vis spectra of the synthesis solutions, shown in Figure 3.1 and in the Appendix Figure A.2. The large decrease in peaks at 260 and 320 nm after mixing the Cp(Pd)allyl solution with the reduced Au/TiO_2 parent catalyst indicates that essentially all of the Cp(Pd)allyl has been taken up by the Au/TiO_2 (Figure 3.1a). During a control experiment, 81% of the Cp(Pd)allyl was taken up by the TiO_2 support, shown by the spectra in Figure 3.1b. This result indicates that although some Cp(Pd)allyl may be deposited on the support during AuPd catalyst synthesis, the increased Pd uptake in the presence of Au suggests that Pd may preferentially go to the Au rather than the support. Additionally, the Cp(Pd)allyl uptake onto the support increases with increasing concentration.[42] Because the control experiment was performed with 1.5 mg Cp(Pd)allyl/g pentane, whereas all catalyst syntheses were carried out with precursor concentrations of at most 1.0 mg Cp(Pd)allyl/g pentane, we conclude that the uptake of Cp(Pd)allyl onto Au during synthesis is increased compared to uptake onto TiO_2. Maintaining low concentrations during synthesis is necessary to achieve selective deposition of Pd onto Au and additional characterization is needed to confirm formation of AuPd species.

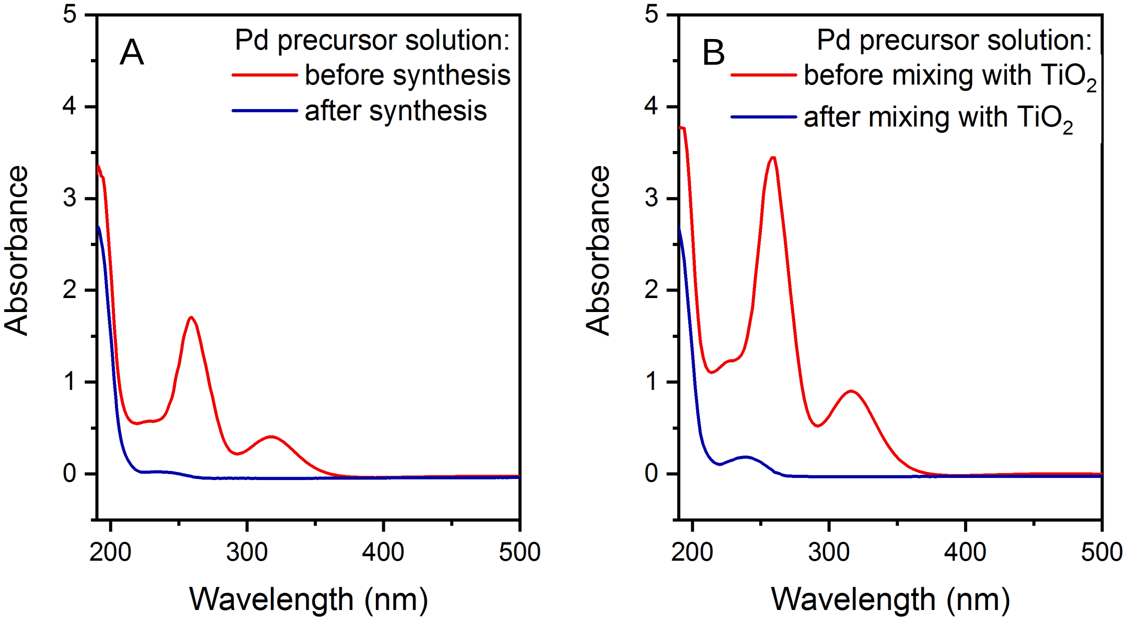

Figure 3.1. UV-vis spectra of Cp(Pd)allyl in pentane before (—) and after (—) contact with (a) reduced Au/TiO_2 catalyst during the synthesis of $AuPd_{0.23}/TiO_2$ and (b) TiO_2 as a control. Precursor concentrations were 1.0 and 1.5 mg Cp(Pd)allyl/g pentane for the synthesis (a) and control (b), respectively.

The catalysts were also analyzed by STEM-EDS to determine particle-size distributions and qualitative compositional distributions of the individual AuPd nanoparticles. The composition distributions are shown in Figure 3.2. The average composition calculated from this EDS analysis indicates a lower Pd content than that determined by ICP. This discrepancy can be attributed either to damage to the small nanoparticles by the electron beam during analysis or to large Pd particles not present in the areas observed by STEM. The likelihood of large monometallic Pd particles will be discussed further below with respect to the chemisorption and FTIR results. It is important to note, however, that on the sample areas analyzed by STEM-EDS, monometallic Pd particles were not observed and few monometallic Au particles were observed, indicating formation of AuPd bimetallic nanoparticles.

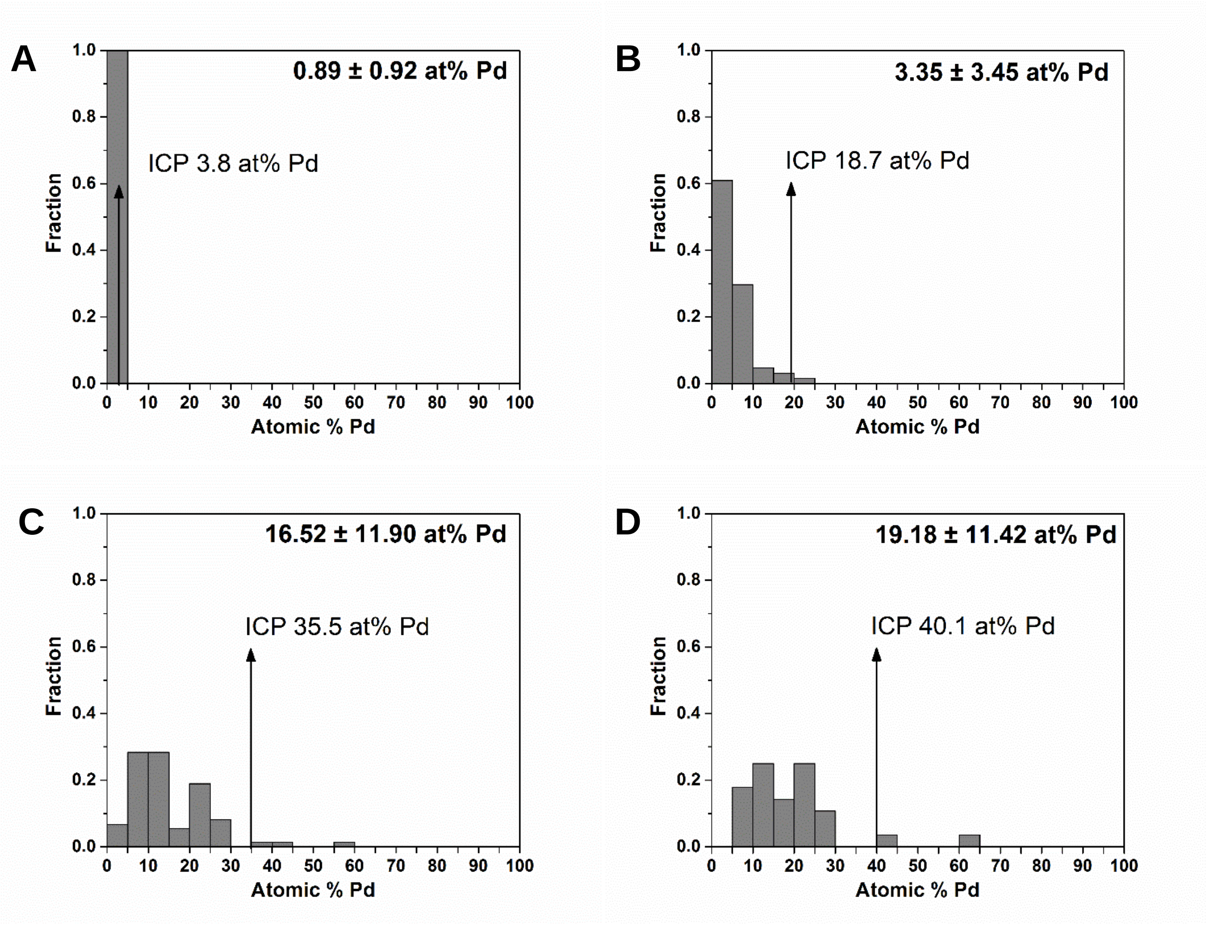

Figure 3.2. Composition distribution for (a) $AuPd_{0.06}/TiO_2$, (b) $AuPd_{0.23}/TiO_2$, (c) $AuPd_{0.55}/TiO_2$, and (d) $AuPd_{0.67}/TiO_2$ as measured by EDS analysis of individual nanoparticles. The average composition and standard deviation is shown and the composition as determined by ICP is shown by the arrow.

3.2.2 Bimetallic Catalyst Structure

Surface site densities, dispersions, and STEM-based particle sizes of the Au/TiO_2, Pd/TiO_2, and AuPd/TiO_2 catalysts are shown in Table 3.2. The Au fractional dispersion, *D*, was estimated from the Au nanoparticle sample-average diameter in nm, *d*, assuming hemispherical particles using *D = 1.16/d* as described by Bergeret and Gallezot.[43] Surface Pd was quantified using CO chemisorption assuming that the number of exposed Pd atoms was equal to the irreversible CO uptake. This stoichiometry was chosen because it has been previously reported that Pd:CO chemisorption stoichiometries are approximately 1:1 for gold-rich supported AuPd catalysts.[44] Furthermore, this stoichiometry reflects predominantly linear CO adsorption atop surface Pd atoms, which is supported by our FTIR results (see below). On monometallic Pd catalysts, however, Pd:CO stoichiometries are known to be higher (up to Pd:CO = 2 or higher)[44] due to the presence of bridge-bonded CO.[45,46] For consistency with the bimetallic AuPd catalysts here however, we have also elected to use Pd:CO = 1:1 for Pd/TiO_2 because this assumption provides a lower bound on the monometallic Pd site density, and thus an upper bound on the monometallic Pd site-time yields and a conservative estimate for the promotional effect of bimetallic formation.

Table 3.2. Catalyst site densities, dispersions, and particle sizes.

Catalyst	Site Density (μmol g^{-1})	Dispersion (%)	Average Particle Size[c] (nm)
Au/TiO_2	34[a]	64[a]	1.8 ± 1.4
$AuPd_{0.06}$/TiO_2	0.14[b]	4.9[b]	3.4 ± 1.7
$AuPd_{0.23}$/TiO_2	1.0[b]	6.6[b]	2.9 ± 1.5
$AuPd_{0.55}$/TiO_2	2.0[b]	7.0[b]	4.2 ± 5.1
$AuPd_{0.67}$/TiO_2	2.5[b]	7.3[b]	3.6 ± 2.4
Pd/TiO_2	7.3[b]	15[b]	1.1 ± 0.4

[a] Au surface site density and dispersion, estimated from the average particle size using *D = 1.16/d* (Ref 43) as determined by STEM.

[b] Pd surface site density and dispersion, measured by CO chemisorption, using a Pd:CO stoichiometry of 1:1.

[c] Measured by STEM.

Under the definition of a surface site as determined by CO uptake, it is clear from Table 3.2 that the Pd in the bimetallic catalysts has a lower dispersion than the Pd in the monometallic Pd catalyst, and that the Pd dispersion in the bimetallic catalysts modestly decreases as Pd is increasingly diluted in Au. Because the bimetallic catalysts were reduced at a higher temperature (673 K) during synthesis than the monometallic Pd catalyst (533 K) to ensure complete decomposition of the cyclopentadienyl ligands, it was necessary to determine whether the reduction in Pd dispersion upon bimetallic formation was caused by strong metal-support interactions (SMSI) between the Au or Pd and titania.

Strong metal-support interactions are reported to cause the migration of metal oxide species onto metal particles, potentially blocking metal sites.[47] Indeed, the chemisorptive capacity of titania-supported catalysts decreases upon reduction at temperatures as low as 573 K;[48] however, these effects may be reversed by calcining the catalyst at 673 K.[47] To determine the impact of SMSI on the AuPd/TiO_2 catalysts, we first calcined a portion of the $AuPd_{0.55}/TiO_2$ catalyst at 673 K to remove any TiO_x species from the surface of the metal nanoparticles, and we subsequently reduced the sample at 533 K, the reduction temperature of the monometallic Pd/TiO_2. If SMSI were responsible for the lower Pd dispersion in the bimetallic catalysts, then we would expect the irreversible CO uptake on this new sample to exceed the value reported in Table 3.2; however, calcination had the opposite effect: CO uptake decreased to 1.1 μmol g^{-1}, likely due to sintering (Appendix Table A.1). To circumvent possible effects of sintering, in a second experiment the monometallic Pd/TiO_2 catalyst was reduced at 673 K—the reduction temperature used during bimetallic synthesis—prior to CO chemisorption, to determine if the higher-temperature reduction would induce SMSI effects and thus decrease CO uptake on the monometallic catalyst. The CO uptake on Pd/TiO_2 after reduction at 673 K was 5.7 μmol g^{-1}, 22% lower than the value reported in Table 3.2, which could be due to mild SMSI and/or particle sintering. This reduced CO uptake is consistent with the uptake reduction reported by Bracey and Burch in a similar comparison.[48] However, this effect is not sufficient to explain the factor-of-two discrepancy in dispersion between the monometallic Pd and bimetallic AuPd catalysts. We also note that work by Gubó et al. determined that a Au rich shell formed in AuPd particles with a high Au concentration which was less susceptible to SMSI than Pd rich particles.[49] Therefore, while modest SMSI effects may occur in our bimetallic catalysts, they are not the primary cause of the low Pd dispersion in the bimetallics. The low dispersion of the bimetallic catalysts could be attributed to the presence of some large monometallic Pd particles, which may partially explain the difference between the EDS and ICP compositions, as discussed above. We note, however, that the dispersion of the monometallic Pd/TiO_2 catalyst (which has particles less than 2 nm in diameter) is higher than that of the bimetallic catalysts. Thus, while some large Pd particles may be present on the bimetallic catalysts, we do not expect this behavior to be the main explanation for the apparent low dispersion. We instead hypothesize that the unaccounted-for Pd is subsurface within the AuPd nanoparticles.

The preferential segregation of Au to the surface of AuPd nanoparticles is well-established in the literature, and can be the result of Au having a lower partial molar surface free energy than Pd.[46,50,51] In general, however, the surface concentration of bimetallic Au-Pd nanoparticles is dependent on the synthesis method and reaction conditions (e.g., temperature, gas composition) used.[45,51] For example, there are conditions under which Pd-rich particles have been observed to be surface-enriched in Pd.[52,53] Most notably, the segregation of Pd to the surface of bimetallic nanoparticles in the presence of CO has been well studied.[54–56] However, because of the low Pd content in the catalysts studied here, we expect that most Pd is sufficiently subsurface as to encounter prohibitively high barriers for diffusion to the nanoparticle surface, even in the presence of CO. Furthermore, work by Seemala, et al. found that the metal structure of bimetallic catalysts was influenced by the TiO_2 support.[57] In CuNi bimetallic particles, the TiO_2 support was found to induce segregation such that Cu was preferentially found on the particle surface while Ni was found at the interface with the support. This type of bimetallic segregation, induced by the differential interactions of reducible TiO_2 with the two metals, could explain the low amount of surface Pd (which is more oxophilic than Au) in the AuPd particles. Other modeling work by Xu, et al. showed that the structure of AuPd particles was dependent on the redox properties of the support.[58] They determined that for particles on a TiO_2 support under reducing conditions, Pd preferred to be at the interface of the metal particle and oxide support or in the core of the particle. Thus, the subsurface Pd observed in the AuPd/TiO_2 catalysts used in this study can be explained based on the relative stabilities of Au and Pd in various particle configurations. Because of the Pd being primarily sub-surface or at the support interface in the bimetallic catalysts, the Pd which remains on the particle surface has a different structure than the structure found in monometallic Pd catalysts, as indicated by the FTIR results discussed below.

Results from CO FTIR spectroscopy provide insight into the structure of the surface Pd species on the bimetallic catalysts. Figure 3.3 shows spectra taken at (a) 283 K and (b) 153 K after exposing the reduced catalysts to 300 Torr of 1 mol% CO in He. At low temperature, peaks corresponding to CO on Pd are not visible in the bimetallic catalysts because the Pd loadings are low and because the extinction coefficient of CO bound to Pd is much lower than that of CO bound to Au.[59,60] The peak observed at 2103 cm^{-1} for all catalysts at 153 K can be assigned to the stretching of CO bound linearly to the top of a Au atom (Figure 3.3b).[56] When the temperature is increased to 283 K, this peak shifts to 2112 cm^{-1} and decreases in intensity as CO desorbs from Au (Figure 3.3a). This blue-shift with decreasing CO coverage has been previously observed[56,61,62] and has been primarily attributed to the fact that CO chemisorption induces coverage dependent changes to the electronic band structure of Au.[62,63] This chemical effect of changing CO coverage was further shown to dominate over dipolar coupling between co-adsorbed CO molecules,[63,64] the latter of which increases CO vibrational frequency with increasing coverage.[65]

The changes in this CO-Au peak are not likely attributable to interaction with Pd, however, because the Pd/Au ratio is low such that we do not expect Pd to greatly influence bulk Au electronically. Au atoms that are locally coordinated with Pd are likely to be influenced by Pd to some extent; however, this electronic interaction is expected to affect a low fraction of Au atoms and therefore not be represented in the bulk FTIR measurement for Au.

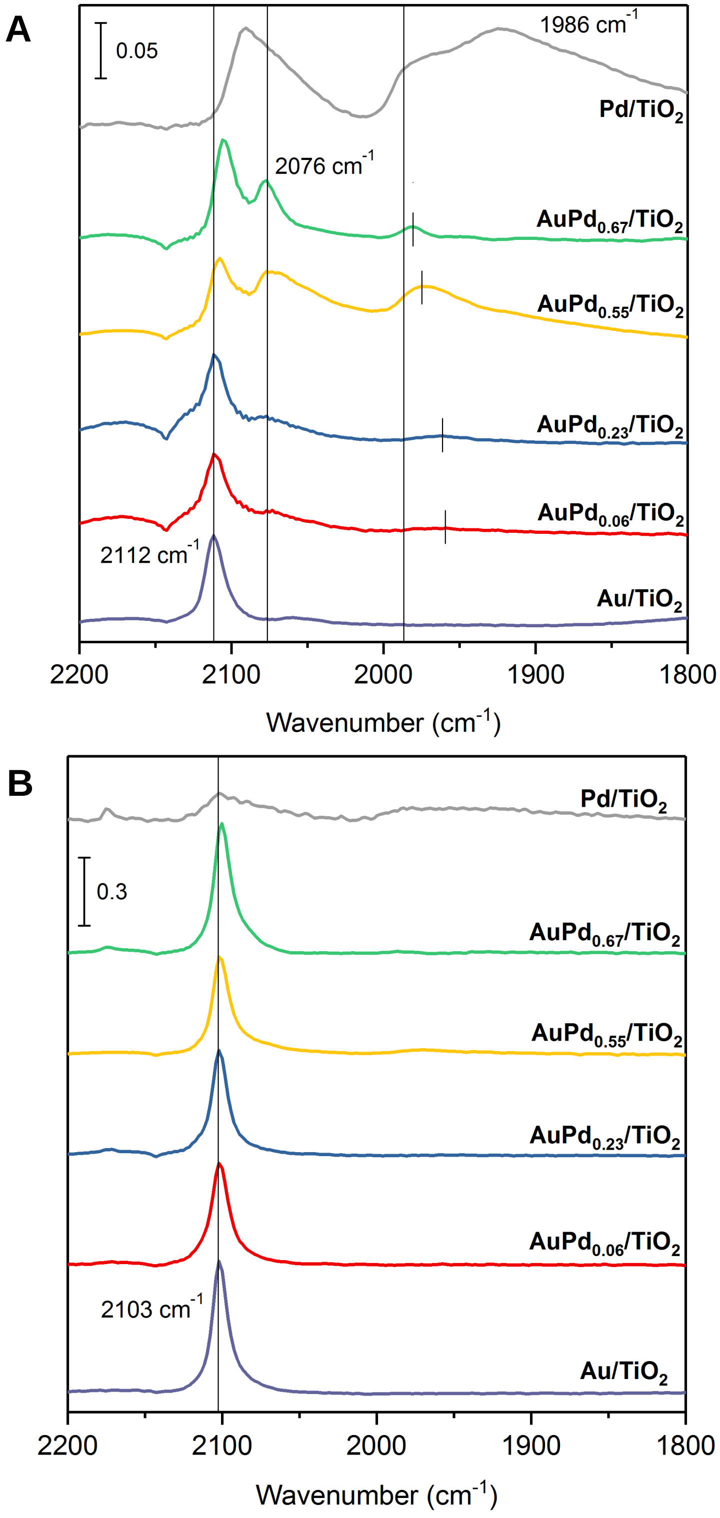

Figure 3.3. FTIR spectra of CO adsorbed on catalysts at (a) 283 K and (b) 153 K. The spectra were collected after introducing 300 Torr of 1 mol% CO in He.

For the monometallic Pd catalyst at room temperature (Figure 3.3a), we observe a peak at 2090 cm^{-1}, corresponding to linear CO on Pd.[52,56,66] A large, broad peak at 1924 cm^{-1} with a shoulder at 1986 cm^{-1} is also observed, corresponding to CO on three-fold Pd sites and bridge sites, respectively.[56,67–69] The linear CO peak at 2090 cm^{-1} for monometallic Pd/TiO_2 is red shifted to 2076 cm^{-1} for the AuPd bimetallic catalysts. Likewise, as Pd is increasingly diluted with Au, the bridging CO peak at 1986 cm^{-1} in the monometallic Pd also shifts to a lower wavenumber. This shift is consistent with the findings of Kugler and Boudart, who studied CO adsorption on AuPd/SiO_2 catalysts.[70] Using isotopically labelled CO to distinguish electronic alloying effects from co-adsorbate interactions, they concluded that the shift in linear-bound CO predominantly arises from electronic Au-Pd interactions, while the shift in bridge-bonded CO is primarily due to co-adsorbate interactions. Increasing Pd content is expected to lead to larger ensembles of contiguous Pd atoms and thus to more extensive CO interactions and dipolar coupling, which increases the frequency of observed vibrational modes.[45,65]

Electronic effects may be rationalized by a combined transfer of *s* and *p* electron density from Pd to Au and a concomitant, partially charge-compensating *d* electron transfer in the reverse direction.[38,46,51,71] Because metal-adsorbate interactions are mediated primarily by the metal *d*-states, as opposed to the *sp*-states,[72] the increased *d*-electron density in Pd atoms from Au coordination leads to increased occupancy of molecular orbitals exhibiting antibonding character with respect to carbon and oxygen.[73,74] The C-O bond is thus weakened, which we observe in the FTIR spectra as a red-shifted CO vibration. This observation is well-established in the literature.[46,69,70] Thus, the electronic effects induced by AuPd bimetallic formation lead to changes in the adsorption of species onto the catalyst surface.

The relative intensity of the peaks for each of the CO binding modes on Pd provides information about the surface structure of the AuPd catalysts. The monometallic Pd catalyst shows a large, broad peak between 1800-2000 cm^{-1} corresponding to the adsorption of CO on bridge and 3-fold Pd sites. For all the bimetallic catalysts, this peak corresponding to multifold CO adsorption has a much smaller area, and linear CO adsorption dominates. At low Pd loadings (Pd/Au = 0.06 and 0.23) multifold adsorption of CO is negligible, while at higher loadings (Pd/Au = 0.55 and 0.67) a multifold CO peak is observed. The binding energy of CO on bridge and 3-fold Pd sites is stronger than the binding energy of CO on top Pd sites and thus CO adsorption is preferred on the multifold sites when available.[75,76] The low area of the multifold adsorption peak then indicates that most of the surface Pd on the bimetallic catalysts is present in isolated species surrounded by Au. The high ratio of the isolated Pd peak area to multifold Pd peak area on the bimetallic catalysts indicates a different geometric surface structure than on the monometallic Pd catalyst.

It has been reported in the literature that the interaction between Pd surface atoms is low, and as a result, Pd atoms are not likely to form clusters when no surface adsorbates are present.[54,55] When CO is present, Pd clusters are likely to form as a result of the stronger binding energy of CO on bridge Pd sites rather than top Pd sites.[55] However, the catalysts with Pd/Au = 0.06 and 0.23 do not show a multifold CO adsorption peak, which indicates that if the Pd concentration is sufficiently low, nearly all of the Pd can be isolated from other Pd atoms. This isolation may be at least partially explained by the Coulombic Pd-Pd repulsion induced by net charge transfer from Pd to Au.[46]

X-ray absorption spectroscopy on the reduced-and-passivated catalysts also provides evidence for interactions between Pd and Au in the bimetallic catalysts. Au and Pd speciation in the reduced-and-passivated catalysts was analyzed by X-ray absorption near edge spectroscopy (XANES) using a linear combination analysis, and the results are shown in Table 3.3. We note that some of these composition values are smaller than the corresponding error; however, this uncertainty does not affect the key conclusions from these experiments. In all of the Au-containing catalysts, Au is present as primarily metallic Au. For the Pd containing catalysts, however, Pd speciation shifts in favor of metallic Pd as the Pd/Au ratio decreases, ranging from Pd^0:PdO ≅ 1:1 in the monometallic Pd/TiO_2 catalyst to Pd^0:PdO ≅ 9:1 for $AuPd_{0.23}/TiO_2$. (The low Pd loading in $AuPd_{0.06}/TiO_2$ precluded this analysis for that catalyst.) The PdO species is characteristic of surface Pd in the passivating layer, which suggests that Pd increasingly favors migrating subsurface as the Pd loading decreases. This behavior would corroborate the low dispersions measured by CO chemisorption.

Table 3.3. Fractional composition of Au and Pd oxidation states in Pd/TiO_2, AuPd/TiO_2, and Au/TiO_2 catalysts, as determined by XANES analysis.

	Au L_3-Edge		**Pd K-Edge**	
Catalyst	**Au_2O_3**	**Au**	**PdO**	**Pd**
Au/TiO_2	0.04	0.96	N/A	N/A
$AuPd_{0.06}/TiO_2$	0.00	1.00	[a]	[a]
$AuPd_{0.23}/TiO_2$	0.03	0.97	0.10	0.90
$AuPd_{0.55}/TiO_2$	0.03	0.97	0.27	0.73
$AuPd_{0.67}/TiO_2$	0.04	0.96	0.28	0.72
Pd/TiO_2	N/A	N/A	0.54	0.46

[a] The Pd loading in the $AuPd_{0.06}/TiO_2$ catalyst was too low for reliable Pd speciation.

[b] Errors for the linear combination fit are ± 2%

The EXAFS fits at both the Au and Pd edges are shown in Table 3.4. For all the bimetallic catalysts, the Pd-Au coordination number is above 8 and the Pd-Pd coordination number is less than 1.6. These values indicate that Pd is well diluted in Au, in agreement with the results from the CO FTIR spectra. This result also suggests that monometallic Pd particles make up a negligible portion of the bimetallic catalysts. From the Au L_3-edge EXAFS analysis, we observe an increase in the Au-Pd coordination number as the Pd content of the catalysts increases. The monometallic Pd/TiO_2 catalyst has a Pd-Pd coordination number of approximately 5, which is the coordination expected for a small particle and is in agreement with the average particle size calculated from STEM images.[77,78]

Table 3.4. Ex-situ EXAFS fits of the Pd K-edge and Au L_3-edge for Pd/TiO_2, $AuPd/TiO_2$, and Au/TiO_2 catalysts.

Catalyst	Edge	Scatter Path	CN[a]	R[b] (Å)	$\Delta\sigma^2$	E_0 (eV)	R factor
Pd/TiO_2	Pd	Pd – Pd	5.4	2.73	0.008	-1.2	0.006
		Pd – O	2.3	1.92			
$AuPd_{0.67}/TiO_2$	Pd	Pd – Pd	1.6	2.86	0.008	13.3	0.015
		Pd – Au	11.0	2.80			
		Pd – O	0.4	1.97			
	Au	Au – Au	9.1	2.85	0.008	8.5	0.039
		Au – Pd	3.1	2.77			
		Au – O	0.2	1.97			
$AuPd_{0.55}/TiO_2$	Pd	Pd – Pd	1.0	2.75	0.008	13.4	0.002
		Pd – Au	8.6	2.82			
		Pd – O	1.0	2.01			
	Au	Au – Au	10.0	2.85	0.008	7.5	0.051
		Au – Pd	2.2	2.80			
		Au – O	0.6	1.98			
$AuPd_{0.23}/TiO_2$	Pd	Pd – Pd	1.0	2.63	0.008	12.8	0.057
		Pd – Au	10.8	2.81			
		Pd – O	0.6	2.04			
	Au	Au – Au	9.9	2.84	0.008	5.1	0.061
		Au – Pd	0.7	2.82			
		Au – O	0.5	1.90			
$AuPd_{0.06}/TiO_2$[c]	Au	Au – Au	10.0	2.82	0.008	4.0	0.035
		Au – Pd	0.6	2.85			
		Au – O	0.4	1.91			
Au/TiO_2	Au	Au – Au	8.8	2.85	0.008	5.4	0.015
		Au – O	0.2	2.06			

[a] Coordination number, estimated uncertainty ± 20%

[b] Distance between the absorber and back-scatterer, estimated uncertainty ± 0.02 Å

[c] Data too noisy to obtain quality fits for the Pd edge

3.2.3 Reactivity Trends

Scheme 3.1 shows a representation of the reaction network for the hydrogen borrowing-mediated amination of 1-hexanol using ammonia.[6,7] We were able to identify hexane, hexylamine, hexanenitrile, *N*-hexylidene hexylamine (the secondary aldimine), dihexylamine, and trihexylamine as products by GC-FID and GC-MS. The aldehyde (hexanal) and primary aldimine (hexylimine) intermediates were not observed by GC-FID or GC-MS techniques. We attribute their absence to their high reactivity and the large molar excess of ammonia (NH_3/hexanol = 36) used: under these conditions, any hexanal formed would react with ammonia on the catalyst surface to form the 1° aldimine since aldehyde-aldimine interconversion is typically equilibrated. The reactive 1° aldimine would then be converted to more stable products. Gaussian-based thermochemical calculations of the two-carbon analogs show that both hexanenitrile and hexylamine are favored at equilibrium (see Appendix Table A.2).

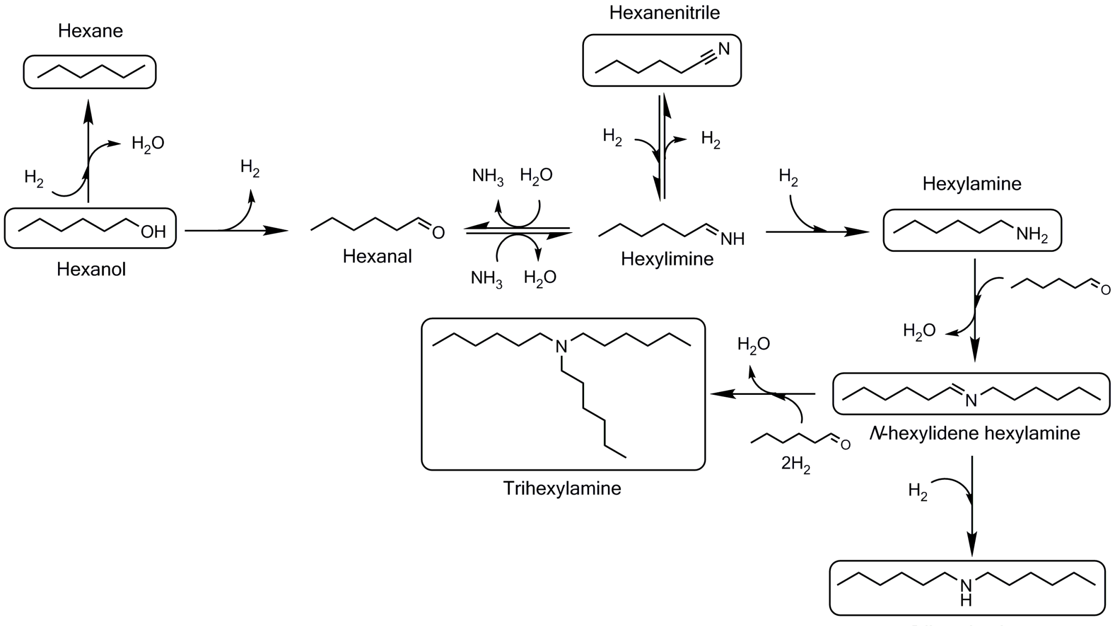

Scheme 3.1 Reaction network for the amination of 1-hexanol using ammonia. Boxed species were identifiable (by GC-FID and GC-MS) and quantified in this work.

Hexanol conversion rates based on product formation at 16-25% hexanol conversion are shown versus time-on-stream for the various catalysts in Appendix Figure A.3. From the time-on-stream data, it is apparent that most of the catalysts are stable over the time periods studied, typically about 8 hours. We compare catalysts using measurements after about two hours on-stream, after which point catalyst deactivation was minimal. Although ammonia and hydrogen bind more strongly to Pd than hexanol and could poison those sites, the stability of the catalyst over at least 8 hours indicates that sufficient vacant sites are available at steady state for hexanol binding.

Comparisons of the hexanol conversion rates and site-time yields (based on product formation) over the various catalysts are shown in Table 3.5. The rate of hexanol conversion increases from 8.7 μmol ks^{-1} (μmol total Pd)$^{-1}$ on Pd/TiO_2 to between 12 and 42 μmol ks^{-1} (μmol total Pd)$^{-1}$ on the bimetallic catalysts. The highest rate (per total Pd) is observed on the $AuPd_{0.06}/TiO_2$ catalyst, which exhibits a rate nearly 5 times higher than that over Pd/TiO_2.

To determine the reactivity of Au in the conversion of hexanol over the bimetallic catalysts, we also calculate rates with respect to the Au metal content. The introduction of Pd to the Au parent increases the rate of hexanol conversion slightly from 3.0 μmol ks^{-1} (μmol total Au)$^{-1}$ on Au/TiO_2 to 5.3 μmol ks^{-1} (μmol Au)$^{-1}$ on $AuPd_{0.23}/TiO_2$. A further rate enhancement to 11 μmol ks^{-1} (μmol Au)$^{-1}$ is observed as the Pd loading increases to Pd/Au = 0.55. The rate decreases slightly to 7.9 μmol ks^{-1} (μmol Au)$^{-1}$ as the Pd/Au ratio is further increased to 0.67 and this trend is attributed to the higher fraction of contiguous Pd ensembles, discussed in more detail below. Thus, independently of whether the rate is normalized by total Au or Pd content, we observe an increase in activity for bimetallic catalysts over monometallic catalysts. Since the Au parent catalyst is identical for all the bimetallic catalysts, the differences in reactivity as the Pd loading changes must be attributed to changes in either the intrinsic activity of Pd or to changes in Au activity because of interaction with Pd. We note that when the rate is normalized by the total metal content, rather than surface metal, the highest rate is observed for the Pd/TiO_2 catalyst. This result can be attributed to the higher dispersion for this catalyst – a higher fraction of the active species is accessible.

Table 3.5. Rate of hexanol conversion and site-time yields (STY) for hexanol amination. The hexanol conversion rate is calculated as the sum of product formation rates, weighted by the number of moles of hexanol needed to form one mole of product. Conditions: 503 K, 1 atm (6.9×10^{-4} atm hexanol, 0.25 atm NH_3, 0.5 atm H_2, and balance He), 16-25% hexanol conversion.

Catalyst	**Rate / µmol ks^{-1} (µmol total Pd)$^{-1}$**	**Rate / µmol ks^{-1} (µmol total Au)$^{-1}$**	**Rate / µmol ks^{-1} (µmol total metal)$^{-1}$**	**STY / ks^{-1} [Pd sites] [a]**	**STY / ks^{-1} [total surface metal] [b]**
Au/TiO_2	N/A	3.0	3.0	N/A	5.6
$AuPd_{0.06}/TiO_2$	42	2.2	2.1	1200	9
$AuPd_{0.23}/TiO_2$	22	5.3	4.3	340	13
$AuPd_{0.55}/TiO_2$	21	11	7.3	340	45
$AuPd_{0.67}/TiO_2$	12	7.9	4.7	300	45
Pd/TiO_2	8.7	N/A	8.7	77	12

[a] STY for AuPd and Pd catalysts calculated from surface Pd sites determined by CO chemisorption.
[b] Total surface metal site density to calculate STY was calculated using the average particle size as determined by STEM. For the Au and AuPd catalysts dispersion was calculated using *D=1.16/d* and for the Pd catalyst, *D=1.11/d* was used. (Ref. 43)

The above results suggest that AuPd bimetallic formation creates new catalytic sites that are more active for hexanol amination than either monometallic Au or Pd sites. We note that bimetallic moieties exhibiting favorable electronic interactions and/or ensemble effects comprise the active sites regardless of whether, mechanistically, Au promotes Pd catalysis, Pd promotes Au catalysis, or both metals directly participate in the chemistry.

The coordination numbers as determined by EXAFS indicate that Pd is highly coordinated to Au, while the Au coordination to Pd is much lower. This stems from the low Pd/Au ratio, and thus each surface

Pd likely exists in a bimetallic ensemble, while only a fraction of the surface Au is part of a bimetallic site. Thus, we expect that the number of surface bimetallic active sites will be proportional to the number of surface Pd sites. To calculate site-time yields (for Pd-containing catalysts), we may normalize the rates by the number of Pd surface species as measured by CO chemisorption (Table 3.5). Based on Pd sites, the hexanol conversion STY over $AuPd_{0.06}/TiO_2$ exceeds that of Pd/TiO_2 by two orders-of-magnitude, from 77 ks^{-1} to 1200 ks^{-1}. At intermediate Pd/Au ratios ranging from 0.23 to 0.67, the STY promotion is more modest.

Site-time yields can also be calculated using site densities of total surface metal, as determined from the STEM average particle size, shown in Figure 3.4. For all Au containing catalysts, the total number of surface metal sites can be approximated using sites calculated by the catalyst particle size determined from STEM using $D = 1.16/d$. Similarly, the total number of surface metal sites for the Pd/TiO_2 catalyst was calculated from the Pd/TiO_2 particle size using $D=1.11/d$.[43] By this normalization, the hexanol conversion STY increases as the Pd loading in the bimetallic catalysts increases. The highest STY of 45 ks^{-1} is observed over the $AuPd_{0.55}/TiO_2$ and $AuPd_{0.67}/TiO_2$ catalysts, with total-surface STYs that are 5.6 and 3.8 times higher than that of Au/TiO_2 and Pd/TiO_2, respectively. We note that the standard deviation for the average particle size is higher on the AuPd catalysts than the monometallic Au catalyst, and thus the error in the calculated STY is also increased for the bimetallic catalysts.

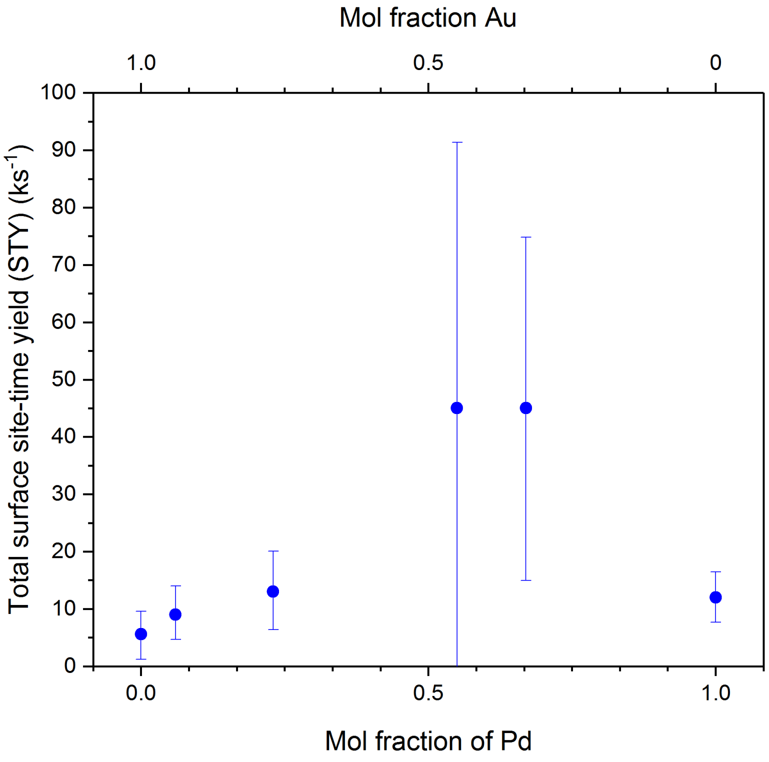

Figure 3.4. Total-surface site-time yield (STY) of hexanol conversion as a function of Pd and Au mol fraction. The STY values were calculated using total surface metal as estimated by the average particle size of each catalyst determined by STEM. Errors bars represent the STY calculated using sites from the average particle size ± standard deviation. Conditions: 503 K, 1 atm (6.9 x 10^{-4} atm hexanol, 0.25 atm NH_3, 0.5 atm H_2, and balance He), 16-25% hexanol conversion.

Based on chemisorption and FTIR results, we know that the number of accessible Pd sites, which we assume to be bimetallic sites, increases with increasing Pd loading. Thus, the increase in STY when a higher fraction of the total surface sites are bimetallic sites, rather than Au sites, corroborates our conclusion that the bimetallic AuPd sites are responsible for enhanced activity. This result is in agreement with previously reported Au-Pd synergy for the AuPd/TiO_2-catalyzed hydrogen-borrowing amination of alcohols using nitrobenzene.[41]

Figure 3.5a shows the site-time yields for the formation of each product observed for the various Au-Pd catalysts, based on total surface metal to allow for comparison of Au activity to Pd-containing catalysts. Particularly noteworthy is the presence of trihexylamine, because it cannot be formed via the previously described amination pathway: dihexylamine lacks a second nitrogen-bonded H atom, which is necessary to eliminate water from the hemiaminal adduct of hexanal and an amine to form the corresponding imine. Instead, a dehydration-hydrogenation sequence and/or a direct hydrogenolysis pathway must be kinetically accessible, and probably contributes to the formation of all three amines.

A comparison of product selectivity over $AuPd_{0.06}/TiO_2$ at 7 and 17% conversion provides insight into the formation of trihexylamine, as seen in Figure 3.6. At lower conversion, the selectivity to hexanenitrile increases, indicating that the reaction of hexylimine to hexanenitrile is equilibrated with equilibrium favoring hexanenitrile. This result is substantiated by our Gaussian calculations, from which the equilibrium constant for hexylimine dehydrogenation to hexanenitrile is estimated to be $1.7x10^3$ (Appendix Table A.2). The production of dihexylamine decreases to essentially zero at low conversion, while the trihexylamine selectivity increases at low conversion. This behavior indicates that trihexylamine cannot be formed via dihexylamine, but instead must pass through the 2° imine species (Scheme 3.1). At 7% conversion, we observe no hexylamine while at 16% conversion, the hexylamine production over the $AuPd_{0.06}/TiO_2$ catalyst is low. It is well established that the formation of imines takes place via the reaction of an aldehyde and amine[1,6,79] and thus hexylamine is necessary for the formation of *N*-hexylidene hexylamine. In this case, we can rationalize the small amount of hexylamine by its rapid conversion to further products and its low sensitivity for detection in the GC analysis. Based on these experiments, we hypothesize that hexylamine is converted to N-hexylidene hexylamine and that the formation of trihexylamine occurs via reaction of hexanal and the 2° imine.

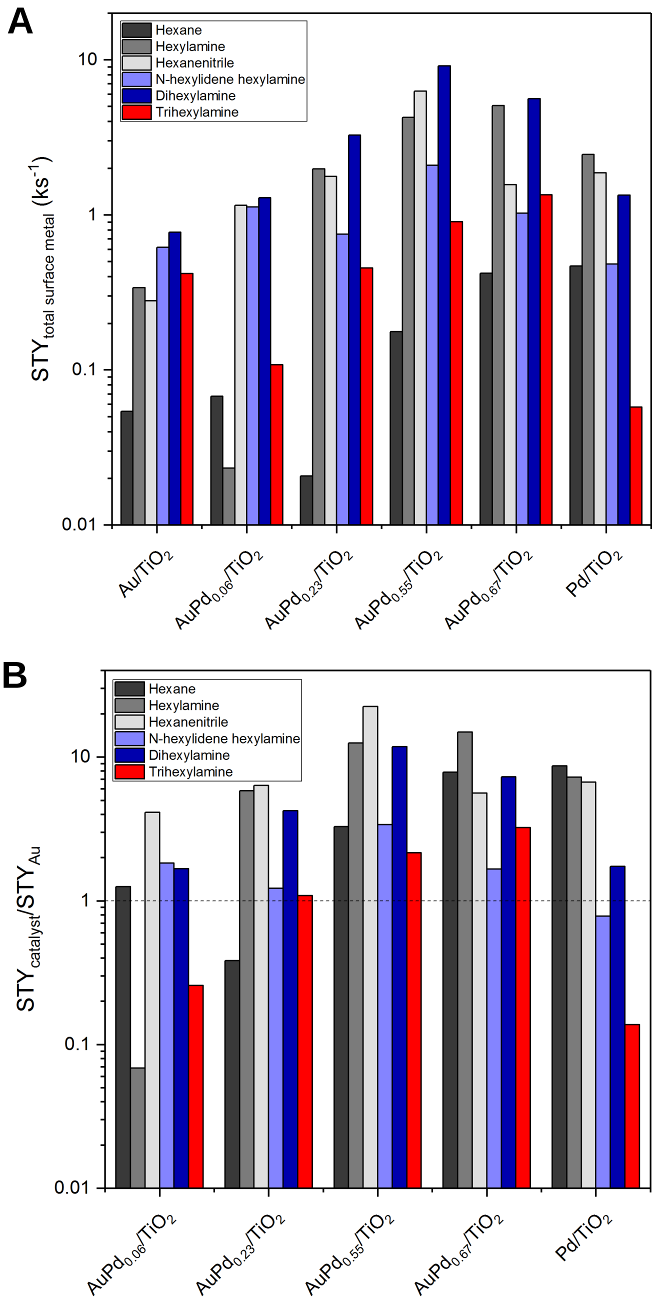

Figure 3.5. (a) Site-time yield of product formation based on the total surface metal of each catalyst. The total surface metal was determined using the particle size for each catalyst, and *D = 1.16/d* for the Au containing catalysts and *D = 1.11/d* for the Pd catalyst. (b) The rate enhancement of each product formation, as calculated by the ratio of the product site-time yield of each catalyst to the product site-time yield over Au/TiO$_2$. Conditions: 503 K, 1 atm (6.9 x 10^{-4} atm hexanol, 0.25 atm NH$_3$, 0.5 atm H$_2$, and balance He), 16-25% hexanol conversion.

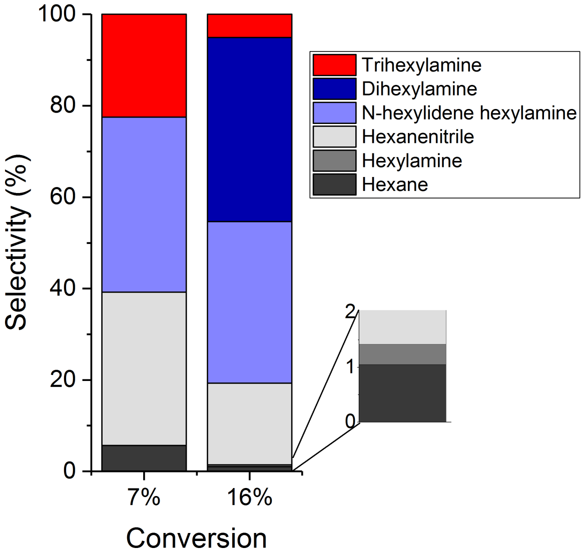

Figure 3.6. Effect of hexanol conversion on product selectivity on hexanol amination product distribution for $AuPd_{0.06}/TiO_2$.

We now consider the change in product distribution which arises from the addition of Pd to the Au parent catalyst. As Pd is added in increasing amounts to the Au parent catalyst, the rate of formation of the products increases, but not uniformly. The ratio of the STY of each product on the AuPd catalyst to the STY on the Au catalyst, i.e. the rate enhancement of product formation upon the addition of Pd, is shown in Figure 3.5b. As the Pd/Au ratio increases from 0.06 to 0.55, the largest enhancement in rate among the amination products is observed for the production of hexylamine and hexanenitrile. The production of dihexylamine is also enhanced as Pd content increases, but to a lesser extent. We note that as the Pd content is further increased to a ratio of Pd/Au = 0.67, the rate enhancement of hexanenitrile and dihexylamine decreases.

Additionally, the monometallic Pd/TiO_2 catalyst exhibits a higher STY for the production of hexylamine and hexanenitrile than Au/TiO_2; however, the extent of rate enhancement is lower than that of the bimetallic catalysts. Moreover, the undesirable rate of hexane production over the Pd/TiO_2 catalyst is the highest of all catalysts studied. Thus, the presence of Au reduces this undesirable hydrogenolysis activity and increases the rate of hexanol dehydrogenation to hexanal.

The product distribution may be further analyzed by considering the selectivity trend. As shown in Figure 3.7, primary amination products are generally favored (and substituted products disfavored) with increasing Pd fraction. This behavior is of practical interest since primary amines are more useful than substituted amines as feedstocks for other reactions.[80,81] Furthermore, although the hexane production rate increases with Pd content, hexane selectivity is maintained at ≤1.1% for all Au-containing catalysts.

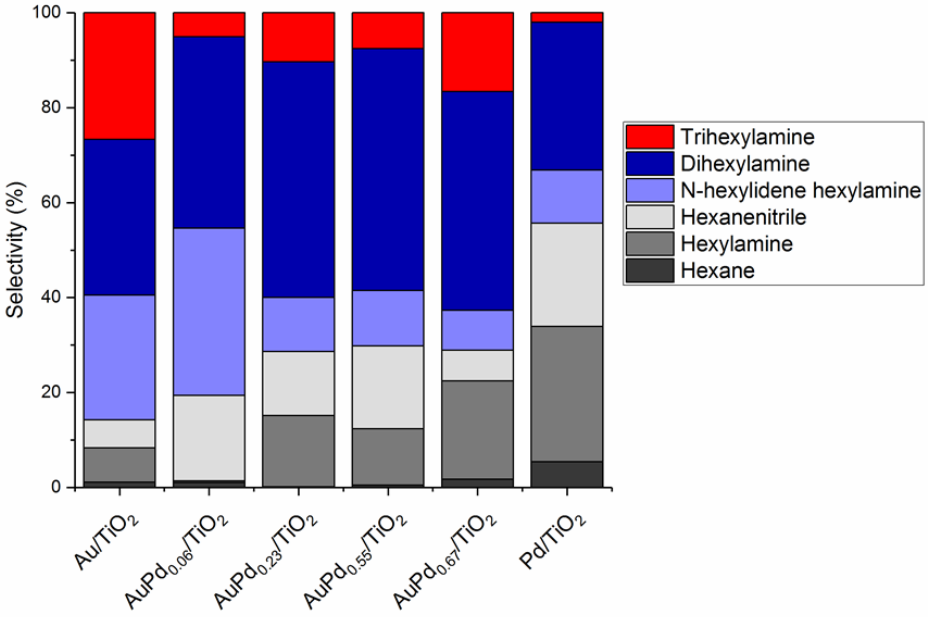

Figure 3.7. Effect of bimetallic composition on the hexanol amination product distribution over titania-supported AuPd catalysts. Here, the selectivity of species *j*, $\boldsymbol{S_j}$, is defined as $\boldsymbol{S_j = \nu_j R_j / \sum_k \nu_k R_k}$; where $\boldsymbol{\nu_j}$ is defined as the number of hexanol molecules required to form species $\boldsymbol{j}$ (*i.e.*, 1, 2, or 3 for primary, secondary, and tertiary products, respectively), and $\boldsymbol{R_j}$ gives the production rate of species *j*. Primary, secondary, and tertiary products are color-coded as gray/black, blue, and red, respectively. Conditions: 503 K, 1 atm (6.9×10^{-4} atm hexanol, 0.25 atm NH_3, 0.5 atm H_2, and balance He), 16-25% hexanol conversion.

Both electronic and ensemble effects have been previously reported to enhance reactivity over AuPd catalyst systems. In our catalyst system, the position of the FTIR band for CO adsorbed on Pd suggests an electronic interaction between Au and Pd, while the change in the dominant binding mode for CO adsorbed on Pd also suggests a change in the geometric structure of accessible Pd. Accordingly, both ensemble and electronic effects could induce the observed reactivity trends. We now discuss possible explanations for these ensemble and electronic effects in AuPd-catalyzed hexanol amination and analyze the extent to which various reaction kinetics principles can rationalize the bimetallic synergy.

The enhancement observed in the rate of hexanol conversion over the bimetallic catalysts may be attributed to geometric changes in Pd structure upon dilution in Au. From FTIR spectra of adsorbed CO, the dominant CO binding mode on the bimetallic catalysts suggests that isolated Pd species surrounded by Au are primarily present. Density functional theory calculations of methanol amination using ammonia on a Pd surface have shown that the binding energy and adsorbed structure change upon inclusion of co-adsorbed NH_3.[4] When NH_3 is present, the adsorbed intermediates form a hydrogen bond with ammonia and are thus stabilized. As a result, the activation energy for several steps increases, and the overall rate is predicted to decrease compared to a clean surface. Ammonia binds more weakly to Au than Pd. Thus, for the AuPd bimetallic catalysts with primarily isolated Pd sites, we do not expect NH_3 to bind sufficiently close to other intermediates on Pd sites to allow for formation of hydrogen bonds. As a result, the rate of hexanol conversion over AuPd catalysts is higher than the rate over a monometallic Pd catalyst, where stabilization of intermediates by co-adsorbed NH_3 is expected to occur. This behavior suggests that the geometric structure of the bimetallic AuPd catalysts is in part responsible for the enhanced rate of hexanol conversion.

The observed selectivity trend can be explained as the result of increased catalyst turnover frequency. According to transition state theory, the thermodynamic activities of reactive intermediates, rather than idealized concentrations, govern reaction rates.[82,83] It follows that for changes in catalyst composition to affect product distributions, those changes must modulate the relative activities of surface intermediates and transition states within the amination network. In the case of ammonia, if we make the assumption that adsorption is quasi-equilibrated, then the activity of adsorbed ammonia is pinned to be equal to that of gas-phase ammonia, which is independent of catalyst composition and is fixed by the reaction conditions (temperature, pressure, and gas composition); the same principle applies to hexanol. In this respect, we can consider the rather complex amination network to consist of two phases: (1) initial hexanol dehydrogenation and ammonia adsorption, followed by (2) a pool of reactive intermediates mutually interconverting via not-necessarily-equilibrated reactions. Because surface-bound hexanal and ammonia are the only species to enter the pool, and species may only exit as one of the stable products shown in Scheme 3.1, the prevailing product distribution will be governed by the activities of adsorbed hexanal and ammonia (as well as relevant kinetic and thermodynamic parameters). In particular, increasing the ratio of hexanal activity to ammonia activity would increase the substitution of resultant amination products. We have already discussed that the activity of ammonia is likely to be fixed by that of the gas phase. Under steady-state operation, surface-bound hexanal is produced by hexanol dehydrogenation, and is consumed at an equal rate by the combined reactions within the reactive intermediate pool. It follows that increasing the *intrinsic* dehydrogenation rate (and thus the overall rate) will increase the number of steady-state surface-bound hexanal molecules. As a condition for thermodynamic stability,[84] this in turn raises the chemical potential (or, equivalently, activity) of adsorbed hexanal. Accompanied by an unchanged ammonia activity, the increased hexanal activity naturally leads to the formation of higher-substituted products within the reactive pool.

By comparing the Pd-based STY trend to the selectivity trend, we observe that, for the Pd-containing catalysts, increasing hexanol conversion STYs are accompanied by increasing selectivities towards secondary and tertiary products. Thus, the idea of a kinetically determined activity of surface-bound hexanal can rationalize the observed relationship between site-time yield (our proxy for intrinsic reactivity) and product substitution.

We note that the monometallic Au/TiO_2 catalyst does not align with the trend predicted by the kinetically determined hexanal activity framework, since its Au-based conversion site-time yield is the lowest among all catalysts despite it producing the greatest fraction of highly substituted products. This discrepancy could be a reflection of inaccurate site-normalization on the Au/TiO_2 catalyst. While we have approximately normalized to the total number of surface Au atoms, Au catalysis is often mediated by just the defect sites, and smaller particles have been observed to be more active than larger ones for hydrogen borrowing amination over Au/TiO_2 catalysts using urea as the nitrogen source.[85] Thus, it cannot be ruled out that only a small subset of the Au defects is catalytically active, such as those vicinal to the titania support or within a particular multi-atom moiety, which could reconcile the Au/TiO_2 discrepancy.

Based on the overall discussion above, we suggest that geometric effects primarily govern the reactivity trend, and that the reactivity and selectivity trends may be intrinsically coupled.

3.3 Conclusions

AuPd/TiO_2 catalysts have been synthesized using controlled surface reactions across a range of Pd/Au ratios. It was determined that by using low concentrations of Cp(Pd)allyl during synthesis, Pd species were deposited onto Au nanoparticles, forming intimate bimetallic particles. EDS analysis indicates the absence of monometallic Pd nanoparticles on the catalysts with Pd/Au ratios between 0.06 and 0.67. CO chemisorption studies indicate that the AuPd nanoparticles contain Pd both on the surface and in the bulk of the particle and infrared spectra of adsorbed CO suggest that Au influences the Pd electronically. Furthermore, compared to a monometallic Pd catalyst, CO adsorbs on the Pd in the bimetallic catalysts in a predominantly linear configuration, indicating that Pd is well dispersed in the Au. Evidence from XAS experiments also supports this conclusion.

The comparison of product distributions over $AuPd_{0.06}/TiO_2$ at different conversions indicates that trihexylamine, which cannot be formed via the condensation of hexanal and dihexylamine, is instead formed via the secondary aldimine intermediate, *N*-hexylidene hexylamine. Additionally, the AuPd catalysts exhibit higher hexanol conversion site-time yields than the monometallic catalysts for gas-phase hexanol amination. The formation of primary species (i.e., hexylamine and hexanenitrile) is also preferentially enhanced as Pd is increasingly added to Au. Given that CO FTIR experiments demonstrate that both electronic and ensemble effects are possible, reaction kinetics principles were used to augment our understanding of potential Au-Pd alloying effects. On this basis, we suggest that hexanol conversion rates are primarily influenced by ensemble effects, whereas selectivity may be susceptible to both electronic and ensemble effects.

3.4 Materials and Methods

3.4.1 Catalyst Synthesis

A monometallic, 1 wt% Au/TiO_2 parent catalyst was synthesized using a deposition precipitation method, as described in Section 2.1.3. A monometallic Pd/TiO_2 catalyst was synthesized by incipient wetness impregnation, described in Section 2.1.2.

Bimetallic AuPd/TiO_2 catalysts were synthesized using controlled surface reactions, a method developed in previous work for other multimetallic systems[24,86–89] and described in detail in Section 2.1.4. The $AuPd_{0.06}/TiO_2$ and $AuPd_{0.23}/TiO_2$ catalysts were synthesized in one cycle of controlled surface reactions, while the $AuPd_{0.55}/TiO_2$ and $AuPd_{0.67}/TiO_2$ catalysts were synthesized in two cycles.

3.4.2 Characterization

CO Chemisorption

The Pd dispersion was measured by CO (CP Grade, Airgas) chemisorption. Catalyst samples were reduced in flowing hydrogen (Industrial Grade, Airgas) at 533 K for 1 h (with a heating rate of 2 K min^{-1}) prior to analysis. CO adsorption was carried out at 293 K and the number of surface Pd atoms was taken to be equal to the irreversible CO uptake (1 mol CO: 1 mol Pd).

Fourier Transform Infrared Spectroscopy

Infrared spectra of CO adsorbed on catalyst samples were collected using a Nicolet 6700 spectrometer connected to a custom vacuum manifold. Catalyst samples were pressed into self-supporting pellets and loaded into a transmission cell described elsewhere.[90,91] Samples were reduced in flowing hydrogen (Industrial Grade, Airgas) at 573 K then cooled to room temperature and evacuated to 10^{-5} Torr. After a background scan was collected, the cell was cooled to 223 K using flowing liquid nitrogen. Then, 300 Torr of 1 mol% CO in He (Airgas) was introduced to the sample and the sample was further cooled to 103 K. Spectra of adsorbed CO were collected in the temperature range of 103 to 293 K with a resolution of 4 cm^{-1}.

X-ray Absorption Spectroscopy

Ex-situ X-ray absorption spectroscopy (XAS) measurements were taken at beamline 10-ID at the Advanced Photon Source at Argonne National Laboratory. Measurements were taken at the Pd-K edge (24350 eV) and the Au-L_3 edge (11919 eV). Samples were pressed into wafers inside a stainless-steel sample holder, which was placed inside a quartz tube with Kapton windows on each end. The tube was flushed with helium prior to analysis and spectra were collected in transmission mode. For the catalyst with the lowest Pd loading (Pd/Au = 0.06), a poor signal-to-noise ratio at the Pd edge in transmission mode prohibited quantitative analysis of the Pd species. Spectra of Au and Pd foils were collected with each sample to calibrate the energy. Fitting of spectra was performed using the Demeter software package over an R range of 1.4-3.4 Å and a k-range of 3-10 $Å^{-1}$. The amplitude reduction factor was determined to be $S_0^2 = 0.82$ for Au and $S_0^2 = 0.86$ for Pd by fitting the spectra of the reference foils.

3.4.3 Reactivity Studies

Reactivity studies for the gas-phase amination of 1-hexanol using ammonia were conducted in a 0.7-inch OD fixed bed, borosilicate glass flow reactor operated in a down-flow configuration. In each run, the catalyst (typically between 5 and 25 mg) was diluted in 1.5 g of silica chips (Silicon Dioxide, fused (granular), 4-20 mesh, 99.9% trace metals, Sigma-Aldrich), which had been crushed and sieved to between 106 and 212 µm to mitigate channeling artifacts. Prior to each reaction, catalysts were reduced under flowing H_2 (Industrial Grade, Airgas) at 533 K for 1 h with a heating rate of 2 K min^{-1}. All reactions were conducted at 503 K and 1 atmosphere total pressure with a gas composition of 6.9×10^{-4} atm hexanol, 0.25 atm NH_3, 0.5 atm H_2, and balance He. The high H_2 pressure was required to achieve sufficiently high hexanol conversion. The reactor temperature was read using a K-type thermocouple seated in a well (which extended into the catalyst bed) in the wall of the reactor. Temperature control was achieved using a resistively heated furnace connected to a variable autotransformer supplied by a self-tuning PID process controller (Series 16A, Love Controls). To prepare the gas mixture, a flow of 20 cm^3(STP) min^{-1} hydrogen was sparged through a 1-hexanol (≥99%, Sigma-Aldrich) saturator maintained at 303 K using a heated circulating bath. A flow of 20 cm^3(STP) min^{-1} of 5 mol% NH_3 in He (Airgas) was mixed with the hexanol-saturated hydrogen stream in a tee union (heated to avoid hexanol condensation) directly upstream of the reactor. To trap all products, the reactor effluent was fed to a borosilicate glass trap filled with 1-butanol (99.9% HPLC Grade, Sigma-Aldrich) and immersed in an ice-water bath. Using a simplified variant of the method of Jou and Freeman,[92] the butanol was purified by refluxing with $NaBH_4$ (>98%, Sigma-Aldrich) (1.3 g $NaBH_4$ per L of butanol) at 323 K under bubbling Ar, followed by distillation; the middle fraction was taken for use. To quantify product formation, the reactor was periodically (approximately every 2 h) isolated, during which time the butanol-containing product trap was replaced with another equivalent one. The butanol solution from the just-removed trap was then injected on a gas chromatograph (Shimadzu GC-2010) equipped with a flame-ionization detector (hereafter referred to as GC-FID) and a Zebron ZB-50 column (30 m x 0.25 mm OD, Phenomenex). All product identification was substantiated by comparison to analytical standards and mass spectrometry using a Shimadzu GCMS-QP2010 S. Only data reflecting steady-state catalytic reactivity are reported. All reactions were carried out at fractional hexanol conversions ranging from 16-25%; however, due to the high sensitivity of hexanol conversion to fraction-of-a-degree uncertainty in the saturator temperature, total hexanol conversion rates were computed based on the appropriate linear combination of production rates of all products observable by GC-FID and GC-MS techniques. Additionally, due to the complexity of the reaction network, reactivity is reported in terms of site-time yields (STY), which are the rates at which products are formed per *defined* catalyst site (where different methods are used to count sites). After each reaction, the reactor was cleaned by soaking in nitric acid to be used again.

3.5 Acknowledgements

This material is based upon work supported by the U.S. Department of Energy, Office of Basic Energy Sciences (DE-SC00114058) and the National Science Foundation Engineering Research Center for

Biorenewable Chemicals (CBiRC) (EEC-0813570). MRCAT operations are supported by the Department of Energy and the MRCAT member institutions. This research used resources of the Advanced Photon Source, a U.S. Department of Energy (DOE) Office of Science User Facility operated for the DOE Office of Science by Argonne National Laboratory under Contract No. DE-AC02-06CH11357. The use of facilities supported by the Wisconsin Materials Research Science and Engineering Center is also acknowledged (DMR-1121288). The authors thank Jeff Miller for useful discussions regarding XAS results, Joe Chada and Siddarth Krishna for their help in obtaining XAS data, and Jake Gold for his assistance with Gaussian calculations.

3.6 References

(1) Bähn, S.; Imm, S.; Neubert, L.; Zhang, M.; Neumann, H.; Beller, M. *ChemCatChem* **2011**, *3*, 1853–1864.

(2) Tomer, A.; Yan, Z.; Ponchel, A.; Pera-Titus, M. **2017**, *356*, 133–146.

(3) Shimizu, K. I.; Kon, K.; Onodera, W.; Yamazaki, H.; Kondo, J. N. *ACS Catal.* **2013**, *3*, 112–117.

(4) Dumon, A. S.; Wang, T.; Ibañez, J.; Tomer, A.; Yan, Z.; Wischert, R.; Sautet, P.; Pera-Titus, M.; Michel, C. *Catal. Sci. Technol.* **2018**, *8*, 611–621.

(5) Kanno, S.; Shimizu, K.; Kon, K.; Tanaka, H.; Sakata, Y.; Hakim Siddiki, S. M. A. *Catal. Today* **2013**, *232*, 134–138.

(6) Hamid, M. H. S. A.; Slatford, P. A.; Williams, J. M. J. *Adv. Synth. Catal.* **2007**, *349*, 1555–1575.

(7) Corma, A.; Navas, J.; Sabater, M. J. *Chem. Rev.* **2018**, *118*, 1410–1459.

(8) Roose, P.; Turcotte, M. G. *Kirk-Othmer Encycl. Chem. Technol.* **2016**, 1–20.

(9) Reif, W.; Franz, L.; Stops, P.; Menger, V.; Becker, R.; Kummer, R.; Winderl, S. Preparation of Amines. 5530127, 1996.

(10) Asprion, N.; Julius, M.; Bey, O.; Werland, S.; Stein, F.; Kummer, M.; Magerlein, W.; Melder, J.-P.; Huyghe, K.; Moors, M. Process for preparing ethylamines and monoisopropylamine. 8766009 B2, 2014.

(11) Tomer, A.; Wyrwalski, F.; Przybylski, C.; Paul, J.-F.; Monflier, E.; Pera-Titus, M.; Ponchel, A. **2017**, *356*, 111–124.

(12) Kyriakou, G.; Boucher, M. B.; Jewell, A. D.; Lewis, E. A.; Lawton, T. J.; Baber, A. E.; Tierney, H. L.; Flytzani-Stephanopoulos, M.; Sykes, E. C. H. *Science* **2012**, *335*, 1209–1212.

(13) Liu, X.; Li, Y.; Lee, J. W.; Hong, C.-Y.; Mou, C.-Y.; Jang, B. W. L. *Appl. Catal. A Gen.* **2012**, *439*–

440, 8–14.

(14) Choudhary, T. V.; Sivadinarayana, C.; Datye, A. K.; Kumar, D.; Goodman, D. W. *Catal. Letters* **2003**, *86*, 1–8.

(15) Furlong, B. K.; Hightower, J. W.; Chan, T. Y. L.; Sarkany, A.; Guczi, L. *Appl. Catal. A, Gen.* **1994**, *117*, 41–51.

(16) Sinfelt, J. H.; Carter, J. L.; Yates, D. J. C. *J. Catal.* **1972**, *24*, 283–296.

(17) Sinfelt, J. H. *J. Catal.* **1973**, *29*, 308–315.

(18) Sinfelt, J. H. *Acc. Chem. Res.* **1977**, *10*, 15–20.

(19) Sinfelt, J. H. *Bimetallic Catalysts: Discoveries, Concepts, and Applications*; John Wiley & Sons: New York, 1983.

(20) Besenbacher, F.; Chorkendorff, I.; Clausen, B. S.; Hammer, B.; Molenbroek, A. M.; Stensgaard, I. *Science* **1998**, *279*, 1913–1915.

(21) Crisafulli, C.; Scirè, S.; Minicò, S.; Solarino, L. *Appl. Catal. A Gen.* **2002**, *225*, 1–9.

(22) Li, D.; Nakagawa, Y.; Tomishige, K. *Appl. Catal. A Gen.* **2011**, *408*, 1–24.

(23) Williams, W. D.; Bollmann, L.; Miller, J. T.; Delgass, W. N.; Ribeiro, F. H. *Appl. Catal. B Environ.* **2012**, *125*, 206–214.

(24) Sener, C.; Wesley, T. S.; Alba-Rubio, A. C.; Kumbhalkar, M. D.; Hakim, S. H.; Ribeiro, F. H.; Miller, J. T.; Dumesic, J. A. *ACS Catal.* **2016**, *6*, 1334–1344.

(25) Bollmann, L.; Ratts, J. L.; Joshi, A. M.; Williams, W. D.; Pazmino, J.; Joshi, Y. V.; Miller, J. T.; Kropf, A. J.; Delgass, W. N.; Ribeiro, F. H. *J. Catal.* **2008**, *257*, 43–54.

(26) Schwartz, T. J.; Johnson, R. L.; Cardenas, J.; Okerlund, A.; Da Silva, N. A.; Schmidt-Rohr, K.; Dumesic, J. A. *Angew. Chemie - Int. Ed.* **2014**, *53*, 12718–12722.

(27) Schwartz, T. J.; Lyman, S. D.; Motagamwala, A. H.; Mellmer, M. A.; Dumesic, J. A. *ACS Catal.* **2016**, *6*, 2047–2054.

(28) Alonso, D. M.; Wettstein, S. G.; Dumesic, J. A. *Chem. Soc. Rev.* **2012**, *41*, 8075.

(29) Sankar, M.; Dimitratos, N.; Miedziak, P. J.; Wells, P. P.; Kiely, C. J.; Hutchings, G. J. *Chem. Soc. Rev.* **2012**, *41*, 8099.

(30) Lu, Q.; Hutchings, G. S.; Yu, W.; Zhou, Y.; Forest, R. V.; Tao, R.; Rosen, J.; Yonemoto, B. T.; Cao, Z.; Zheng, H.; Xiao, J. Q.; Jiao, F.; Chen, J. G. *Nat. Commun.* **2015**, *6*, 6567.

(31) Xie, S.; Choi, S. Il; Lu, N.; Roling, L. T.; Herron, J. A.; Zhang, L.; Park, J.; Wang, J.; Kim, M. J.; Xie, Z.; Mavrikakis, M.; Xia, Y. *Nano Lett.* **2014**, *14*, 3570–3576.

(32) Singh, A. K.; Xu, Q. *ChemCatChem* **2013**, *5*, 652–676.

(33) Wu, J.; Yang, H. *Acc. Chem. Res.* **2013**, *46*, 1848–1857.

(34) Takanashi, T.; Nakagawa, Y.; Tomishige, K. *Chem. Lett.* **2014**, *43*, 822–824.

(35) Takanashi, T.; Tamura, M.; Nakagawa, Y.; Tomishige, K. *RSC Adv.* **2014**, *4*, 28664–28672.

(36) He, W.; Wang, L.; Sun, C.; Wu, K.; He, S.; Chen, J.; Wu, P.; Yu, Z. *Chem. - A Eur. J.* **2011**, *17*,

13308–13317.

(37) Wu, K.; He, W.; Sun, C.; Yu, Z. *Tetrahedron* **2016**, *72*, 8516–8521.

(38) Rodriguez, J. A. *Surf. Sci. Rep.* **1996**, *24*, 223–287.

(39) Campbell, C. T. *Annu. Rev. Phys. Chem.* **1990**, *41*, 775–837.

(40) Ono, Y.; Ishida, H. *J. Catal.* **1981**, *72*, 121–128.

(41) Sankar, M.; He, Q.; Dawson, S.; Nowicka, E.; Lu, L.; Bruijnincx, P. C. A.; Beale, A. M.; Kiely, C. J.; Weckhuysen, B. M. *Catal. Sci. Technol.* **2016**, *6*, 5473–5482.

(42) Ball, M. R.; Rivera-Dones, K. R.; Stangland, E.; Mavrikakis, M.; Dumesic, J. A. *J. Catal.* **2019**, *370*, 241–250.

(43) Bergeret, G.; Gallezot, P. In *Handbook of Heterogeneous Catalysis*; Ertl, G., Knozinger, H., Weitkamp, J., Eds.; VCH Verlagsgesellschaft mbH: Weinheim, 1997; Vol. 438, pp 439–441.

(44) Wei, X.; Yang, X. F.; Wang, A. Q.; Li, L.; Liu, X. Y.; Zhang, T.; Mou, C. Y.; Li, J. *J. Phys. Chem. C* **2012**, *116*, 6222–6232.

(45) Gao, F.; Wang, Y.; Goodman, D. W. *J. Am. Chem. Soc.* **2009**, *131*, 5734–5735.

(46) Gao, F.; Goodman, D. W. *Chem. Soc. Rev.* **2012**, *41*, 8009.

(47) Tauster, S. J.; Fung, S. C.; Garten, R. L. *J. Am. Chem. Soc.* **1978**, *100*, 170–175.

(48) Bracey, J. D.; Burch, R. *J. Catal.* **1984**, *86*, 384–391.

(49) Gubó, R.; Yim, C. M.; Allan, M.; Pang, C. L.; Berkó, A.; Thornton, G. *Top. Catal.* **2018**, *61*, 308–317.

(50) Ruban, A. V.; Skriver, H. L.; Nørskov, J. K. *Phys. Rev. B - Condens. Matter Mater. Phys.* **1999**, *59*, 15990–16000.

(51) Yi, C. W.; Luo, K.; Wei, T.; Goodman, D. W. *J. Phys. Chem. B* **2005**, *109*, 18535–18540.

(52) Simson, S.; Jentys, A.; Lercher, J. A. *J. Phys. Chem. C* **2015**, 2471–2482.

(53) Davis, R. J.; Boudart, M. *J. Phys. Chem.* **1994**, *98*, 5471–5477.

(54) Soto-Verdugo, V.; Metiu, H. *Surf. Sci.* **2007**, *601*, 5332–5339.

(55) Kim, H. Y.; Henkelman, G. *ACS Catal.* **2013**, *3*, 2541–2546.

(56) Gao, F.; Wang, Y.; Goodman, D. W. *J. Phys. Chem. C* **2009**, *113*, 14993–15000.

(57) Seemala, B.; Cai, C. M.; Wyman, C. E.; Christopher, P. *ACS Catal.* **2017**, *7*, 4070–4082.

(58) Xu, C. Q.; Lee, M. S.; Wang, Y. G.; Cantu, D. C.; Li, J.; Glezakou, V. A.; Rousseau, R. *ACS Nano* **2017**, *11*, 1649–1658.

(59) Chiorino, A.; Manzoli, M.; Menegazzo, F.; Signoretto, M.; Vindigni, F.; Pinna, F.; Boccuzzi, F. *J. Catal.* **2009**, *262*, 169–176.

(60) Vannice, M. A.; Wang, S. Y. *J. Phys. Chem.* **1981**, *85*, 2543–2546.

(61) Rainer, D. R.; Xu, C.; Holmblad, P. M.; Goodman, D. W. *J. Vac. Sci. Technol. A Vacuum, Surfaces,*

Film. **1997**, *15*, 1653–1662.

(62) France, J.; Hollins, P. *J. Electron Spectros. Relat. Phenomena* **1993**, *64–65*, 251–258.

(63) Dumas, P.; Tobin, R. G.; Richards, P. L. *Surf. Sci.* **1986**, *171*, 579–599.

(64) Kim, J.; Samano, E.; Koel, B. E. *J. Phys. Chem. B* **2006**, *110*, 17512–17517.

(65) Hollins, P.; Pritchard, J. *Prog. Surf. Sci.* **1985**, *19*, 275–349.

(66) Alba-Rubio, A. C.; Plauck, A.; Stangland, E. E.; Mavrikakis, M.; Dumesic, J. A. *Catal. Letters* **2015**, *145*, 2057–2065.

(67) Bradshaw, A. M.; Hoffmann, F. M. *Surf. Sci.* **1978**, *72*, 513–535.

(68) Giorgi, J. B.; Schroeder, T.; Bäumer, M.; Freund, H.-J. *Surf. Sci.* **2002**, *498*, L71–L77.

(69) Rebelli, J.; Rodriguez, A. A.; Ma, S.; Williams, C. T.; Monnier, J. R. *Catal. Today* **2011**, *160*, 170–178.

(70) Kugler, E. L.; Boudart, M. *J. Catal.* **1979**, *59*, 201–210.

(71) Han, Y. F.; Zhong, Z.; Ramesh, K.; Chen, F.; Chen, L.; White, T.; Tay, Q.; Yaakub, S. N.; Wang, Z. *J. Phys. Chem. C* **2007**, *111*, 8410–8413.

(72) Nørskov, J. K.; Studt, F.; Abild-Pedersen, F.; Bligaard, T. In *Fundamental Concepts in Heterogeneous Catalysis*; John Wiley & Sons, 2014; pp 114–137.

(73) Blyholder, G. *J. Phys. Chem.* **1964**, *68*, 2772–2777.

(74) Hu, P.; King, D. A.; Lee, M. H.; Payne, M. C. *Chem. Phys. Lett.* **1995**, *246*, 73–78.

(75) Loffreda, D.; Simon, D.; Sautet, P. *Surf. Sci.* **1999**, *425*, 68–80.

(76) Yudanov, I. V.; Sahnoun, R.; Neyman, K. M.; Rösch, N.; Hoffmann, J.; Schauermann, S.; Johánek, V.; Unterhalt, H.; Rupprechter, G.; Libuda, J.; Freund, H. J. *J. Phys. Chem. B* **2003**, *107*, 255–264.

(77) De Graaf, J.; Van Dillen, A. J.; De Jong, K. P.; Koningsberger, D. C. *J. Catal.* **2001**, *203*, 307–321.

(78) Frenkel, A. I.; Hills, C. W.; Nuzzo, R. G. *J. Phys. Chem. B* **2001**, *105*, 12689–12703.

(79) Zhang, Y.; Lim, C. S.; Boon Sim, D. S.; Pan, H. J.; Zhao, Y. *Angew. Chemie - Int. Ed.* **2014**, *53*, 1399–1403.

(80) Shimizu, K. I.; Kon, K.; Onodera, W.; Yamazaki, H.; Kondo, J. N. *ACS Catal.* **2013**, *3*, 112–117.

(81) Imm, S.; Neubert, L.; Neumann, H.; Beller, M. *Angew. Chemie - Int. Ed.* **2010**, *49*, 8126–8129.

(82) Madon, R. J.; Iglesia, E. *J. Mol. Catal. A Chem.* **2000**, *163*, 189–204.

(83) Laidler, K. J.; King, M. C. *J. Phys. Chem.* **1983**, *87*, 2657–2664.

(84) Chandler, D. *Introduction to Modern Statistical Mechanics*; Oxford University Press: New York, 1987.

(85) He, L.; Qian, Y.; Ding, R. S.; Liu, Y. M.; He, H. Y.; Fan, K. N.; Cao, Y. *ChemSusChem* **2012**, *5*, 621–624.

(86) Aragão, I. B.; Ro, I.; Liu, Y.; Ball, M.; Huber, G. W.; Zanchet, D. *Appl. Catal. B Environ.* **2018**,

222, 1–2.

(87) Liu, Y.; Göeltl, F.; Ro, I.; Ball, M. R.; Sener, C.; Aragão, I. B.; Zanchet, D.; Huber, G. W.; Mavrikakis, M.; Dumesic, J. A. *ACS Catal.* **2017**, *7*, 4550–4563.

(88) Ro, I.; Liu, Y.; Ball, M. R.; Jackson, D. H. K.; Chada, J. P.; Sener, C.; Kuech, T. F.; Madon, R. J.; Huber, G. W.; Dumesic, J. A. *ACS Catal.* **2016**, *6*, 7040–7050.

(89) Hakim, S. H.; Sener, C.; Alba-Rubio, A. C.; Gostanian, T. M.; O’Neill, B. J.; Ribeiro, F. H.; Miller, J. T.; Dumesic, J. A. *J. Catal.* **2015**, *328*, 75–90.

(90) Shen, J.; Hill, J. M.; Watwe, R. M.; Spiewak, B. E.; Dumesic, J. A. *J. Phys. Chem. B* **1999**, *103*, 3923–3934.

(91) Carrasquillo-Flores, R.; Ro, I.; Kumbhalkar, M. D.; Burt, S.; Carrero, C. A.; Alba-Rubio, A. C.; Miller, J. T.; Hermans, I.; Huber, G. W.; Dumesic, J. A. *J. Am. Chem. Soc.* **2015**, *137*, 10317–10325.

(92) Jou, F. Y.; Freeman, G. R. *J. Phys. Chem.* **1977**, *81*, 909–915.

Chapter 4. Hydrodechlorination of 1,2-dichloroethane on Supported AgPd Catalysts

This chapter is adapted from: Ball, M. R.; Rivera-Dones, K. R.; Stangland, E.; Mavrikakis, M.; Dumesic, J. A. *J. Catal.* **2019**, *370*, 241–250.

4.1 Introduction

Hydrodechlorination is an attractive process for the treatment of toxic chlorinated waste to produce valuable hydrocarbon products.[1,2] This process offers a more environmentally friendly alternative to the typical incineration used to treat and remove halogenated waste.[3] The hydrodechlorination of many species, including 4-chlorophenol,[4] dichlorodifluoromethane,[5] 1,2-dichloroethane,[5,6] 1,2- and 1,3-dichloropropane,[6,7] and trichloroethene,[8,9] has been previously studied using a range of catalysts. As one example, 1,2-dichloroethane (1,2-DCA) is used in the industrial production of vinyl chloride[6] and its gas phase hydrodechlorination can produce primarily non-chlorinated hydrocarbons. Group VIII metals, such as Pt, Pd, and Rh, have been previously shown to be active for this reaction.[1,6,10–13] The dechlorination typically occurs via dissociative adsorption of the alkane to break the first C-Cl bond, followed by scission of the second C-Cl bond.[10] The dechlorinated alkene can then either be hydrogenated or desorb to form ethane or ethylene, respectively. The selective production of ethylene is preferred as it is a more valuable feedstock for further use. In the hydrodechlorination of 1,2-dichloroethane, Pt and Pd monometallic catalysts typically achieve high ethane selectivity, and therefore there is interest in the development of catalysts which achieve high ethylene selectivities. It has been demonstrated that the addition of Group IB metals, such as Cu, Au, or Ag, to Pt or Pd catalysts can improve the selectivity of ethylene over ethane.[1,10–18] Luebke et al. demonstrated 95% selectivity to ethylene using $PdCu_3$/C catalysts[19] and nearly 100% selectivity to ethylene was achieved using AgPd/ZrO_2 and AgPd/SiO_2 catalysts with low Pd content.[1,16]

The loadings of the two metals in bimetallic catalysts and the resulting surface structures have been shown to be important in achieving high ethylene selectivity. For AgPd/ZrO_2 catalysts, Han et al. demonstrated that catalysts with low Pd loadings achieved high ethylene selectivity.[16] This result was attributed to an isolation of Pd species in the Ag and the resulting absence of contiguous Pd species. Vadlamannati et al. found that up to 90% selectivity to ethylene was achievable with PtCu catalysts with Pt/Cu ratios less than 1/3.[20] When the Pt/Cu ratio was greater than 1, however, primarily ethane and chloroethane were formed. FTIR experiments with adsorbed ^{12}CO and ^{13}CO indicated that Cu had both a geometric and electronic effect on Pt. Similarly, Rhodes et al. reported a change in product selectivity for hydrodechlorination of 1,2-dichloroethane over PtSn catalysts.[21] When the ratio of Pt/Sn was greater than 1, ethane was the primary product formed, while at Pt/Sn ratios less than 1, the primary product was ethylene. They concluded that Sn rich structures are ethylene selective due to a decrease in the olefin heat of adsorption. These results suggest that selective production of ethylene from 1,2-dichloroethane occurs on bimetallic active sites with intimate contact between the two metals; however, the specific nature of these active sites is unclear.

Although numerous studies in the literature have examined hydrodechlorination reactions over AgPd catalysts,[1,3,10,11,15–18] traditional catalyst synthesis methods produce bimetallic catalysts with a wide range of structures, making it challenging to elucidate structure-activity relationships. Sol-gel techniques,[1,10,11,18] liquid phase surface reduction,[15] and co-impregnation[16] have been used to synthesize AgPd bimetallic catalysts, but it is challenging to create uniform catalysts with these techniques. The structure of the catalyst surface and resulting product selectivity trends can change with synthesis technique.[15] Furthermore, although some work has investigated the effect of the support for dechlorination of CF_2Cl_2 over Pd catalysts,[22] we note that to our knowledge, the effect of catalyst support on bimetallic nanoparticle formation for use in hydrodechlorination of 1,2-dichloroethane has not yet been investigated.

In this work, AgPd catalysts have been synthesized on TiO_2, C, and SiO_2 supports using controlled surface reactions. This synthesis approach allows us to form well controlled bimetallic surface structures, as has previously been shown for a variety of metal systems.[23–30] The range of surface structures formed on these supports at various Pd loadings has allowed us to develop structure-selectivity relationships for the hydrodechlorination of 1,2-dichloroethane, observing high ethylene selectivity when Pd is well isolated because of intimate contact with Ag. Here we measure the interactions between Pd precursor and catalyst support during synthesis and determine that selective deposition of Pd onto Ag during the catalyst synthesis process is most favorable on a TiO_2 support. We characterize the structure of TiO_2, C, and SiO_2 supported catalysts using chemisorption and FTIR techniques. The resulting catalysts are investigated for hydrodechlorination of 1,2-dichloroethane, and we determine that the desirable high selectivity to ethylene can be achieved on catalysts which display AgPd bimetallic sites. We also show that increased turnover frequency of 1,2-dichloroethane consumption is correlated with increased ethylene selectivity.

4.2 Results and Discussion

4.2.1 Catalyst Synthesis

Bimetallic AgPd catalysts were synthesized by depositing Pd onto a Ag parent catalyst. Control experiments were carried out to measure the selective deposition of Pd onto the Ag, rather than the support. A solution of cyclopentadienyl Pd allyl in *n*-pentane was mixed with each support and UV vis spectra of the diluted solutions were measured. The support was allowed to settle and the solution was pulled from the top of the mixture so that no support was present in the solution for UV vis analysis. As shown in Figure 4.1, the extent of interaction between Cp(Pd)allyl and support is dependent on concentration. Figure 4.1a shows a decrease in the peak at 260 nm in the UV vis spectra after 1 h of mixing Cp(Pd)allyl with a TiO_2 support, indicating that Cp(Pd)allyl was deposited on the TiO_2 support. Similar control experiments were carried out on carbon and silica supports and the percentages of Cp(Pd)allyl taken up by the supports are shown in Table 4.1. The calibration curve and corresponding spectra are shown in Appendix Figures B.1 and B.2. In Figure 4.1b, the uptake of the Cp(Pd)allyl precursor in grams is shown as a function of the synthesis concentration. We observe a decrease in the uptake as the synthesis concentration is lowered. This result indicates the importance of maintaining low concentrations of Cp(Pd)allyl during synthesis for all supports. On the TiO_2 support, 95% of the Cp(Pd)allyl was taken up when concentrations of more than 3 mg Cp(Pd)allyl/g pentane were used, but the uptake decreased to 81% when the concentration was lowered to 1.8 mg/g pentane. It was determined that more than 94% of the Cp(Pd)allyl was deposited onto the silica and untreated carbon supports, indicating that selective deposition of Pd onto Ag is unlikely for these supports. When the carbon support was treated at high temperatures prior to use, however, a decrease in the Cp(Pd)allyl uptake was observed, indicating that not all of the precursor was deposited onto the support and thus some deposition of Pd onto Ag would be likely to occur. Therefore, only the carbon treated at high temperatures under H_2 prior to use was used for subsequent catalyst synthesis and will be discussed below. Based on UV vis spectra of the control experiments, Pd is likely to be deposited on the SiO_2 support and may be deposited to some extent on the TiO_2 and treated carbon supports. Therefore, the formation of monometallic Pd species is likely on SiO_2. On the carbon and TiO_2 supports at low concentrations, Pd deposited may be deposited onto the support and/or onto the Ag. To determine whether the formation of monometallic Pd species occurs, additional characterization of the resulting catalysts is necessary.

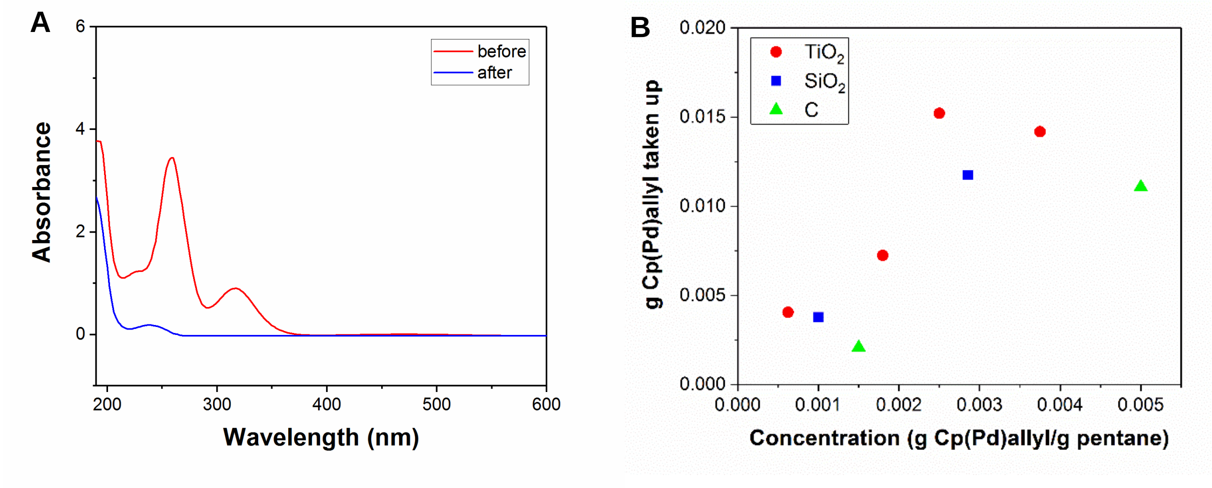

Figure 4.1. (a) UV vis spectra of cyclopentadienyl palladium allyl in n-pentane before and after mixing with TiO2 at a concentration of 1.8 mg/g n-pentane, diluted 67x, (b) the Cp(Pd)allyl taken up by the supports at varied concentrations

Table 4.1. Results of control experiments mixing Cp(Pd)allyl in n-pentane with support materials at room temperature. The Pd adsorbed onto the support is calculated by the change in intensity of the UV vis peak at 260 nm.

Support	**Concentration (mg Cp(Pd)allyl/g pentane)**	**Pd adsorbed onto support[a] (%)**
TiO_2	1.8	81
	3.8	95
High temperature treated carbon	1.5	69
Untreated carbon	1.0	98
SiO_2	1.0	94

[a]% adsorbed is based on intensity of peak at 260 nm

The uptake of Cp(Pd)allyl was also measured during the synthesis process, when Pd is deposited onto the Ag parent catalysts. The concentration of Cp(Pd)allyl using during synthesis and the percentage of precursor taken up by the parent catalyst is shown in Table 4.2, and the corresponding spectra are shown in Appendix Figure B.3. For the TiO_2 supported catalysts, nearly all of the Cp(Pd)allyl is taken up by the Ag parent catalyst, although we note that this uptake could be either onto Ag nanoparticles or the catalyst support. The $AgPd_{0.6}/C$ and $AgPd_{1.3}/SiO_2$ catalysts, however, had some Cp(Pd)allyl remaining in the pentane solution after mixing for 1h. Upon evaporation of the remaining pentane, it is expected that this Pd will be unselectively deposited onto the catalyst support. Additionally, because the control experiments suggest that some Cp(Pd)allyl will be deposited onto the carbon and TiO_2 supports, we expect a portion of the Cp(Pd)allyl to form monometallic Pd species on those supports.

Table 4.2. Concentration of cyclopentadienyl Pd allyl using during synthesis of AgPd catalysts on several supports. The percentage of the Cp(Pd)allyl taken up by the Ag parent catalyst during synthesis was measured by the change in height of the UV vis peak at 260 nm.

Catalyst synthesized	**Concentration (mg Cp(Pd)allyl/g pentane)**	**Pd adsorbed onto Ag parent catalyst[a] (%)**
$AgPd_{1.9}/TiO_2$	4.8	96
$AgPd_{0.5}/TiO_2$	3.0	99
$AgPd_{0.35}/TiO_2$	1.3	80
$AgPd_{1.3}/SiO_2$	3.0	72
$AgPd_{0.6}/C$	1.8	65

[a]% adsorbed is based on the change in the intensity of peak at 260 nm in UV vis spectra

For the most likely formation of bimetallic particles to occur, Cp(Pd)allyl should remain in solution and not be deposited onto the support during control experiments yet be fully deposited onto the Ag parent catalyst during synthesis. Based on evidence from both control and synthesis UV vis spectra, we expect that the formation of bimetallic AgPd particles is most likely to occur on the TiO_2 support when low concentrations are used during synthesis and on the carbon support. When SiO_2 and high concentrations of Cp(Pd)allyl are used with TiO_2, monometallic Pd structures are expected to form. We note that although the control experiments indicated some uptake onto the support for all cases, in the presence of Ag nanoparticles, the Cp(Pd)allyl may preferentially deposit on the Ag rather than the support. Characterization of the resulting bimetallic catalysts is necessary to elucidate the final structure and determine to what extent monometallic Pd nanoparticles were formed.

4.2.2 Catalyst Characterization

The loadings of the bimetallic catalysts, as measured by ICP-AES, are shown in Table 4.3. All Ag parent catalysts have a loading less than 1 wt%, and the molar ratio of Pd/Ag is shown. The average particle size for each catalyst, measured by STEM, is shown and indicates that the addition of Pd to the Ag parent catalyst does not change the particle size significantly. Representative images and the particle size distributions are shown for AgPd catalysts in Figure 4.2. Adsorption experiments were used to measure the accessible surface sites of the Ag parent catalysts, AgPd bimetallic catalysts, and monometallic Pd catalysts for comparison.

Table 4.3. The loading of Ag, Pd, and AgPd catalysts as measured by ICP and the average particle size measured by STEM, averaging at least 800 particles.

Catalyst	Ag loading (wt%)[a]	Pd loading (wt%)[a]	Pd/Ag (mol/mol)	Particle size (nm)
Pd/TiO_2	-	0.59	-	1.44 ± 1.47
$AgPd_{1.9}/TiO_2$	0.78	1.45	1.90	2.37 ± 1.46
$AgPd_{0.5}/TiO_2$	0.64	0.31	0.49	1.97 ± 0.92
$AgPd_{0.35}/TiO_2$	0.52	0.18	0.35	1.62 ± 0.78
Ag/TiO_2	0.55	-	-	2.04 ± 0.95
Pd/SiO_2	-	0.43	-	3.61 ± 1.73
$AgPd_{1.3}/SiO_2$	0.61	0.78	1.31	1.53 ± 0.48
Ag/SiO_2	0.50	-	-	1.99 ± 1.17
Pd/C	-	0.36	-	3.78 ± 3.79
$AgPd_{0.6}/C$	0.47	0.29	0.63	3.28 ± 2.15
Ag/C	0.26	-	-	1.07 ± 0.57

[a] Error in measurement ± 0.3 wt%

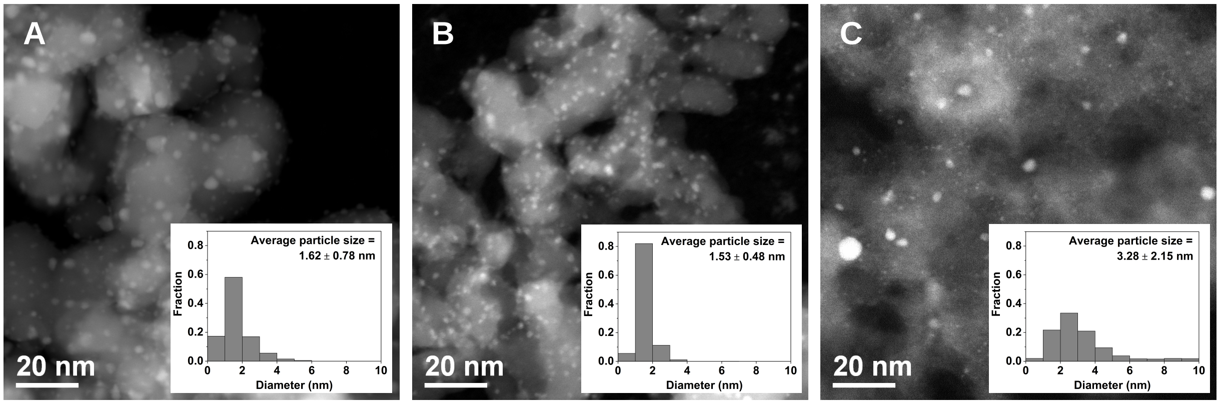

Figure 4.2. Representative STEM images of (a) $AgPd_{0.35}/TiO_2$, (b) $AgPd_{1.3}/SiO_2$, (c) $AgPd_{0.6}/C$ and corresponding particle size distributions.

Ag surface sites were measured by N_2O titration, as shown in Table 4.4. After the addition of Pd to the Ag parent catalysts, the Pd site densities were measured by CO chemisorption, as CO will bind to Pd but not to Ag at room temperature.[31] Appendix Figure B.4 shows the CO-FTIR spectra for CO adsorbed on a Ag/TiO_2 parent catalyst, indicating no uptake of CO by the Ag. A stoichiometric ratio of 1 CO:1 Pd is used since Pd is generally present in isolated species when alloyed. The presence of isolated Pd species in these catalysts is shown by CO-FTIR and discussed further below. We note that Ag and Pd are expected to form alloy structures, not core shell structures, based on consideration of the system phase diagram and similar reduction potential of the two metals.[32,33]

Table 4.4. Adsorption results for Ag, Pd, and AgPd catalysts

Catalyst	**N_2O titration[a] (umol/g)**	**CO uptake (umol/g)[b]**		**Dispersion (%)[c]**
		Reversible CO uptake	**Irreversible CO uptake**	
Pd/TiO_2	-	1.55	5.05	9.1
$AgPd_{1.9}/TiO_2$	-	3.05	11.2	8.2
$AgPd_{0.5}/TiO_2$	-	1.61	3.37	12
$AgPd_{0.35}/TiO_2$	-	0.373	0.123	0.72
Ag/TiO_2	50	-	-	98
Pd/SiO_2	-	0.51	3.11	7.7
$AgPd_{1.3}/SiO_2$	-	3.49	13.4	18
Ag/SiO_2	16	-	-	35
Pd/C	-	0.45	1.02	3.0
$AgPd_{0.6}/C$	-	0.492	1.68	6.2
Ag/C	15	-	-	85

[a] N_2O titration carried out at 443 K using stoichiometry $N_2O + Ag_s \rightarrow Ag_sO + N_2$
[b] CO uptake at 293 K, a stoichiometry of 1 CO:1 Pd is used
[c] Dispersion is calculated from irreversible CO uptake for Pd containing catalysts and sites determined by N_2O titration for Ag catalysts

On the $AgPd/TiO_2$ catalysts, the Pd site density decreases as the loading decreases. The dispersions for the catalysts with Pd/Ag ratios of 0.5 and 2 are similar to that of the monometallic Pd catalyst (around 10%), while a large decrease in dispersion is observed for the Pd/Ag = 0.35 catalyst (to <1%). We hypothesize that more monometallic Pd species are present for the higher Pd loading catalysts. Higher concentrations of Cp(Pd)allyl were used during synthesis to achieve these loadings, and thus Pd is likely to have been deposited on the TiO_2 support rather than only on Ag nanoparticles. At lower loadings and Pd/Ag ratios, nearly all the Pd is expected to be selectively deposited on the Ag nanoparticles. The resulting alloy nanoparticles likely have some surface and mostly subsurface Pd, leading to the lower dispersion. Interestingly, the $AgPd_{0.35}/TiO_2$ catalyst also had a reversible CO uptake higher than the irreversible CO uptake, which suggests that the Pd structures on this catalyst bind CO weaker than the Pd structures on the catalysts with higher Pd loadings. The silica and carbon supported AgPd catalysts have a higher dispersion than that of the monometallic Pd catalysts on those supports. This behavior suggests that Pd may be dispersed on the surface of bimetallic particles, achieving higher dispersion than the monometallic particles. Monometallic Pd particles may also be present in these samples, which we expect based on the UV vis results described above.

FTIR spectra of CO adsorbed on the AgPd/TiO_2 catalysts are shown in Figure 4.3a. The peak at 2052 cm^{-1} is assigned to CO adsorbed in a linear configuration to atop Pd sites.[34] The peak at 1975 cm^{-1} corresponds to CO adsorbed in a bridging configuration.[34,35] CO is adsorbed on atop Pd sites for all TiO_2 supported bimetallic catalysts, with Pd/Ag ratios between 0.35 and 2. The bridge-bonded CO peak, however, is not present for the $AgPd_{0.35}/TiO_2$ catalyst and is weak for the $AgPd_{0.5}/TiO_2$ catalyst. A larger peak appears when the ratio of Pd/Ag is increased to 2. We note that the adsorption of CO onto Ag is weak and thus is not observed at room temperature.[31] Furthermore, when the FTIR spectra are compared with the spectra of adsorbed CO on monometallic Pd/TiO_2 there are several changes. The monometallic Pd catalyst adsorbs CO in a third binding mode, shown by the broad peak at 1917 cm^{-1}. This peak corresponds to CO adsorbed on three-fold Pd sites and indicates larger ensembles of Pd.[36] The absence of this three-fold peak on the bimetallic $AgPd_{0.5}/TiO_2$ and $AgPd_{0.35}/TiO_2$ catalysts indicates that large contiguous Pd ensembles are not present. On the $AgPd_{1.9}/TiO_2$ catalyst, a small amount of CO is adsorbed in this three-fold configuration, indicating larger Pd ensembles on the surface as the Pd content increases.

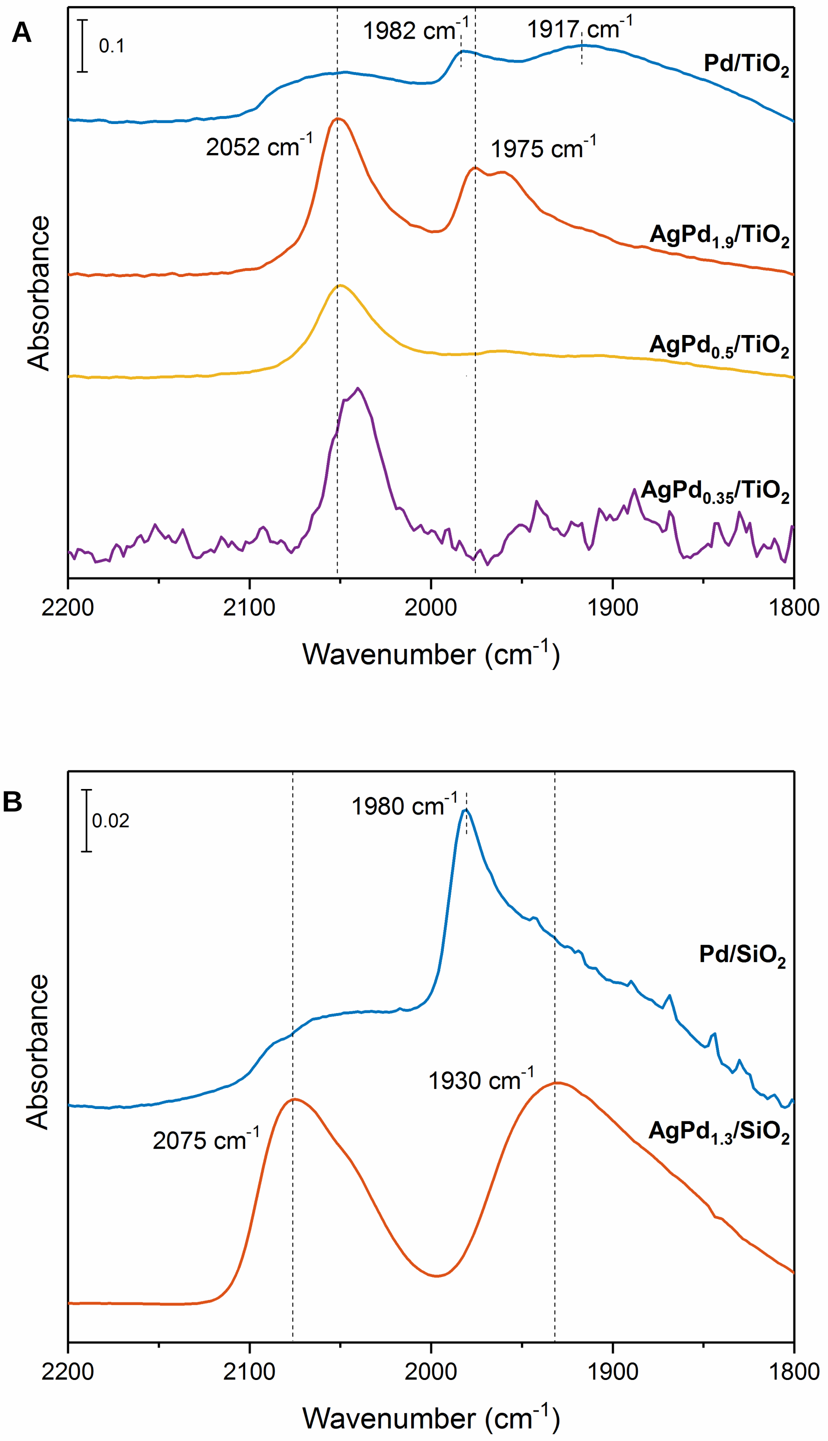

Figure 4.3. FTIR spectra of CO adsorbed on (a) TiO_2 supported and (b) SiO_2 supported Pd and AgPd catalysts. Catalysts were reduced in H_2 at 473 K prior to introduction of 1% CO until the catalyst surface was saturated with CO. Spectra were collected under vacuum to remove gas phase and weakly adsorbed CO species. Spectra are normalized by the pellet density and Pd site density as determined by CO chemisorption.

The aforementioned changes in the dominant binding mode for CO indicate a change in the Pd surface structure as the Pd loading changes for AgPd/TiO_2 catalysts and compared to monometallic Pd. When both top and bridging sites are available, CO binds more strongly to bridge sites.[37] Therefore, the presence of almost entirely linear CO binding for $AgPd_{0.35}/TiO_2$ and $AgPd_{0.5}/TiO_2$ indicates that Pd atoms are primarily isolated from each other and surrounded by Ag atoms such that bridging adsorption sites are not available. These isolated Pd species are not single atom species on the support, but instead are Pd atoms that have been diluted in the Ag nanoparticles. For these AgPd bimetallic catalysts, isolated Pd species are Pd atoms which have primarily Ag neighboring atoms and few to no Pd neighboring atoms. The decrease in the linear peak area and increase in the bridge and three-fold peak areas when comparing $AgPd_{1.9}/TiO_2$ to monometallic Pd/TiO_2 indicate a change in Pd structure when alloyed with Ag. In the bimetallic catalysts, less Pd is present in contiguous ensembles and more Pd is isolated from other Pd atoms. These trends agree with those reported by Han et al. for AgPd/ZrO_2 catalysts[16] and these isolated Pd structures are hypothesized to be selective to ethylene in the hydrodechlorination of 1,2-dichloroethane.

Additionally, a shift in the peak corresponding to bridge bound CO is observed from 1982 cm^{-1} on monometallic Pd to 1975 cm^{-1} on bimetallic $AgPd_{1.9}/TiO_2$. This shift indicates an electronic interaction between the Ag and Pd in the bimetallic system where both species gain *d* electron charge and lose non-*d* charge. Because of the higher electronegativity of Pd, however, the charge loss in Ag is only partially compensated by *d*-charge gain and overall charge is transferred from Ag to Pd. When the metal adsorbing the CO receives electrons, increased π back-donation shifts the CO vibrational frequency to lower wavenumbers.[38] This peak shift caused by electron transfer between the two metals suggests close proximity of the Ag and Pd species and intimate bimetallic structure formation.[39] Similarly, a red shift in the linearly adsorbed CO peak is observed as the Pd content decreases. A shift from 2052 cm^{-1} on Pd/TiO_2 and $AgPd_{1.9}/TiO_2$ to 2048 cm^{-1} on $AgPd_{0.35}/TiO_2$ is observed.

FTIR spectra for the SiO_2 supported catalysts are shown in Figure 4.3b. A peak at 2075 cm^{-1}, corresponding to CO linearly adsorbed on Pd, and a broad peak at 1930 cm^{-1}, corresponding to CO adsorbed on bridge and multifold Pd sites, are observed on the bimetallic catalyst with a Pd/Ag ratio of 1.3.[34,35] Although the area of the linear peak increases from the Pd/SiO_2 catalyst to the $AgPd_{1.3}/SiO_2$ catalyst, a large multifold peak is still present for the bimetallic catalyst. This result suggests that by adding Pd to Ag on a SiO_2 support, some isolated Pd sites are formed, but contiguous sites remain.

The above FTIR evidence shows that the fraction of CO adsorbed in a linear configuration changes between catalyst supports. The fraction of the total FTIR peak area that corresponds to linearly adsorbed CO, indicating isolated Pd species, is shown as a function of the Pd mol fraction in Figure 4.4. Across a range of Pd compositions, the TiO_2 supported AgPd catalysts have a larger fraction of CO linearly adsorbed than the SiO_2 supported AgPd catalysts. Additionally, both SiO_2 and TiO_2 supported AgPd catalysts have more linearly adsorbed CO than the monometallic Pd catalysts. We note that we use the peak area without taking into account the extinction coefficients for the different adsorption geometries. Although the extinction coefficients for CO adsorbed on Pd vary with support, the bridge bonded CO has a higher extinction coefficient than linearly bonded CO, and therefore we expect the fraction of Pd sites with linearly bonded CO to be even larger than that estimated using peak areas.[40]

Based on the UV vis results discussed above, the deposition of Pd onto Ag/SiO_2 is not expected to be selective. If we consider linearly adsorbed CO on Pd to be indicative of selective Pd deposition and formation of intimate bimetallic structures, then these FTIR results indicate that bimetallic formation is more effective on the TiO_2 support than on the SiO_2 support. Furthermore, for both TiO_2 and SiO_2 supported catalysts, there is an increase in the number of isolated Pd sites on the bimetallic catalysts compared to monometallic catalysts. We note that carbon supported catalysts do not allow transmittance and therefore transmission FTIR spectra cannot be collected on those samples.

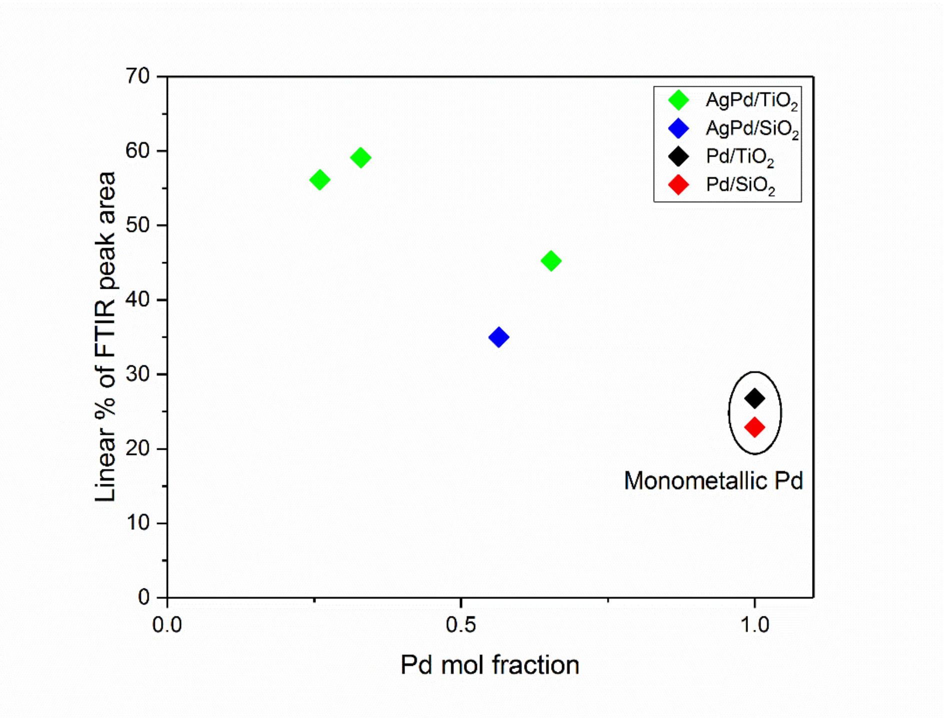

Figure 4.4. The percentage of peak area of CO linearly adsorbed on Pd sites on monometallic Pd and bimetallic AgPd catalysts as a function of the mol fraction of Pd in the catalyst.

We also note that the peak for linearly adsorbed CO on the bimetallic catalysts shifts from 2075 cm^{-1} on the SiO_2 support to 2053 cm^{-1} on the TiO_2 support. This shift may suggest that the Pd sites on the TiO_2 supported bimetallic catalyst are more electronegative than the Pd sites on the SiO_2 supported catalyst. Increased *d*-electron density, which may be due to charge transfer from either the Ag or the TiO_2 to the Pd, leads to a weakened C-O bond and the resulting red shift to lower wavenumbers.[38]

EXAFS analyses were carried out on the Ag, AgPd, and Pd catalysts after *in situ* reduction at 473 K and the resulting fits are shown in Table 4.5. Spectra were collected from both the Pd-K edge and the Ag-K edge, however we note that the close proximity of these edge energies limits the data fitting. The close edge energies results in similar scattering for Ag and Pd, and therefore the Ag-Ag and Ag-Pd scattering cannot be distinguished from one another. As a result, we report Ag-M and Pd-M scatter paths which include both neighboring Ag and Pd atoms. The radius of the nearest neighbor then provides information about the bimetallic nanoparticle composition; in bulk Ag, R_{Ag-Ag} = 2.89 Å and in bulk Pd, R_{Pd-Pd} = 2.75 Å. R values in between these limits indicate a mixture of Pd and Ag.[41–43] We note that the formation of hydride species can complicate this analysis, however the low H_2 concentrations used for the reduction of samples prior to XAS analysis are expected to avoid the formation of hydride species.[44] For the TiO_2 supported AgPd catalysts, we observe a decrease in R as the Pd content is increased; this result is consistent with the smaller R for bulk Pd. Shown in Figure 4.5, we also note that the $AgPd_{0.5}/TiO_2$ and $AgPd_{0.35}/TiO_2$ bimetallic catalysts have similar R values resulting from the EXAFS fits at the Ag edge and the Pd edge. This behavior indicates that the Ag and Pd are well mixed in the bimetallic nanoparticle structure. However, the R values at the Ag and Pd edges deviate somewhat for the $AgPd_{1.9}/TiO_2$ and $AgPd_{1.3}/SiO_2$ catalysts, indicating that the Ag and Pd are segregated to some extent. For the bimetallic carbon supported catalyst however, there is a larger discrepancy of 0.09 Å between the R values obtained from the Pd – M and Ag – M scatter paths at the respective edges. This difference indicates that the local structures around Pd atoms and around Ag atoms differ – Pd is found in areas with high Pd content, indicated by the R of 2.76 Å. The value of R calculated from the Ag-M scatter path from the Ag edge for carbon is 2.85 Å which is more representative of bulk Ag. Thus, the EXAFS fits from the Ag and Pd edges indicate that Ag and Pd are well mixed in the low Pd loading TiO_2-supported catalysts but are more segregated in the SiO_2–supported and particularly the carbon-supported catalysts. Additionally, the intensities of the white line in the XANES spectra are in agreement with peak shifts observed in the FTIR spectra. The Fourier transforms of the EXAFS spectra and the XANES spectra are given in the Appendix Figures B.5-B.8.

Table 4.5. EXAFS fits for Pd, AgPd, and Ag catalysts pretreated under H_2 at 473 K at the Pd-K edge (24350 eV) and Ag-K edge (25514 eV)

Catalyst	**Edge**	**Scatter Path**	**CN**[a]	**R**[b] **(Å)**	ΔE_0 (eV)	σ^2 (Å^2)	**R factor**
Pd/TiO_2	Pd	Pd – M	8.3	2.74	3.79	0.0059	0.031
$AgPd_{1.9}/TiO_2$	Pd	Pd – M	10.1	2.79	1.89	0.0095	0.017
	Ag	Ag – M	10.5	2.83	3.10	0.0095	0.007
$AgPd_{0.5}/TiO_2$	Pd	Pd – M	11.1	2.82	2.96	0.0095	0.011
	Ag	Ag – M	9.1	2.84	2.35	0.0095	0.021
$AgPd_{0.35}/TiO_2$[c]	Pd	Pd – M	9.9	2.84	4.99	0.0095	0.046
	Ag	Ag – M	9.4	2.85	1.87	0.0095	0.021
Ag/TiO_2	Ag	Ag – M	9.6	2.86	2.03	0.0095	0.021
Pd/HTT-C	Pd	Pd – M	10.9	2.74	2.97	0.0059	0.004
$AgPd_{0.6}$/HTT-C	Pd	Pd – M	10.6	2.76	4.36	0.0095	0.008
	Ag	Ag – M	10.0	2.85	2.72	0.0095	0.009
Ag/HTT-C	Ag	Ag – M	9.4	2.87	1.19	0.0095	0.010
Pd/SiO_2	Pd	Pd – M	9.4	2.74	2.98	0.0059	0.009
$AgPd_{1.3}/SiO_2$	Pd	Pd – M	6.0	2.73	-5.58	0.0095	0.017
	Ag	Ag – M	4.5	2.77	0.41	0.0095	0.046
Ag/SiO_2	Ag	Ag – M	3.4	2.79	-1.24	0.0095	0.079

[a] Coordination number, estimated uncertainty ± 20%

[b] Distance between the absorber and back-scatterer, estimated uncertainty ± 0.02 Å

[c] Spectra for $AgPd_{0.35}/TiO_2$ were collected without pretreatment under inert flow

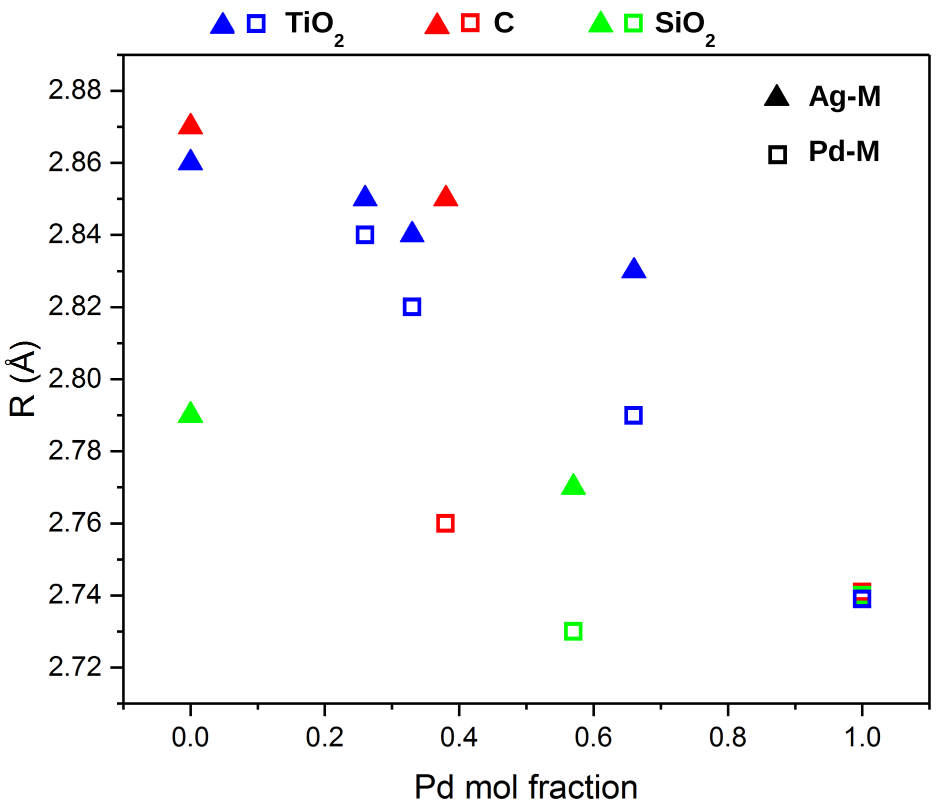

Figure 4.5. Radius of nearest neighbor, R, in Å for the Ag, AgPd, and Pd catalysts on TiO2 (blue), carbon (red), and SiO2 (green) supports as a function of the Pd mol fraction. The R values from the EXAFS fits from the Ag edge, indicating the Ag-M distance, are shown by ▲ and from the Pd edge, indicating the Pd-M distance, are shown by ☐.

The results from UV vis, chemisorption, EXAFS, and CO-FTIR indicate that the Pd structure and extent of bimetallic formation varies on the supports used in this work. At low Pd loadings, TiO_2 supported AgPd catalysts are expected to have minimal extent of monometallic Pd species and close interaction between Ag and Pd.

4.2.3 Catalyst Reactivity Measurements

As shown in Figure 4.6, the hydrodechlorination of 1,2-dichloroethane over the $AgPd_{0.35}/TiO_2$ catalyst achieves 97% selectivity to ethylene. As the Pd loading is increased, 89% selectivity to ethylene is achieved over the $AgPd_{0.5}/TiO_2$ catalyst. The $AgPd_{1.9}/TiO_2$ catalyst, however, exhibits only 1% selectivity to ethylene and 98% selectivity to ethane. Similarly, monometallic Pd/TiO_2 gives 2.5% selectivity to ethylene, 66% selectivity to ethane, and the remainder chloroethane. The selectivity and corresponding conversion values are given in Appendix Table B.1. These changes in selectivity on the TiO_2 supported catalysts can be attributed to changes in the Pd structure. As seen in the FTIR spectra discussed above, $AgPd_{0.35}$ and $AgPd_{0.5}$ showed primarily isolated surface Pd species, while $AgPd_{1.9}$ and Pd/TiO_2 have multifold Pd sites. Thus, we suggest that contiguous Pd species favor the hydrogenation of ethylene to ethane, while the desorption of ethylene is favored on isolated Pd species. Work by others supports this structure sensitivity where aggregated Pd leads to the formation of ethane.[15,45] Additionally, the weak adsorption of CO observed from chemisorption on the $AgPd_{0.35}/TiO_2$ catalyst suggests that ethylene may also be bound more weakly to the Pd species on this catalyst, leading to the observed desorption and resulting high ethylene selectivity. In addition to the effect of Pd geometry on selectivity, the TiO_2 support may also influence the selectivity and favor ethylene production. There have been reports on monometallic Pd/TiO_2 catalysts suggesting that electron transfer from Pd to TiO_2 can occur, resulting in $Pd^{\delta+}$ species and weakening the adsorption of chlorine and ethylene.[46,47] This weakened adsorption then favors the desorption of ethylene as a product, increasing the ethylene selectivity. We note that although this electron transfer may contribute to the selectivity trends to some extent, the high ethane selectivity over the $AgPd_{1.9}/TiO_2$ catalyst suggests that geometric effects dominate on the bimetallic catalysts. The TiO_2 is not expected to contribute to the activity alone, as Ag/TiO_2 catalysts have been reported to be inactive for hydrodechlorination reactions.[13]

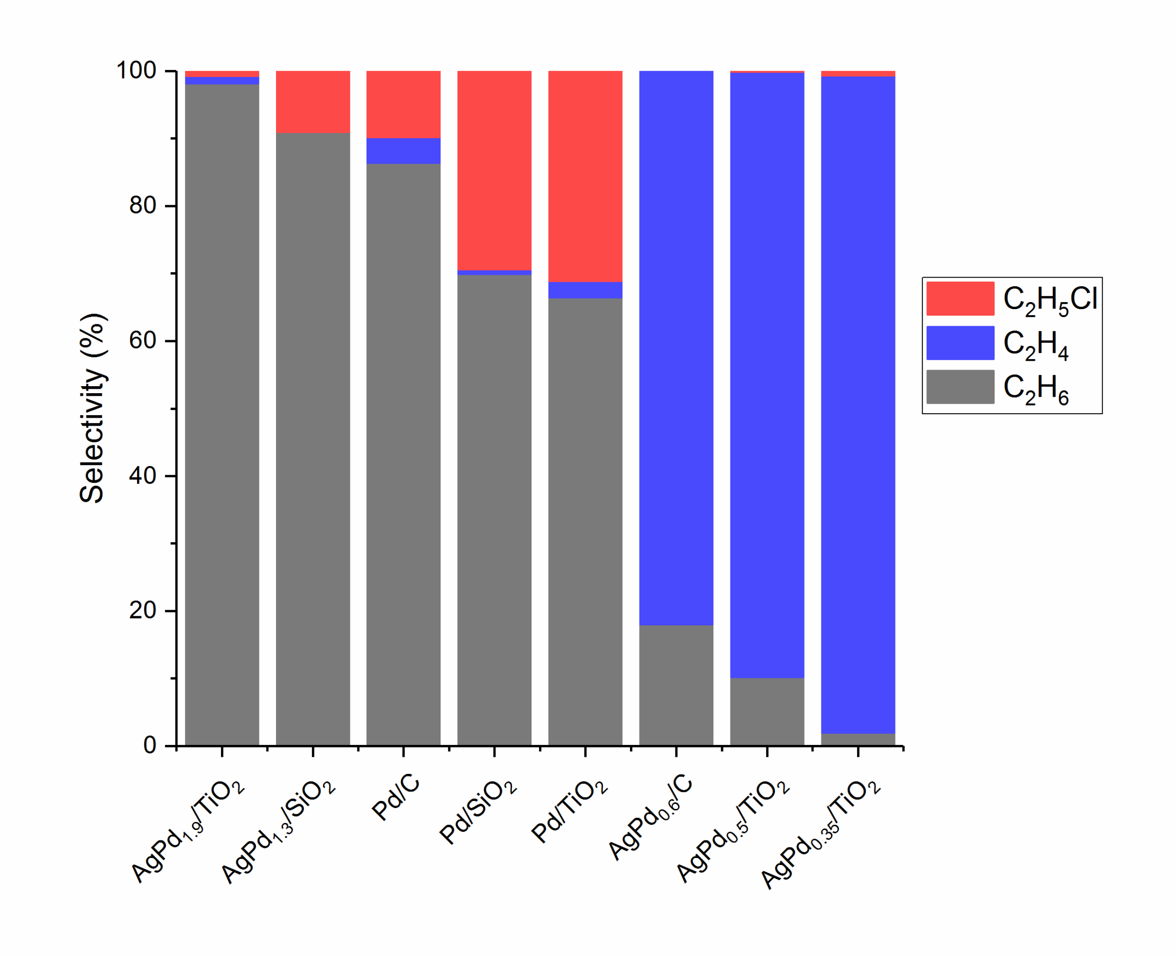

Figure 4.6. Selectivity for monometallic Pd and bimetallic AgPd catalysts for hydrodechlorination of 1,2-dichloroethane at 443 K. Conditions: 443 K, 15 psig, 0.2 Bar H_2, 0.18 Bar 1,2-DCA, total flow rate 36 sccm. All selectivity measurements were carried out at a 1,2-DCA conversion of <2%, a H_2 conversion of <10%, and are averaged over 4 hours time on stream. Selectivity was calculated as the moles of product formed over the total moles of all products, corrected by the stoichiometric numbers.

From FTIR spectra of CO adsorbed on the Pd/SiO_2 and $AgPd_{1.3}/SiO_2$ catalysts, we determined that contiguous Pd sites are available. Accordingly, both monometallic Pd and bimetallic AgPd SiO_2-supported catalysts have low ethylene selectivity and form primarily ethane and some chloroethane. Additionally, the $AgPd_{0.6}/C$ catalyst, which is expected to have some selective deposition of Pd onto Ag and some monometallic Pd species based on UV vis results discussed above, has an ethylene selectivity of 82% and an ethane selectivity of 18%. Thus, the greater is the interaction between the support and Cp(Pd)allyl, the less effective is the formation of bimetallic structures and the larger is the ethane selectivity. The catalysts with more initial intimate bimetallic particle formation, with close interaction between Ag and Pd species, have more isolated Pd species which favors ethylene formation. This behavior is supported by the findings of Han et al., who concluded that the aggregation of Pd species aids in hydrogenation.[15] Work by Nutt et al. on the hydrodechlorination of trichloroethene in water over AuPd catalysts similarly found that at Pd loadings which resulted in more than one monolayer coverage of Pd on Au, primarily ethane was formed. When catalysts contained less than one monolayer of Pd, however, the ethylene selectivity was greater, indicating that Pd species diluted in Au were selective to ethylene.[8] The EXAFS results, which suggest intimate bimetallic formation on the TiO_2 support and segregation of the Ag and Pd on the C and SiO_2 supports, also support this selectivity trend. The size of the accessible Pd species is hypothesized to modulate the binding strength of ethylene which in turn influences whether desorption or hydrogenation is favored. As a result, the ethylene selectivity is influenced by the size of the Pd species in the AgPd nanoparticles.

Theoretical calculations have suggested that the high ethylene selectivity is due to the relative barriers of ethylene desorption and hydrogenation.[45] Xu et al. reported that isolated Pt and Pd species, modeled on $(Pd\text{ or }Pt)_1(Cu, Au,\text{ or }Ag)_3$ (111) surfaces, bind ethylene in a π-bonded configuration. This configuration is less stable than the di-σ configuration which is preferred when neighboring Pd or Pt atoms are accessible. The weakened ethylene binding energy then favors the desorption of ethylene as a product instead of hydrogenation to form ethane. As a result of this change in ethylene adsorption structure from di-σ-bonding to the less stable π-bonding when only isolated Pd species are accessible, the ethylene selectivity increases when the fraction of the Group IB metal is increased. This behavior is observed for Pd_3Ag_1, Pd_1Ag_1 and Pd_1Ag_3 surfaces, where the calculated Gibbs free energy barriers for ethylene desorption are 0.77, 0.40, and 0.02 eV, respectively. The Pd_1Ag_3 surface, which has Pd atoms isolated from one another, is representative of the $AgPd_{0.35}/TiO_2$ catalyst. Thus, the increase in ethylene selectivity we observe on AgPd catalysts with isolated Pd moieties results from weakened ethylene adsorption and decreased desorption energy barriers. A similar explanation has been previously reported for PtCu catalysts.[6,48]

The electronegativity of Pd sites may also influence the ethylene selectivity. As noted from the redshift in the peak for linearly adsorbed CO in the FTIR spectra from the SiO_2-supported to the TiO_2-supported bimetallic catalysts, the Pd sites on the TiO_2 support are more electronegative than the Pd sites on the SiO_2 support. As a result, we suggest that the increased electronegativity may also explain the increased ethylene selectivity. We note that this electronic structure change and the geometric change discussed above both result in weakened adsorption of intermediates which favors the formation of ethylene rather than overhydrogenation to ethane.

In addition to the change from primarily ethane selectivity to primarily ethylene selectivity as the degree of bimetallic formation improves, we note a change in the chloroethane selectivity. Over the monometallic Pd catalysts on carbon, SiO_2, and TiO_2 supports, between 10% and 31% selectivity to chloroethane is observed. The $AgPd_{1.3}/SiO_2$ catalyst also gives around 9% selectivity to chloroethane. In contrast, the remaining bimetallic catalysts are less than 1% selective to chloroethane. Therefore, we suggest that the decrease in chloroethane selectivity over the bimetallic catalysts is based on the role of Ag in hydrodechlorination.

Work by Heinrichs et al. suggested that both Ag and Pd sites play a role in hydrodechlorination of 1,2-dichloroethane.[17,18] They suggested that dissociative adsorption of 1,2-dichloroethane occurs on Ag sites and hydrogen dissociation occurs on Pd sites. The adsorbed Cl on Ag sites induces a slight positive charge, thus making ethylene adsorption on $Ag^{\delta+}$ feasible. Other work has suggested $Ag^{\delta+}$ species form because of electronic interactions with the more electronegative Pd.[16] Thus, C-Cl bond cleavage is more favorable on Ag sites and can justify the absence of chloroethane over the TiO_2 and carbon supported bimetallic AgPd catalysts. Although the Ag sites are active in the bimetallic catalysts, it is important to note that monometallic Ag catalysts have been reported to be inactive for hydrodechlorination of 1,2-

dichloroethane.[1,15] The hydrogen dissociation required for hydrodechlorination is highly activated on Ag surfaces.[2] Furthermore, adsorbed Cl species bind strongly to Ag[49] and therefore may lead to rapid deactivation of Ag catalysts. In AgPd bimetallic catalysts, however, adsorbed H on Pd sites can be transferred to Ag sites and remove Cl as HCl, thus maintaining catalyst activity.[18] As a result, the Pd acts to maintain the Ag activity in bimetallic catalysts for hydrodechlorination of 1,2-dichloroethane and thus ethylene or ethane will be formed preferentially over chloroethane on catalysts with bimetallic structures. Based on the characterization results discussed above, the $AgPd_{1.3}/SiO_2$ catalyst has monometallic Ag and Pd species. Therefore, we suggest the formation of chloroethane over this catalyst is due to the C-Cl bond cleavage on Ag sites that is not followed by Cl removal as HCl since Pd is not in intimate contact with the Ag. Additionally, we expect the formation of chloroethane to occur on the monometallic Pd catalysts, since it has previously been shown that the rate of 1,2-dichloroethane hydrodechlorination is slower on Pd than on Ag.[50] Since C-Cl bond cleavage is the reported rate determining step,[10] it follows that a lower overall rate implies a lower rate of C-Cl bond cleavage and therefore the formation of chloroethane as a product is favored over subsequent cleavage of the second C-Cl bond.

The rates and turnover frequencies of 1,2-dichloroethane conversion over the TiO_2, carbon, and SiO_2 supported catalysts are shown in Table 4.6 and Appendix Table B.2. The rates are reported as the average over four hours time on stream at 443 K and were collected after an initial deactivation period of several hours after which the TOF measured across 48 hours time on stream remained constant within 10%.

For the TiO_2-supported catalysts, the turnover frequency, based on Pd sites measured by CO uptake, increases from the monometallic Pd catalyst to the bimetallic AgPd catalysts. The turnover frequency (TOF) increases as the Pd/Ag ratio decreases, with a factor of 17 increase in the TOF over $AgPd_{0.35}/TiO_2$ compared to Pd/TiO_2. This trend indicates that the isolated Pd species present on the low Pd loading catalysts have higher intrinsic activity than the larger Pd ensembles present on the monometallic Pd and higher Pd loading bimetallic catalysts. This result is supported by the chemisorption results on the $AgPd_{0.35}/TiO_2$ catalyst that show a high amount of reversible CO uptake indicating a weakened binding of species compared to catalysts with higher Pd loadings. The weakened binding of reactive intermediates on this catalyst then results in an increased rate of 1,2-dichloroethane conversion. This increased activity is correlated with the increased ethylene selectivity with decreasing Pd loading.

Table 4.6. Turnover frequency, rate of 1,2-dichloroethane conversion, and ethylene selectivity for Pd and AgPd catalysts. The TOFs are calculated using Pd sites determined by CO chemisorption, using a stoichiometry of 1 CO:1 Pd. The rate is reported as the rate of 1,2-DCA reacted per mol of total Pd or total metal as determined by ICP. Conditions: 443 K, 15 psig, 0.2 Bar H_2, 0.18 Bar 1,2-DCA, total flow rate 36 sccm

	TOF (ks^{-1})	**Rate ($\mu mol\ mol_{Pd}^{-1}\ s^{-1}$)**	**Rate ($\mu mol\ mol_{metal}^{-1}\ s^{-1}$)**	**C_2H_4 Selectivity (%)**
Pd/TiO_2	15.9	1710	1710	2.47
$AgPd_{1.9}/TiO_2$	17.8	2190	1430	1.06
$AgPd_{0.5}/TiO_2$	35.0	6050	1990	89.6
$AgPd_{0.35}/TiO_2$	276	3010	782	97.3
Pd/C	19.0	618	618	3.81
$AgPd_{0.6}/C$	19.4	1790	688	82.0
Pd/SiO_2	20.9	1380	1380	0.70
$AgPd_{1.3}/SiO_2$	14.0	3810	2150	0.02

On the SiO_2 support, a small decrease in turnover frequency is observed for the AgPd catalyst, compared to the monometallic Pd catalyst. However, a 2.8- and 1.6-fold increase is observed in the rate normalized by total moles of Pd and total moles of metal, respectively, for the AgPd catalyst compared to the Pd/SiO_2 catalyst (Table 4.6). For these catalysts, the bimetallic catalyst has a higher ethane selectivity than the monometallic Pd catalyst, at the expense of chloroethane (Figure 4.6). We also note the turnover frequency on the SiO_2–supported catalysts is approximately the same as the ethane selective TiO_2 supported catalysts.

The Pd and AgPd high temperature treated carbon supported catalysts have similar turnover frequencies even though the ethylene selectivity differs by almost 80%. We observe that as the ethylene selectivity increases past the value of 82% obtained over $AgPd_{0.6}/C$, the TOF then begins to increase. This trend, observing increasing TOF as ethylene selectivity increases, may be attributed to the behavior that upon desorption of ethylene, surface sites become accessible for adsorption of 1,2-dichloroethane. This behavior agrees with the reaction orders determined in reaction kinetics studies by Heinrichs et al. They determined that hydrodechlorination of 1,2-dichloroethane over AgPd catalysts is first order in DCA and negative order in ethylene.[10] As ethylene desorbs and decreases its coverage, the rate increases while increasing the coverage of DCA increases the rate of conversion.

The rate normalized by the total moles of Pd in the catalyst (Table 4.6) is higher for the bimetallic catalysts compared to monometallic catalysts. For the TiO_2 supported samples, we note that in contrast to the TOF trends, the rate per mol of Pd does not continuously increase as the Pd loading decreases, since the dispersion of Pd decreases as the loading decreases and thus less Pd species are accessible at the catalyst surface. Because this normalization assumes that the Ag metal is inactive, the increased activity for bimetallic catalysts may be attributed to the activity of Ag sites when alloyed with Pd, as discussed above. Work by Heinrichs et al. has suggested that the rate determining step, the dissociative adsorption of 1,2-dichloroethane, likely occurs on Ag sites. We note that the active site for this reaction may also be at the interface of Pd and Ag such that reactive intermediates can be exchanged between Pd and Ag sites.

The rate per mole of total metal is also calculated to account for both metals taking part in the surface chemistry. Using this normalization for the TiO_2 supported catalysts, the highest rate is observed over the $AgPd_{0.5}/TiO_2$ catalyst, while the lowest rate is observed over the $AgPd_{0.35}/TiO_2$ catalyst. This result supports the hypothesis that the isolated Pd surface structure is responsible for increased ethylene selectivity and 1,2-DCA conversion activity. The $AgPd_{0.35}/TiO_2$ has the lowest fraction of surface metal being Pd sites and thus the rate based on total surface metal will be lower if the Pd sites are the primary sites leading to formation of ethylene.

4.3 Conclusions

We have demonstrated the synthesis of AgPd catalysts supported on TiO_2, SiO_2, and carbon using controlled surface reactions. We determined that TiO_2 is an effective support for the deposition of Pd onto Ag nanoparticles to form effective bimetallic structures. Chemisorption and CO FTIR experiments showed that the Pd surface structure changed across supports and across Pd loadings. AgPd catalysts on TiO_2 at low Pd loadings have Pd primarily present in isolated moieties, diluted from other Pd species by Ag. AgPd catalysts based on SiO_2 and C supports, however, have Pd present in both isolated and contiguous species.

For the gas phase hydrodechlorination of 1,2-dichloroethane, AgPd/TiO_2 catalysts with isolated Pd species were found to be up to 97% selective to ethylene, while the AgPd/SiO_2 catalyst was found to have an ethane selectivity of 91%. Thus, a high ethylene selectivity is correlated with the presence of isolated Pd species surrounded by Ag in the bimetallic catalysts. Additionally, the catalysts with high ethylene selectivity exhibited an increase in the TOF of 1,2-dichloroethane conversion over the catalysts with high ethane selectivity. Thus, isolated Pd species which are selective to ethylene are also more active than the contiguous Pd species which are selective to ethane. On monometallic Pd catalysts, up to 31% selectivity to chloroethane was observed, and the formation of AgPd species reduced this selectivity to less than 10% for all bimetallic catalysts. The formation of AgPd bimetallic sites enhanced the activity of both Ag and Pd species to facilitate C-Cl bond breaking and desorption of the resulting ethylene. Accordingly, for hydrodechlorination of 1,2-dichloroethane, the most ethylene selective structures are formed on TiO_2 and the most ethane selective structures are formed on SiO_2.

4.4 Materials and Methods

4.4.1 Catalyst Synthesis

Parent Ag/SiO_2 and Ag/TiO_2 catalysts were synthesized using deposition precipitation, and the parent Ag/C catalyst was synthesized using wet impregnation as described in Sections 2.1.3 and 2.1.2. Monometallic Pd catalysts on all supports were synthesized by incipient wetness impregnation, as described in Section 2.1.2. The bimetallic AgPd catalysts were synthesized by controlled surface reactions, described in Section 2.1.4.

4.4.2 Characterization

Adsorption measurements

Surface Ag sites were measured using N_2O titration, following the methods of Seyedmonir et al.[51] and surface Pd sites were measured using CO chemisorption. Prior to CO adsorption, the catalyst samples were reduced at 473 K in H_2 for 6 h (heating rate 0.75 K/min). Experimental details are provided in Sections 2.2.1 and 2.2.2.

Fourier transform infrared spectroscopy

Fourier transform infrared spectroscopy of adsorbed CO on the catalyst samples was carried out using a Nicolet 6700 spectrometer. Catalyst samples were pressed into self-supporting pellets (approximately 20 mg) and loaded into a sample cell described elsewhere.[52] The sample was reduced in H_2 for 6h at 473 K (heating rate 0.75 K/min) and then evacuated to 10^{-5} Torr. A background spectrum was collected and 1% CO (Airgas) was then introduced to the cell. Spectra were collected by averaging 256 scans with a resolution of 4 cm^{-1}. After the catalyst surface was saturated with CO, the cell was evacuated to remove weakly adsorbed CO. Spectra were normalized by the pellet area density (pellet area/pellet mass) and Pd site density.

X-ray absorption spectroscopy

X-ray absorption spectroscopy was carried out at MRCAT facilities (10-BM/ID) at the Advanced Photon Source at Argonne National Laboratory. Measurements were taken at the Pd-K edge (24350 eV) and the Ag-K edge (25514 eV). Catalyst samples were pressed into pellets supported inside a stainless-steel sample holder. The sample holder was placed inside a quartz tube with Kapton windows on either side and fittings to allow for gas flow through the tube. Samples were treated in 3% H_2 in He (Airgas) for 30 min at 473 K, purged with He, and then cooled to room temperature under inert flow for analysis. For each sample, the energy was calibrated by collecting spectra of Pd and Ag foils. The Demeter software package was used to fit spectra over an R range of 1.6 – 3.2 Å and a k-range of 2.8 – 13.5 $Å^{-1}$. The amplitude reduction factor was calculated by fitting spectra of the reference foils and determined to be $S_0^2 = 0.88$ for Ag and $S_0^2 = 0.86$ for Pd.

4.4.3 Reaction Kinetics Measurements

Catalysts were pressed and sieved to 20/40 mesh and diluted twice by weight with similarly sized alpha alumina (Alamatis T64) then loaded into a 6.35 mm ID x 305 mm, 316 stainless steel reactor for activity testing. A cylindrical aluminum block, with imbedded cartridge heaters (Tempco, ¼”X 10”, 250W), was clamped, with minimal air gap, around the middle 203 mm of this reactor and served as the heating source for the reactor. A K-type thermocouple was placed inside a well bored into the aluminum block and used for temperature control of the cartridge heaters in a PID loop, giving a uniform temperature profile over the middle 152 mm of the alumina block. The catalyst and diluent were loaded in this 152 mm section. He, N_2, and H_2 (Research Grade, Airgas), delivered by mass flow controller (Brooks 5890E), and liquid dichloroethane (99%, Aldrich), delivered via syringe pump (ISCO), were used for reactor testing without further purification. The molar ratio of H_2:dichloroethane was 1:1 for all reactions. To compare catalysts, the catalyst mass was adjusted to maintain a constant residence time. The N_2 was fed to the reactor and used as an internal standard to correct for volume changes due to stoichiometric changes in the numbers of moles, however at the low conversions of these tests this dilution effect was minimal. Reactant and product analysis was performed by Siemens Maxum GC with argon carrier gas using a TCD detector for analysis of N_2, H_2, ethane, ethylene, and methane while an FID detector was used to monitor dichloroethane and ethyl chloride. No methane or ethyl chloride were detected at any conditions for the catalysts studied in this work. All measurements were carried out at a 1,2-DCA conversion of less than 2% and rate and selectivity values represent averages over 4 hours time on stream, during which time the rate remained constant within 10%. H_2 conversion was typically kept below 10% based on H_2, and the absence of heat and external mass transfer effects were assumed after verifying effectiveness factor and Mears' axial dispersion and radial interparticle temperature correlations using GradientCheck.[53] Details on these calculations are given in Appendix B. For all reactions, the carbon balance was closed to >97%. No conversion was observed for a blank reaction with diluent only.

4.5 Acknowledgements

This work was supported as part of The Dow Chemical Company University Partner Initiative with UW-Madison, under Dow agreement number 235744C. We thank Christopher M. Menzies, Dow, for his assistance with reactor testing. MRCAT operations are supported by the Department of Energy and the MRCAT member institutions. This research used resources of the Advanced Photon Source, a U.S. Department of Energy (DOE) Office of Science User Facility operated for the DOE Office of Science by Argonne National Laboratory under Contract No. DE-AC02-06CH11357. The use of facilities supported by the Wisconsin Materials Research Science and Engineering Center is also acknowledged (DMR-1121288). The authors thank Jeff Miller for useful discussions regarding XAS results and data analysis as well as Joe Chada and Siddarth Krishna for their help in obtaining XAS data.

4.6 References

(1) Heinrichs, B.; Delhez, P.; Schoebrechts, J. P.; Pirard, J. P. *J. Catal.* **1997**, *172*, 322–335.

(2) Xu, L.; Stangland, E. E.; Mavrikakis, M. *Catal. Sci. Technol.* **2018**, *8*, 1555–1563.

(3) Lambert, S.; Ferauche, F.; Brasseur, A.; Pirard, J. P.; Heinrichs, B. *Catal. Today* **2005**, *100*, 283–289.

(4) Hoke, J. B.; Gramiccioni, G. A.; Balko, E. N. *Appl. Catal. B, Environ.* **1992**, *1*, 285–296.

(5) Legawiec-Jarzyna, M.; Śrębowata, A.; Juszczyk, W.; Karpiński, Z. *Appl. Catal. A Gen.* **2004**, *271*, 61–68.

(6) Kovalchuk, V. I.; D'Itri, J. L. *Appl. Catal. A Gen.* **2004**, *271*, 13–25.

(7) Meyer, R. J.; Kim, D. I.; Allen, D. T.; Jo, J. H. *Chem. Eng. Sci.* **1999**, *54*, 3627–3634.

(8) Nutt, M. O.; Hughes, J. B.; Wong, M. S. *Environ. Sci. Technol.* **2005**, *39*, 1346–1353.

(9) Halász, J.; Imre, B.; Hannus, I. *Appl. Catal. A Gen.* **2004**, *271*, 47–53.

(10) Heinrichs, B.; Schoebrechts, J. P.; Pirard, J. P. *J. Catal.* **2001**, *200*, 309–320.

(11) Heinrichs, B.; Noville, F.; Schoebrechts, J. P.; Pirard, J. P. *J. Catal.* **2003**, *220*, 215–225.

(12) Borovkov, V. Y.; Luebke, D. R.; Kovalchuk, V. I.; d'Itri, J. L. *J. Phys. Chem. B* **2003**, *107*, 5568–5574.

(13) Han, Y.; Zhou, J.; Wang, W.; Wan, H.; Xu, Z.; Zheng, S.; Zhu, D. *Appl. Catal. B Environ.* **2012**, *125*, 172–179.

(14) Ito, L. N.; Harley, A. D.; Holbrook, M. T.; Smith, D. D.; Murchison, C. B.; Cisneros, M. D. Processes for converting chlorinated alkane byproducts or waste products to useful, less chlorinated alkenes. EP 0662941 B1, 1997.

(15) Han, Y.; Gu, G.; Sun, J.; Wang, W.; Wan, H.; Xu, Z.; Zheng, S. *Appl. Surf. Sci.* **2015**, *355*, 183–190.

(16) Han, Y.; Sun, J.; Fu, H.; Qu, X.; Wan, H.; Xu, Z.; Zheng, S. *Appl. Catal. A Gen.* **2016**, *519*, 1–6.

(17) Heinrichs, B.; Schoebrechts, J.-P.; Pirard, J.-P. *Stud. Surf. Sci. Catal.* **2000**, *130*, 2015–2020.

(18) Heinrichs, B.; Noville, F.; Schoebrechts, J.-P.; Pirard, J.-P. *J. Catal.* **2000**, *192*, 108–118.

(19) Luebke, D. R.; Vadlamannati, L. S.; Kovalchuk, V. I.; D'Itri, J. L. *Appl. Catal. B Environ.* **2002**, *35*, 211–217.

(20) Vadlamannati, L. S.; Luebke, D. R.; Kovalchuk, V. I.; Itri, J. L. *Stud. Surf. Sci. Catal.* **2000**, *130*, 233–238.

(21) Rhodes, W.; Lazar, K.; Kovalchuk, V.; Ditri, J. *J. Catal.* **2002**, *211*, 173–182.

(22) Coq, B.; Figuéras, F.; Hub, S.; Tournigant, D. *J. Phys. Chem.* **1995**, *99*, 11159–11166.

(23) Alba-Rubio, A. C.; Sener, C.; Hakim, S. H.; Gostanian, T. M.; Dumesic, J. A. *ChemCatChem* **2015**, *7*, 3881–3886.

(24) Aragão, I. B.; Ro, I.; Liu, Y.; Ball, M.; Huber, G. W.; Zanchet, D. *Appl. Catal. B Environ.* **2018**, *222*, 1–2.

(25) Liu, Y.; Göeltl, F.; Ro, I.; Ball, M. R.; Sener, C.; Aragão, I. B.; Zanchet, D.; Huber, G. W.; Mavrikakis, M.; Dumesic, J. A. *ACS Catal.* **2017**, *7*, 4550–4563.

(26) Hakim, S. H.; Sener, C.; Alba-Rubio, A. C.; Gostanian, T. M.; O'Neill, B. J.; Ribeiro, F. H.; Miller, J. T.; Dumesic, J. A. *J. Catal.* **2015**, *328*, 75–90.

(27) Ro, I.; Liu, Y.; Ball, M. R.; Jackson, D. H. K.; Chada, J. P.; Sener, C.; Kuech, T. F.; Madon, R. J.; Huber, G. W.; Dumesic, J. A. *ACS Catal.* **2016**, *6*, 7040–7050.

(28) Ro, I.; Aragao, I. B.; Chada, J. P.; Liu, Y.; Rivera-Dones, K. R.; Ball, M. R.; Zanchet, D.; Dumesic, J. A.; Huber, G. W. *J. Catal.* **2018**, *358*, 19–26.

(29) Ro, I.; Sener, C.; Stadelman, T. M.; Ball, M. R.; Venegas, J. M.; Burt, S. P.; Hermans, I.; Dumesic, J. A.; Huber, G. W. *J. Catal.* **2016**.

(30) Sener, C.; Wesley, T. S.; Alba-Rubio, A. C.; Kumbhalkar, M. D.; Hakim, S. H.; Ribeiro, F. H.; Miller, J. T.; Dumesic, J. A. *ACS Catal.* **2016**, *6*, 1334–1344.

(31) Hadjiivanov, K.; Kno, H. *J. Phys. Chem. B* **1998**, *102*, 10936–10940.

(32) Lisowski, W.; Klimczuk, T.; Zaleska-Medynska, A.; Grabowska, E.; Marchelek, M. *J. Mol. Catal. A Chem.* **2016**, *424*, 241–253.

(33) Karakaya, I.; Thompson, W. T. *Bull. Alloy Phase Diagrams* **1988**, *9*, 237–243.

(34) Rebelli, J.; Rodriguez, A. A.; Ma, S.; Williams, C. T.; Monnier, J. R. *Catal. Today* **2011**, *160*, 170–178.

(35) Gao, F.; Goodman, D. W. *Chem. Soc. Rev.* **2012**, *41*, 8009.

(36) Giorgi, J. B.; Schroeder, T.; Bäumer, M.; Freund, H.-J. *Surf. Sci.* **2002**, *498*, L71–L77.

(37) Loffreda, D.; Simon, D.; Sautet, P. *Surf. Sci.* **1999**, *425*, 68–80.

(38) Primet, M.; Mathieu, M. V.; Sachtler, W. M. H. *J. Catal.* **1976**, *44*, 324–327.

(39) Tromp, M.; van Bokhoven, J. A.; van Strijdonck, G. P. F.; van Leeuwen, P. W. N. M.; Koningsberger, D. C.; Ramaker, D. E. *J. Am. Chem. Soc.* **2005**, *127*, 777–789.

(40) Vannice, M. A.; Wang, S. Y. *J. Phys. Chem.* **1981**, *85*, 2543–2546.

(41) Tsapina, A. M.; Tsyrulnikov, P. G.; Glyzdova, D. V.; Shlyapin, D. A.; Vedyagin, A. A.; Kaichev, V. V.; Trenikhin, M. V.; Trigub, A. L.; Lavrenov, A. V. *Appl. Catal. A Gen.* **2018**, *563*, 18–27.

(42) Lin, C.-K.; Lin, Y.-G.; Wu, T.; Barkholtz, H. M.; Lin, Q.; Wei, H.; Brewe, D. L.; Miller, J. T.; Liu, D.; Ren, Y.; Ito, Y.; Xu, T. *Inorg. Chem.* **2012**, *51*, 13281–13288.

(43) Aich, P.; Wei, H.; Basan, B.; Kropf, A. J.; Schweitzer, N. M.; Marshall, C. L.; Miller, J. T.; Meyer, R. *J. Phys. Chem. C* **2015**, *119*, 18140–18148.

(44) Benson, J. E.; Hwang, H. S.; Boudart, M. *J. Catal.* **1973**, *30*, 146–153.

(45) Xu, L.; Stangland, E. E.; Mavrikakis, M. *J. Catal.* **2018**, *362*, 18–24.

(46) Babu, N. S.; Lingaiah, N.; Pasha, N.; Kumar, J. V.; Prasad, P. S. S. *Catal. Today* **2009**, *141*, 120–

124.

(47) González, C. A.; Bartoszek, M.; Martin, A.; De Correa, C. M. *Ind. Eng. Chem. Res.* **2009**, *48*, 2826–2835.

(48) Avdeev, V. I.; Kovalchuk, V. I.; Zhidomirov, G. M.; D’Itri, J. L. *J. Struct. Chem.* **2007**, *48*, 171–183.

(49) Petrova, N. V.; Yakovkin, I. N.; Braun, O. M. *Chem. Phys.* **2011**, *383*, 35–40.

(50) Anju, Y.; Yamamoto, H.; Seiyama, T.; Kato, A.; Mochida, I. The Dehalogenation of Haloalkanes on SiO 2 -supported Metals . *Bulletin of the Chemical Society of Japan*, 2006, *45*, 2319–2323.

(51) Seyedmonir, S. R.; Strohmayer, D. E.; Geoffroy, G. L.; Vannice, M. A.; Young, H. W.; Linowski, J. W. *J. Catal.* **1984**, *87*, 424–436.

(52) Shen, J.; Hill, J. M.; Watwe, R. M.; Spiewak, B. E.; Dumesic, J. A. *J. Phys. Chem. B* **1999**, *103*, 3923–3934.

(53) Gradient✓ (GradientCheck) for Heterogeneous Catalysis, 2016.

Chapter 5. AgPd and CuPd catalysts for selective hydrogenation of acetylene

5.1 Introduction

The selective hydrogenation of acetylene in ethylene-rich streams is used to purify ethylene prior to polymerization reactions.[1] Acetylene levels are usually around 1% in ethylene streams and must be reduced to less than 5 ppm to reduce deactivation of the polymerization catalysts.[2,3] This process can be operated in either a front-end or tail-end process, referring to the placement of the hydrogenation unit either before the de-methanizer unit or after the de-ethanizer unit, respectively.[4] The tail-end process is operated at lower partial pressures of hydrogen and involves feeds that contain less light hydrocarbons compared to the front-end process. This hydrogenation reaction is typically carried out using Ni- or Pd-based catalysts, due to their high activity while achieving selectivity to the desired ethylene.[4,5] Studies have shown that metals such as Cu or Au are also active and selective, while metals such as Pt or Ir give lower selectivities.[4] To identify a desirable catalyst for acetylene hydrogenation in the presence of ethylene, it is important to achieve high activity while also maintaining high selectivity and avoiding over-hydrogenation to ethane.[6] Acetylene hydrogenation proceeds via a Horiuti-Polanyi mechanism where acetylene is first hydrogenated to a vinyl intermediate, which is subsequently hydrogenated to the desired ethylene.[7] Unselective production of ethane can occur via hydrogenation of ethylene directly, or by hydrogenation of the vinyl intermediate to ethylidene followed by hydrogenation to ethane. Studies on acetylene hydrogenation over Pd catalysts over the past decades have been summarized in several review papers.[4,8–10]

Importantly, it has been reported that the selectivity of Pd-based catalysts can be improved by forming bimetallic catalysts with Pd and a group IB metal such as Ag, Au, or Cu, with AgPd catalysts often used in industrial processes.[3,11] It is suggested that by forming these Pd alloys, the d-band center of the Pd is shifted and therefore favors the desorption rather than hydrogenation of ethylene.[12] As a result, extensive research has been carried out on various aspects of acetylene hydrogenation over bimetallic catalysts. Many studies have investigated the role of the Pd site structure on ethylene selectivity. Work by Tsapina et al. used X-ray absorption spectroscopy to study Pd-Ga, Pd-Zn, and Pd-Ag catalysts and found that the distance between neighboring Pd atoms was increased from 2.75 Å to between 2.82-2.99 Å for the bimetallic catalysts.[13] They hypothesized that this dilution of Pd atoms can prevent acetylene from adsorbing in a strong multisite mode and improve ethylene selectivity. Investigation of CuPd/Al_2O_3 catalysts by Leviness et al. determined that the addition of Cu to Pd increased the catalyst stability and ethylene selectivity while decreasing the catalyst activity.[14] This effect was attributed to Cu breaking up Pd-hydride phases and decreasing the contiguous Pd sites which can dissociatively adsorb acetylene and lead to the formation of C_{4+} species.

Computational work has also investigated acetylene hydrogenation to identify the origin of high ethylene selectivity over bimetallic catalysts[7,12,15] and to identify potential new catalytic materials.[16] For PdIn alloy surfaces, the ethylene selectivity was predicted to be higher on surfaces with single atom Pd sites than on surfaces with Pd trimer sites, suggesting that when ethylene is adsorbed more weakly on single atom Pd sites it readily desorbs as a product rather than being further hydrogenated.[15] These calculations were supported by experimental studies over well controlled PdIn single crystal surfaces, showing that over PdIn crystals with single atom Pd sites 92% ethylene selectivity was achieved, while Pd_3In crystals with Pd trimer sites achieved only 21% ethylene selectivity. Other work has developed a descriptor to determine the relative rates of hydrogenation and C-C coupling reactions with the aim of identifying metals that reduce oligomerization reactions.[12] It was determined that over Pt and Ir catalysts, the selectivity to 1,3-butadiene, the presumed precursor to further oligomers, is lowest, and the selectivity increases for Rh, Pd, and Cu, respectively. This desired low selectivity to 1,3-butadiene needs to be balanced, however, with the acetylene hydrogenation activity and selectivity to ethylene. Weak adsorption of acetylene on the catalyst surface will decrease the barriers for both the desired selective hydrogenation of acetylene and the undesired coupling reactions.[12]

Other computational studies have focused on the mechanism of acetylene hydrogenation on both monometallic Pd and alloy catalysts. Work by Mei et al. determined, by DFT and kinetic Monte Carlo simulations, that the selective formation of ethylene proceeds through a surface vinyl species, while the unselective formation of ethane can occur from overhydrogenation of ethylene to ethane directly or hydrogenation of vinyl to form ethylidene.[7] The vinyl intermediate is suggested to be a key intermediate, since, depending on the other surface species, it can be converted into a range of different surface intermediates. Studies of the effects of coverage on Pd surfaces determined that adsorption energies decrease on a covered surface because of repulsive interactions.[17] Additionally, increasing the surface coverage is determined to decrease the barrier for acetylene hydrogenation to the vinyl intermediate, from 66 kJ/mol at 0.25 ML coverage to 50 kJ/mol at 0.33 ML coverage.[7] The presence of Ag on the surface is concluded to improve the catalyst performance by weakening adsorption energies of all intermediates which increases the rates for both desorption and hydrogenation. Furthermore, Ag reduces the presence of large Pd ensembles which are expected to be active for C-C bond breaking.[7] Although catalyst performance is suggested to be highly dependent on the reaction conditions,[10] these first principles calculations provide important insights into the mechanism of acetylene hydrogenation over both Pd and AgPd catalysts.

Acetylene hydrogenation chemistry has also been widely studied in the surface science community, with spectroscopic studies of both adsorption and reactions informing understanding of the catalyst surface. It is important to note that many of these studies have been carried out on single crystal surfaces under UHV conditions, and therefore although they provide invaluable information about surface species, the dependence on pressure and temperature may not be the same as for an industrially relevant catalyst. Work by Gates and Kesmodel investigated the adsorption of acetylene[18–20] and ethylene[19,21] on Pd(111) and Pd(100) surfaces through high resolution electron energy loss spectroscopy. These studies determined that at low temperatures (< 250 K) acetylene chemisorbs on the Pd surface, while upon heating, acetylene is converted to ethylidyne. Ethylene binds more weakly than acetylene to the surface and is also converted to ethylidyne around 300K. Later studies by Tysoe and coworkers identified the formation of a vinylidene surface species formed after adsorption of acetylene on Pd(111) at room temperature and determined that the vinylidene species was stable up to 480 K.[22] Additional studies determined that the rate limiting step of acetylene hydrogenation is the addition of the first hydrogen to form the vinyl intermediate. It was also found that vinyl species can be converted to ethylidyne and that any surface vinylidene species can be hydrogenated to ethylidyne at high hydrogen pressures through a vinyl intermediate.[23] Computational studies have also informed the structure of surface species derived from acetylene and ethylene. Studies of adsorbed vinylidene on Pd(111) predict that acetylene can isomerize to vinylidene with a low barrier and that vinylidene is more stable than the starting acetylene.[24] Other calculations of vibrational spectra of adsorbed acetylene on Cu(111) and Pd(111) determined that the spectra are not sensitive to the particular adsorption site (bridge or hollow) but are sensitive to the metal.[25] These studies indicate that a variety of surface species are present under acetylene hydrogenation conditions. As more direct evidence, recent work by Krooskwyk et al. investigated both surface and gas phase species during acetylene hydrogenation over a Pt(111) surface using polarization-dependent infrared spectroscopy. This work determined that, on a platinum surface, ethylidyne, ethylidene, and di-σ-bonded ethylene are all spectator species during acetylene hydrogenation.[26]

In this work, we have investigated AgPd and CuPd catalysts, synthesized by controlled surface reactions, for the selective hydrogenation of acetylene. By synthesizing catalysts with a measurable distribution of nanoparticle size and composition, we can develop structure-activity relationships for this system. The catalysts were characterized using STEM-EDS, CO chemisorption, and FTIR of adsorbed CO and adsorbed C_2H_4. In-situ FTIR studies of the catalysts under reaction conditions were used to identify surface spectator species. This work aims to bridge the gap between adsorption on ideal surfaces and adsorption under reaction conditions on supported nanoparticle catalysts to understand the controlling factors for achieving high ethylene selectivity on AgPd and CuPd bimetallic catalysts.

5.2 Results and Discussion

5.2.1 Catalyst Synthesis

Ag/TiO_2 and Cu/TiO_2 catalysts were first prepared using deposition precipitation and ion exchange, respectively. The metal loading, determined by ICP, and the site densities, determined by N_2O titration, are shown in Table 5.1. Additionally, the average particle size, determined by STEM, is given for the parent catalysts. We note that although the Ag and Cu catalysts have different metal loadings, the metal particle sizes are similar for these catalysts. The TiO_2 support was chosen since it was found in previous work, detailed in Chapter 4, to facilitate the most effective formation of AgPd bimetallic structures. A Cu/SiO_2 parent catalyst was also synthesized to facilitate comparison to literature for infrared spectroscopy characterization and the SiO_2 supported catalysts are advantageous in some aspects, discussed in more detail below.

Table 5.1. Metal loading as determined by ICP, CO uptake, and dispersion of bimetallic AgPd and CuPd catalysts and monometallic Pd catalysts

Catalyst	**Ag wt%**	**Cu wt%**	**Pd wt%**	**(Ag/Cu):Pd (mol:mol)**	**CO uptake (µmol/g)**	**N_2O titration (µmol/g)**	**Dispersion (%)**	**Average particle size (nm)**
Ag/TiO_2	0.49	-	-	-	-	18.1	40	3.04 ± 1.67
Cu/TiO_2	-	3.91	-	-	-	109	18	2.67 ± 1.29
Cu/SiO_2	-	4.15	-	-	-	131	20	4.34 ± 1.93
$AgPd_{0.64}/TiO_2$	0.28	-	0.17	0.64	1.6	-	10	2.04 ± 0.85
$CuPd_{0.08}/TiO_2$	-	4.12	0.56	0.08	16.6	-	32	1.90 ± 0.51
$CuPd_{0.02}/TiO_2$	-	4.46	0.15	0.02	5.5	-	39	1.63 ± 0.43
$CuPd_{0.09}/SiO_2$	-	4.93	0.75	0.09	22.2	-	31	2.81 ± 1.98
Pd/TiO_2	-	-	0.52	-	7.8	-	16	1.07 ± 0.30
Pd/SiO_2	-	-	0.50	-	4.3	-	9.2	1.72 ± 0.90

To synthesize the bimetallic catalysts, Pd was deposited by controlled surface reactions using cyclopentadienyl Pd allyl, as described in Section 2.1.4. The uptake of this precursor was monitored using UV vis spectroscopy of the solution. UV vis spectra shown in Figure 5.1 indicate that the Pd precursor was taken up completely by the parent catalysts. Although Cp(Pd)allyl is partially deposited onto the TiO_2 support alone during control experiments, additional uptake upon deposition onto the Ag and Cu catalysts indicates the formation of bimetallic particles. Furthermore, the uptake of Cp(Pd)allyl onto the support is linearly related to the concentration used,[27] and therefore using concentrations below $1 \cdot 10^{-3}$ g Cp(Pd)allyl/g pentane in solution during synthesis reduces the uptake onto the support.

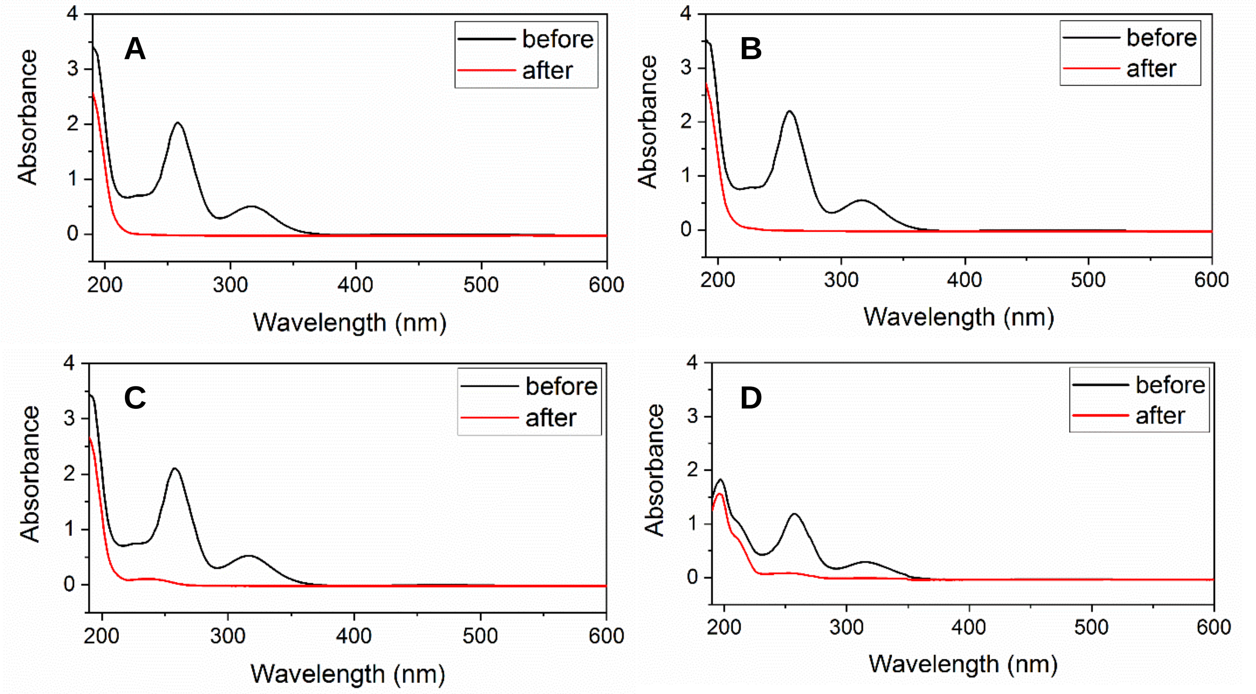

Figure 5.1 UV vis spectra showing the concentration of cyclopentadienyl Pd allyl in pentane, before (–) and after (–) mixing with the Ag/TiO$_2$ or Cu/TiO$_2$ parent catalyst in the synthesis of (A) AgPd$_{0.60}$/TiO$_2$, (B) CuPd$_{0.02}$/TiO$_2$, (C) CuPd$_{0.08}$/TiO$_2$, and (D) CuPd$_{0.09}$/SiO$_2$.

The bimetallic catalysts were characterized using CO chemisorption to measure Pd dispersion. The metal loading of each catalyst, as determined by ICP, and the Pd dispersion calculated from CO uptake are shown in Table 5.1. The dispersions of all the CuPd catalysts, with molar ratios of Cu:Pd between 0.02 and 0.09, are above 30%. The AgPd catalyst has a lower dispersion of 10%. We note that for each metal system, the dispersions are similar across the range of metal loadings used for the catalysts. This difference in dispersion between the Cu and Ag systems may be attributed to the differences in the relative surface and segregation energies for these two metal systems. For a CuPd alloy, the segregation energy suggests that

Pd has a slight preference to be on the surface of Cu, while for a AgPd alloy, Pd slightly prefers to be subsurface of the Ag.[28] We also note that adsorbate induced surface reconstruction has been widely reported to occur, particularly for CO adsorbed on bimetallic Pd.[29–31] As a result, the measured CO uptake may overestimate the surface Pd in the bimetallic catalysts as-synthesized due to diffusion of Pd to the surface.

The composition distribution for the CuPd bimetallic catalysts was measured using STEM-EDS analysis. The electron beam was placed on individual nanoparticles and EDS spectra quantified to measure the relative amount of each metal. The composition distributions, along with representative TEM images, are shown in Figure 5.2. For both the $CuPd_{0.08}/TiO_2$ and $CuPd_{0.02}/TiO_2$ catalysts, the distribution is broad (average compositions of 55.7 ± 33.5 at% Pd and 37.6 ± 35.4 at% Pd, respectively), with monometallic Cu as well as bimetallic CuPd particles of varied ratios. Some monometallic Pd nanoparticles are also present. This broad distribution of nanoparticle compositions suggests that there is also likely a broad distribution of surface composition and structures. In contrast, the $CuPd_{0.09}/SiO_2$ catalyst has a narrower distribution of particle compositions, with an average composition of 13.8 ± 10.9 at% Pd and most particles containing less than 15 atomic% Pd. In particular, no monometallic Pd particles were detected for this catalyst. This narrow distribution indicates that the Pd surface structures on the SiO_2 supported CuPd catalyst are uniform across the catalyst. We note that the close X-ray edge energies between Ag and Pd prevent a similar analysis on those catalysts.

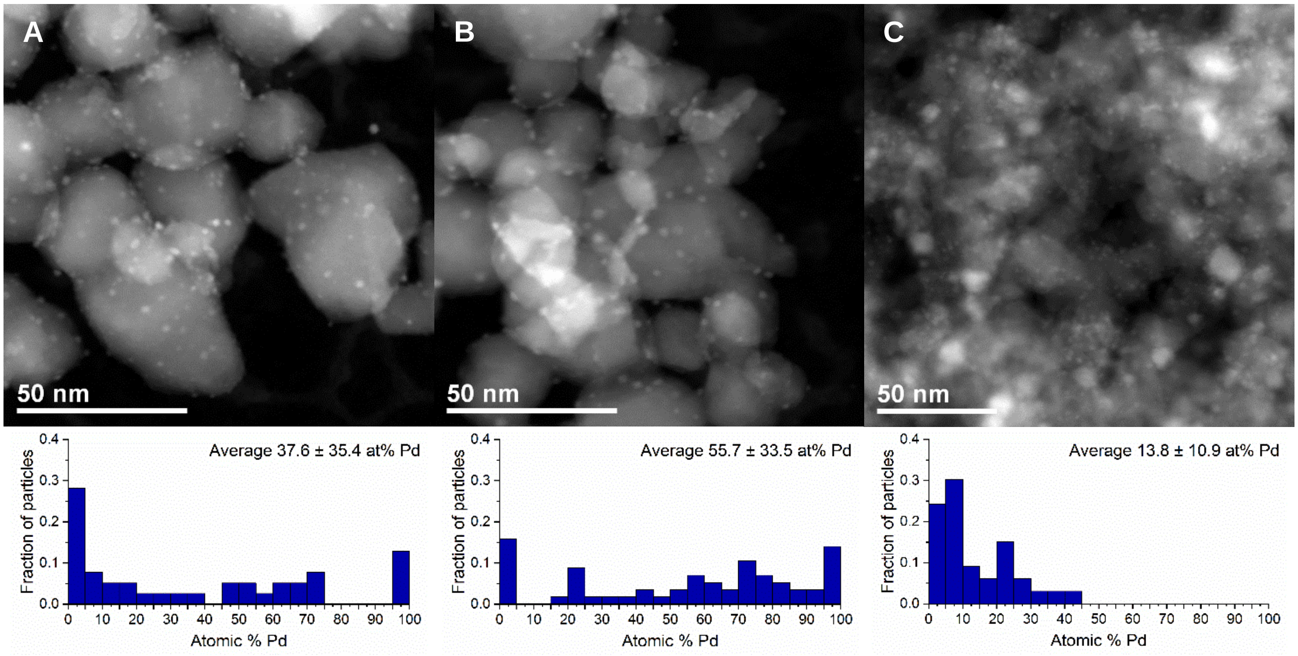

Figure 5.2. Representative STEM images (top) and nanoparticle composition distributions as determined by EDS analysis (bottom) for (A) $CuPd_{0.02}/TiO_2$, (B) $CuPd_{0.08}/TiO_2$, and (C) $CuPd_{0.09}/SiO_2$. For each composition distribution a minimum of 30 nanoparticles from multiple areas of the sample were analyzed.

5.2.2 Infrared spectroscopy

CO Adsorption

FTIR spectra of adsorbed CO were used to determine the structure of the surface Pd on the monometallic Pd and bimetallic CuPd catalysts. As shown in Figure 5.3, CO binds to CuPd catalysts in three configurations at room temperature. The peak at 2109 cm^{-1} is assigned to adsorption of CO on Cu sites[32], and the intensity of this peak decreases upon addition of Pd to the Cu parent catalyst, indicating a decrease in the available surface Cu species. This peak is observed in spectra reported by Goodman and coworkers for CO adsorbed on copper films.[33] Other work has reported a similar decrease in peak intensity upon addition of a promoting metal to a copper catalyst, indicating a decrease in the accessible copper surface.[32] In the spectra for CO adsorbed on $CuPd_{0.08}/TiO_2$, we observe a peak at 2058 cm^{-1} which can be assigned to CO linearly adsorbed to the top of Pd atoms[34] and a smaller broad peak at 1979 cm^{-1} which be attributed to a combination of CO adsorbed on bridge and 3-fold Pd sites.[35,36] On the $AgPd_{0.64}/TiO_2$ catalyst, a peak at 2070 cm^{-1} is observed, corresponding to CO on atop Pd sites. For comparison, the spectrum for CO adsorbed on monometallic Pd/TiO$_2$ is also shown. Although peaks for all three binding configurations for CO on Pd are present, the peak for CO adsorbed on atop sites is much smaller than the peaks for bridge and 3-fold adsorption. CO adsorption is more stable on bridge and 3-fold sites on Pd, and prefers these sites when they are accessible.[37,38] Therefore, the increase in the linear adsorption on the bimetallic catalysts indicates that Pd is present in primarily isolated species, diluted in the Cu or Ag nanoparticles. Additionally, the shift to lower wavenumbers for the peak for CO adsorbed on atop Pd sites on AgPd and CuPd compared to monometallic Pd/TiO$_2$ indicates greater electronic interaction between the Pd and parent metal, with the Pd gaining *d* electrons because of its higher electronegativity.[39] Similar to the CO chemisorption results discussed above, we note that these IR spectra may reflect some degree of a reconstructed catalyst, with Pd pulled to the surface by CO. This possible adsorbate-induced reconstruction is a result of the stronger binding energy of CO on Pd than on the Cu or Ag.[29,31,40,41]

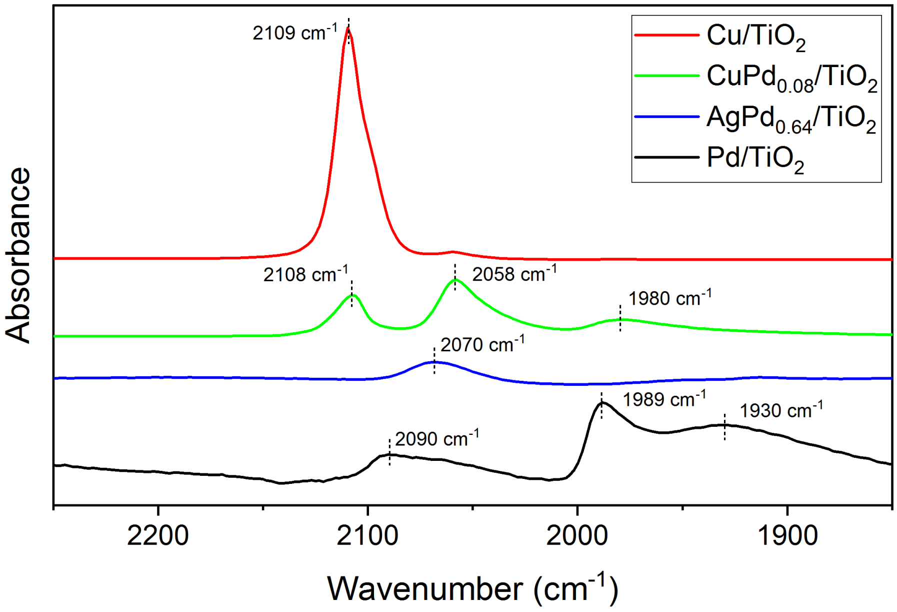

Figure 5.3. FTIR spectra of CO adsorbed on Cu/TiO$_2$ (red), CuPd$_{0.08}$/TiO$_2$ (green), AgPd$_{0.06}$/TiO$_2$ (blue), and Pd/TiO$_2$ (black) catalysts. Catalysts were pretreated under H$_2$ at 473 K for 2 hours prior to adsorption of 300 Torr of 1% CO and spectra were collected at room temperature. Spectra were normalized by the pellet areal density and Pd containing catalysts were also normalized by site density as measured by CO chemisorption.

Ethylene adsorption

We also investigated the adsorption of ethylene using infrared spectroscopy, since the nature of ethylene adsorption on the catalyst surface is hypothesized to be important in determining the selectivity during acetylene hydrogenation. For example, stronger adsorption of ethylene on the catalyst surface favors hydrogenation to ethane, while weaker adsorption of ethylene favors its desorption as a product.[42] The spectra in Figure 5.4 show the surface species formed after ethylene adsorption on each of the catalysts after gas phase ethylene was removed from the cell. Pd/SiO_2 is shown for comparison to literature, where three primary species have been reported: ~1327 cm^{-1} for ethylidyne species, 1412 cm^{-1} for di-σ-bonded ethylene, and 1524 cm^{-1} for π-bonded ethylene.[43] The spectrum for Pd/SiO_2 shown below has a peak at 1415 cm^{-1} and a small peak at 1348 cm^{-1} which are assigned to di-σ-bonded ethylene and ethylidyne, respectively and a small amount of π-bonded ethylene is observed (peak at 1524 cm^{-1}). Comparing the spectrum for Pd/SiO_2 to the spectrum for Pd/TiO_2, we assign the peak at 1442 cm^{-1} to di-σ-bonded ethylene on Pd on a TiO_2 support. This blue shift of ~30 cm^{-1} indicates a weaker adsorption of ethylene on the TiO_2 supported catalysts. This peak is shifted to slightly higher wavenumbers (~1444 cm^{-1}) for the bimetallic CuPd and AgPd catalysts. These spectra indicate that after introducing ethylene to the catalysts and then removing gas phase ethylene, the remaining surface ethylene is adsorbed primarily in a di-σ configuration on the bimetallic catalysts. There is a small peak at 1524 cm^{-1} on Pd/TiO_2 and $AgPd_{0.64}/TiO_2$, which corresponds to π-bonded ethylene. The adsorption of ethylene in both π-bonded and di-σ-bonded configurations on these catalysts is hypothesized to be due to the larger fraction of the surface as Pd. We also observe a π-bonded ethylene species bound to Cu at 1564 cm^{-1}.[44] The monometallic Pd catalysts and the AgPd catalysts form a small amount of ethylidyne on the surface (1351 cm^{-1}), while ethylidyne is not present on the CuPd bimetallic catalysts. It is important to note that removing the gas phase ethylene from the IR cell also allows weakly adsorbed surface species to desorb. Therefore, it is possible that other configurations of adsorbed ethylene are present under ethylene flow or reaction conditions but are removed upon purging the cell with inert gas.

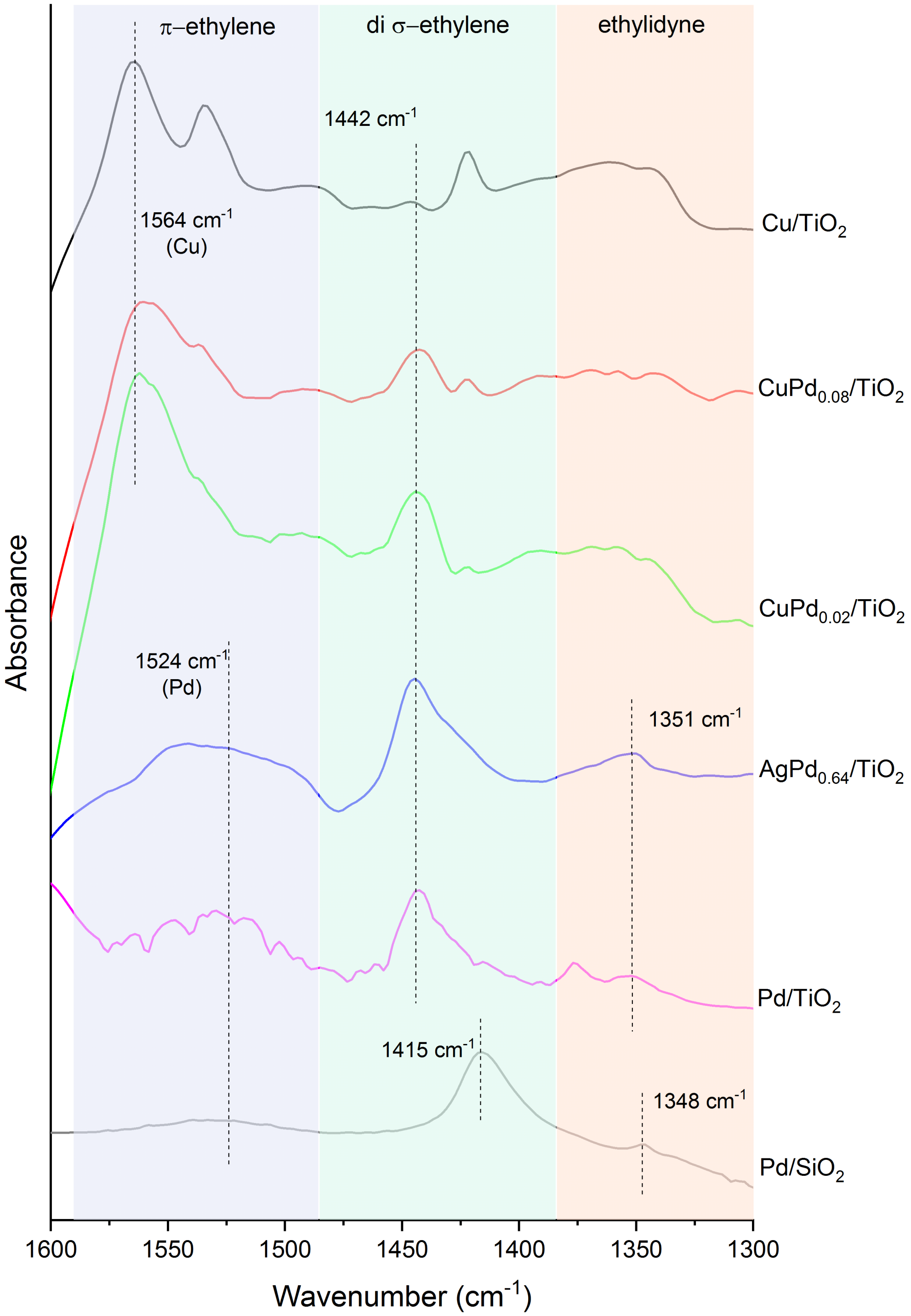

Figure 5.4. FTIR spectra of adsorbed ethylene on Cu, CuPd, AgPd, and Pd catalysts. All catalysts were reduced at 473 K under H_2 and cooled to 308 K for analysis. Monometallic Pd catalysts were purged with He at 473 K for 1 hour before cooling to avoid the formation of Pd hydride. The catalysts were exposed to flowing C_2H_4 for 30 minutes, then purged with He. The spectra shown represent the catalysts after He flow for 200 minutes.

In situ infrared spectroscopy

It is hypothesized that the absence of π-bonded ethylene in the above ethylene adsorption experiments on the $CuPd_{0.02}/TiO_2$ and $CuPd_{0.08}/TiO_2$ catalysts may be due to the weak adsorption of this species and subsequent desorption upon purging the IR cell with inert gas. Therefore, infrared spectroscopic studies of the catalysts under reaction flow can provide more insight into the surface species present under catalyst operating conditions. To reduce the contribution of the gas phase spectra which may dominate over peaks of adsorbed species, the concentrations of ethylene, acetylene, and hydrogen were reduced while maintaining the same ratio of these species as the flow reactor studies. First, the full reaction mixture was fed through the IR cell for 2+ hours to allow the catalyst to reach steady state. It can be observed in Figure 5.5, trace (i) that as the $CuPd_{0.02}/TiO_2$ catalyst was exposed to acetylene and ethylene, a negative peak around 3750 cm^{-1} appeared, indicating adsorption of species onto -OH functional groups on the support.[45] A broad peak from 3700-3500 cm^{-1} is also attributed to adsorption onto -OH functional groups which are involved in hydrogen bonding to various degrees.[45–47] Similar features were observed on the Cu/TiO_2 and Pd/TiO_2 catalysts (Figure 5.5B and C, trace (i)), as well as SiO_2 supported catalysts (Figure 5.6). These results indicate that some adsorption of the acetylene and ethylene occurs on both the TiO_2 and SiO_2 supports. It is hypothesized that the irreversibility of these peaks upon removal of acetylene and ethylene (Figure 5.5, traces (ii) and (iii)) indicates a change to the support structure such as -OH condensation. These same peaks are observed when only ethylene is introduced into the cell, therefore the changes are not due to the presence of hydrogen in the feed. The peaks from gas phase ethylene around 3000 cm^{-1} and 1400 cm^{-1} mask any C-C or C-H stretches of surface hydrocarbon species, therefore, we incrementally remove the acetylene and ethylene to monitor changes due to desorption of these species and their derivatives.

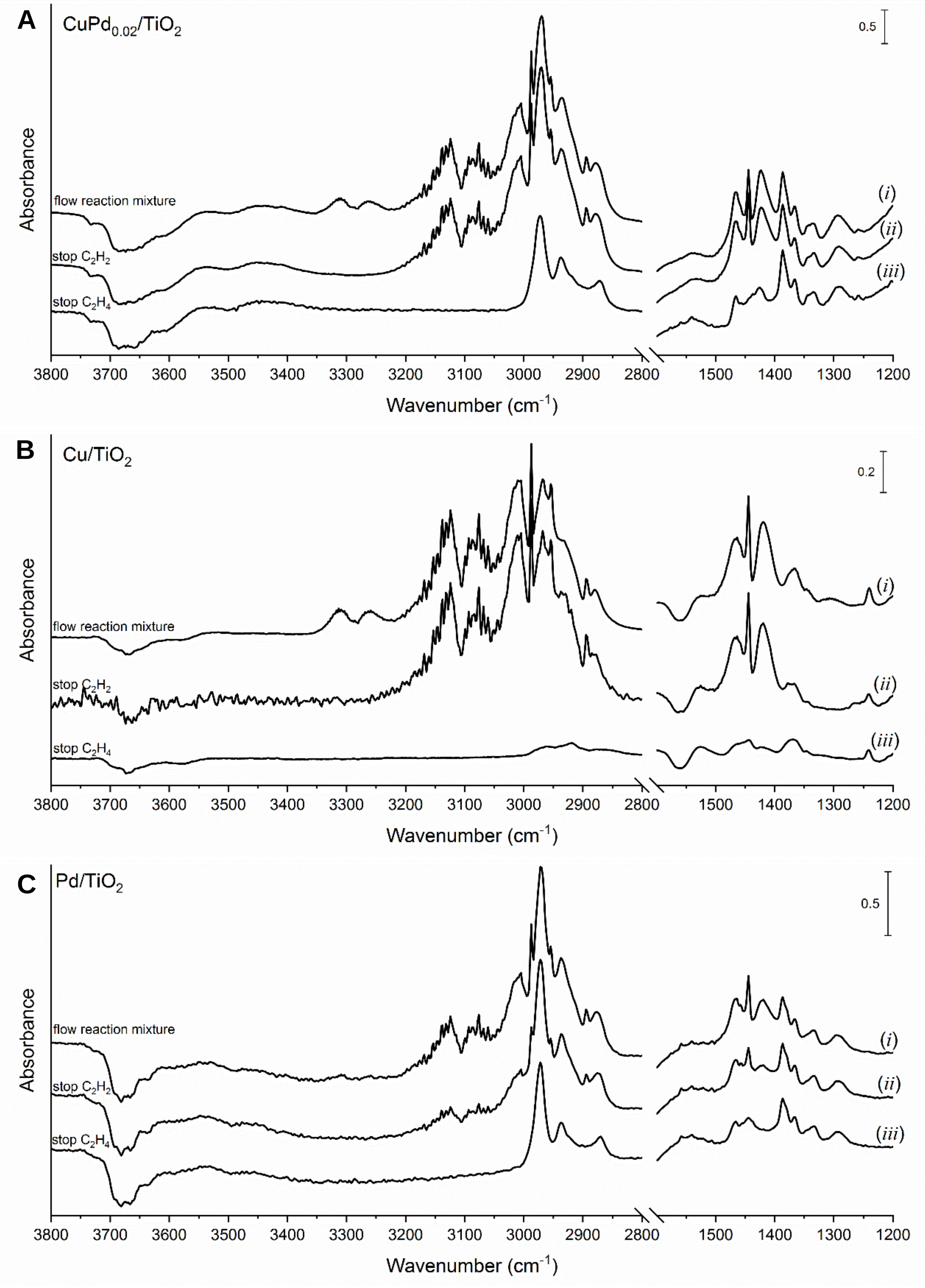

Figure 5.5. FTIR spectra of $CuPd_{0.02}/TiO_2$ (A), Cu/TiO_2 (B), and Pd/TiO_2 (C) at 313 K and 1 atm under (i) the dilute reaction mixture (0.083 bar C_2H_4, 0.003 bar C_2H_2, 0.083 bar H_2, balance Ar) (ii) after the removal of C_2H_2 from the reaction mixture, and (iii) after removal of C_2H_2 and C_2H_4 from the reaction mixture. The catalysts were reduced for 2 h at 473 K under H_2 prior to exposure to reaction gases. Spectra have been normalized by the catalyst pellet areal density.

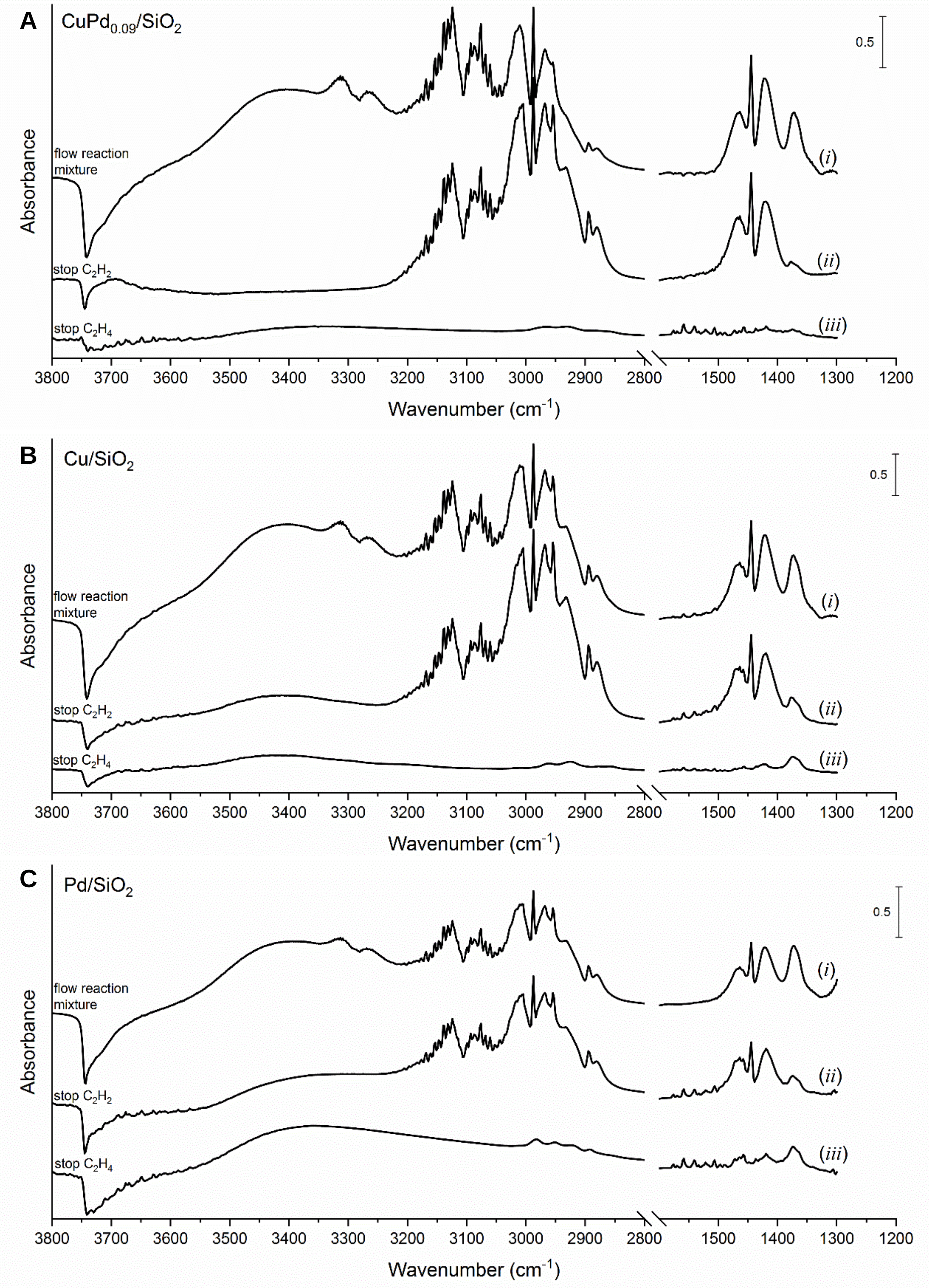

Figure 5.6. FTIR spectra of $CuPd_{0.09}/SiO_2$ (A), Cu/SiO_2 (B), and Pd/SiO_2 (C) at 313 K under (i) the dilute reaction mixture (0.083 bar C_2H_4, 0.003 bar C_2H_2, 0.083 bar H_2, balance Ar) (ii) after the removal of C_2H_2 from the reaction mixture, and (iii) after removal of C_2H_2 and C_2H_4 from the reaction mixture. The catalysts were reduced for 2 h at 473 K under H_2 prior to exposure to reaction gases. Spectra have been normalized by the catalyst pellet areal density.

After the catalyst was exposed to reaction flow at 313 K, the acetylene flow was stopped. On both the Pd/TiO_2 and $CuPd_{0.02}/TiO_2$ catalysts, minimal changes to the spectra were observed in Figure 5.5A and B, trace (ii) which indicates that either (1) the surface is covered with strongly binding acetylene and acetylene-derived species or (2) the reactive species are present in such low quantities that the IR measurement is not sensitive to the magnitude of the change in the spectra. Theoretical calculations have determined the adsorption energy of acetylene to be -1.78 eV on a Pd(111) surface and between -1.30 and -1.71 eV on AgPd/Pd(111) surfaces of varied compositions.[11] Acetylene is expected to be hydrogenated to a vinyl intermediate which binds more strongly to these surfaces with binding energies of between -2.84 and -2.22 eV on those same surfaces.[11] Therefore, it is possible that these species would not readily desorb after gas phase acetylene was removed. Additionally, the large peaks from gas phase ethylene may overlap the peaks for acetylene adsorbed on the surface. Small peaks at 3309 and 3260 cm^{-1} disappear due to the removal of gas phase acetylene. On the SiO_2 supported catalysts as well as SiO_2 support alone (Figure 5.6 and Appendix Figure C.1, trace (ii)), the peak at 1373 cm^{-1} decreases in intensity. This peak is assigned to an ethylidyne-type species on the SiO_2 support.

Then, the ethylene flow was stopped, and the catalyst was monitored under 9% hydrogen in argon flow. This change is expected to remove both gas phase ethylene from the cell and reactive surface species derived from ethylene. The remaining species on the catalyst surface are strongly bound and therefore are expected to be spectator species under reaction conditions. It is known that the selective hydrogenation of acetylene on Pd catalysts runs on a highly covered surface and that the coverage influences the binding strength of intermediates.[11,48] In the C-H stretching region, shown in Figure 5.5A, trace (iii), peaks at 3123 and 3075 cm^{-1} from gas phase ethylene disappear. Additionally, the intensity of the peaks between 3000 and 2800 cm^{-1} decreases. This region contains peaks attributed to CH stretches of both the gas phase ethylene and surface species, and peaks for surface species at 2972 cm^{-1}, 2937 cm^{-1}, and 2871 cm^{-1} remain after all ethylene has been purged from the IR cell. These peaks are assigned to surface vinylidene and ethylidyne.[19,24] It has been reported that acetylene can isomerize to vinylidene and that vinylidene is more stable on Pd.[24] Additionally, on Pt surfaces, ethylidyne and di-σ-bonded ethylene were observed as spectator species during acetylene hydrognation.[26] These peaks have the largest intensity on the Pd/TiO_2 catalyst and the intensity decreases slightly on the $CuPd_{0.02}$/TiO_2 catalyst, as shown in Figure 5.7. The intensity of analogous peaks on Pd/SiO_2 at 2982 cm^{-1}, 2951 cm^{-1}, 2924 cm^{-1}, and 2892 cm^{-1} is lower and then decreases further for peaks on the $CuPd_{0.09}$/SiO_2 catalyst at 2964 and 2932 cm^{-1} with a shoulder at 2858 cm^{-1}. These changes in peak intensity suggest that the bimetallic catalysts are less covered by ethylidyne and vinylidene spectator species than the monometallic Pd catalysts. Additionally, the similarity in peaks for these surface spectator species on $CuPd_{0.02}$/TiO_2 and Pd/TiO_2 suggests that this CuPd catalyst has structures similar to a monometallic Pd catalyst under these conditions. The differences between the SiO_2 and TiO_2 supported bimetallic catalysts are hypothesized to be due to the differences in the uniformity of the bimetallic nanoparticles, as shown by STEM-EDS analysis above. On the Cu/TiO_2 and Cu/SiO_2 catalysts, there are small peaks in this same region suggesting that minimal amounts of ethylidyne and vinylidene species are formed on Cu sites (Figure 5.5B and Figure 5.6B, trace (iii)).

There are also changes observed in the C-C stretching region between 1200-1500 cm^{-1} shown in Figure 5.5 and Figure 5.6. The peaks below 1400 cm^{-1} are attributed to solely surface species while peaks from gas phase ethylene as well as surface species are observed above 1400 cm^{-1}. On the $CuPd_{0.02}$/TiO_2, Cu/TiO_2, and Pd/TiO_2 catalysts, the peaks below 1400 cm^{-1} do not change upon removal of gas phase acetylene or ethylene (Figure 5.5, traces (ii) and (iii)), which indicates these are strongly bound surface spectator species. Some peaks are also observed when the reaction mixture is introduced to the SiO_2 and TiO_2 supports alone (Appendix Figure C.1). The peaks at 1366 cm^{-1} and 1374 cm^{-1} are assigned to ethylidyne-type species on the support and the peak at 1333 cm^{-1} is assigned to ethylidyne on Pd.[19,49] Peaks at wavenumbers higher than 1400 cm^{-1} are convoluted by species adsorbed on TiO_2 and SiO_2 and therefore further deconvolution of the peaks to assign particular intermediates was not carried out. The range of 1400-1600 cm^{-1} includes adsorbed ethylene and acetylene, as well as vinylidene. Although the adsorption energy of acetylene is much greater than the adsorption energy of ethylene,[18–21] the difference in concentration of these species in the feed likely leads to the presence of both species on the catalyst surface. The overall intensity of the peaks can be used to qualitatively measure the coverage of strongly adsorbed spectator species on the surface, shown in Figure 5.7.

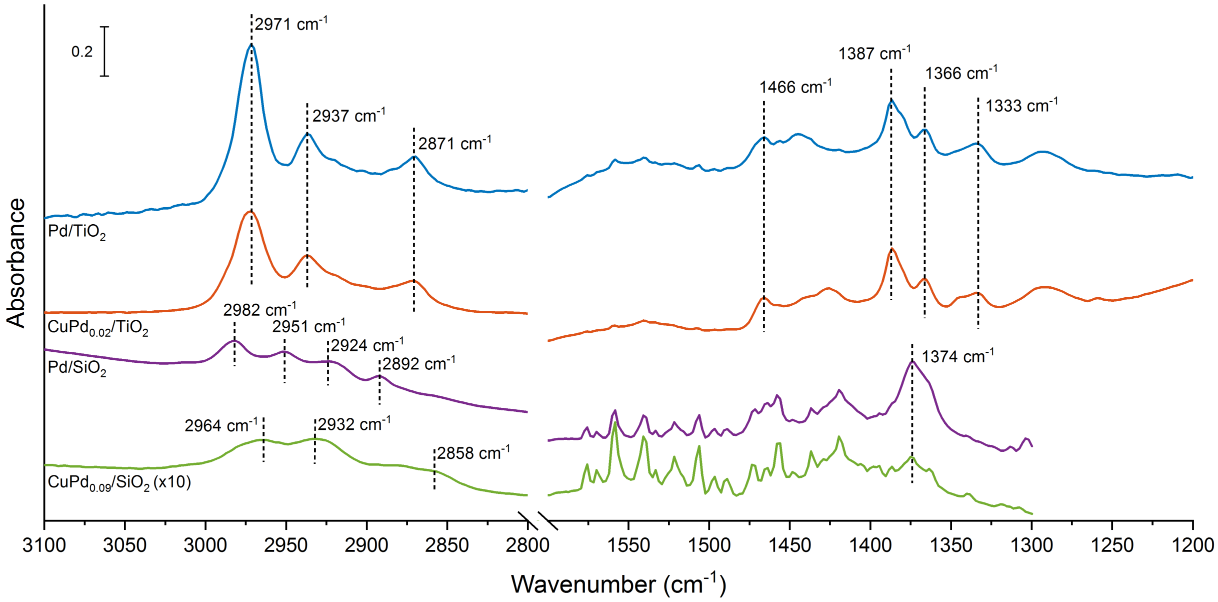

Figure 5.7. FTIR spectra of the Pd, CuPd, and Cu catalysts at 313 K after being exposed to reaction flow (0.083 bar C_2H_4, 0.003 bar C_2H_2, 0.083 bar H_2, balance Ar) for 2+ hours, under flow of C_2H_4 and H_2 for 2+ hours, then under flow of H_2 in Ar for 2+ hours. Spectra are normalized by the areal density of the catalyst pellet and the Pd sites measured by CO chemisorption. The intensity of the spectra for CuPd$_{0.09}$/SiO$_2$ has been multiplied by a factor of 10 for ease in observing the low intensity peaks.

The peak intensities, both in the 2800-3100 cm^{-1} range and 1200-1600 cm^{-1} range, are slightly lower for the CuPd$_{0.02}$/TiO$_2$ catalyst than for the Pd/TiO$_2$ catalyst. This difference indicates that the bimetallic nature of the CuPd surface slightly decreases the presence of spectator species on the Pd surface. The SiO$_2$ supported catalysts, however, both have decreased peak intensity, particularly at the higher wavenumber range. Additionally, the peaks for the bimetallic CuPd$_{0.09}$/SiO$_2$ catalyst are much smaller than the monometallic Pd/SiO$_2$. This result suggests that the influence of the support is key in determining both the structure of the metal nanoparticle surface and, as a result, the coverage of the metal surface under reaction conditions. The large differences between the TiO_2 and SiO_2 supported catalysts may stem from the difference in nanoparticle composition and uniformity that we measured using STEM-EDS analysis, discussed above in Figure 5.2. We note that all spectra shown in Figure 5.6 have been normalized by pellet areal density and Pd site density as measured by CO chemisorption, therefore the decrease in peak intensity for the bimetallic catalysts is separate from any decrease in intensity due to lower Pd site densities.

Additionally, for all catalysts, no changes were observed to the spectra upon removal of hydrogen to purge the IR cell with inert gas only.

5.2.3 Reaction Kinetics Studies

Activity and selectivity trends

Acetylene hydrogenation reactions were carried out over these AgPd, CuPd, and Pd catalysts at 313 K and 1 atm. A molar ratio of 1:25:25 C_2H_2:C_2H_4:H_2 was used for all reactions. We define the ethylene selectivity as:

$$S_{C_2H_4} = 1 - \left(\frac{C_2H_6}{C_2H_{2_{feed}} - C_2H_2}\right).$$

Because the selectivity is calculated based on acetylene consumed and it is possible for the ethylene in the feed to also be converted to ethane, a negative selectivity is possible and indicates hydrogenation of both acetylene and ethylene to ethane.

At acetylene conversions less than 2%, the monometallic Pd/TiO_2 catalyst is 95% selective to ethylene and the bimetallic catalysts supported on TiO_2 are more than 98% selective to ethylene, as shown in Figure 5.8A. Additionally, the Pd/SiO_2 catalyst is 93% selective to ethylene and the $CuPd_{0.09}/SiO_2$ catalyst is 97% selective to ethylene. These results indicate that the ethylene selectivity is enhanced by diluting the Pd in the Ag or Cu. This is hypothesized to be due to a weakened binding of intermediates on the Pd sites in a bimetallic catalyst, as has previously been reported in both theory and experimental studies.[6,7,50] We note that for all catalysts studied, the carbon balance was closed to >99% and there were no observed C_{4+} species, as have been previously reported to form over Pd catalysts.[51]

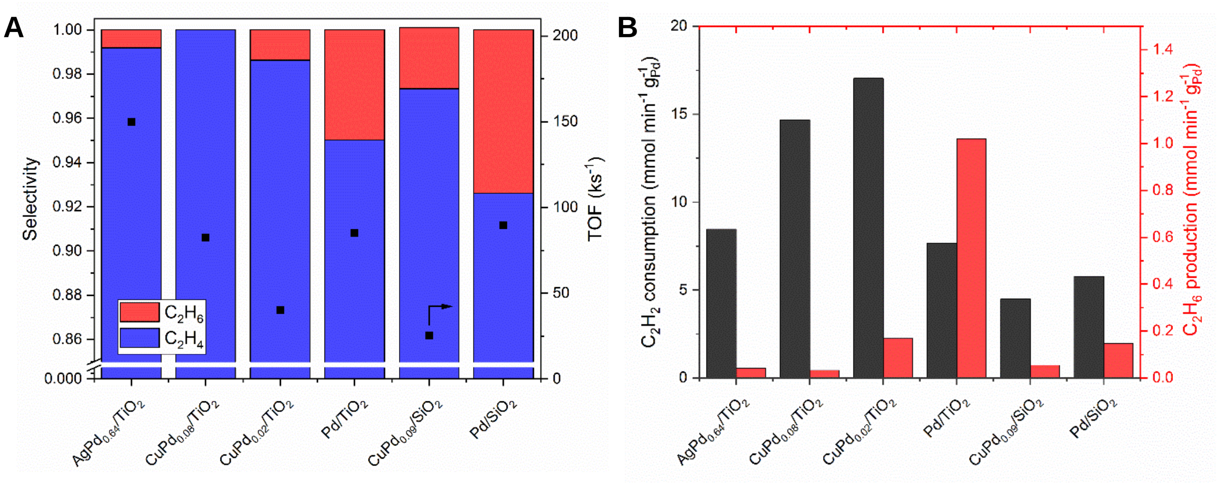

Figure 5.8. (A) Selectivities and turnover frequencies for AgPd, CuPd, and Pd catalysts and (B) the rate of acetylene consumption (black, left axis) and ethane production (red, right axis) during acetylene hydrogenation is shown for AgPd, CuPd, and Pd catalysts. Acetylene conversions were below 3% for all reactions. Reaction conditions: 313 K, 1 atm, 150 sccm, feed composition: 1% C_2H_2, 25% C_2H_4, 25% H_2, balance He.

Under the conditions investigated in this work, the monometallic Pd and bimetallic CuPd and AgPd catalysts are all stable over 12 hours of time-on-stream. The acetylene conversion turnover frequency (with sites counted by CO adsorption) as a function of time on stream is shown in Figure 5.9. The primary route for Pd catalyst deactivation during acetylene hydrogenation is hypothesized to be the formation of oligomeric species formed from C-C coupling reactions.[52,53] These species can form “green oil,” blocking active sites and subsequently deactivating the catalyst. Our observed catalyst stability is in agreement with the absence of C_{4+} products, detected by GC. It has been suggested in the literature that dimerization reactions are avoided over small Pd particles because of the small fraction of low index Pd surfaces present.[54] The small particle sizes of the catalysts studied in this work (Table 5.1), as well as the dilution of Pd sites by Cu and Ag reduces the presence of these Pd surfaces. Furthermore, the higher hydrogen pressures used in these reactivity studies, comparable to typical “front-end” acetylene hydrogenation conditions likely limits the deposition of carbon on the catalyst surface compared to “tail-end” conditions.[48]

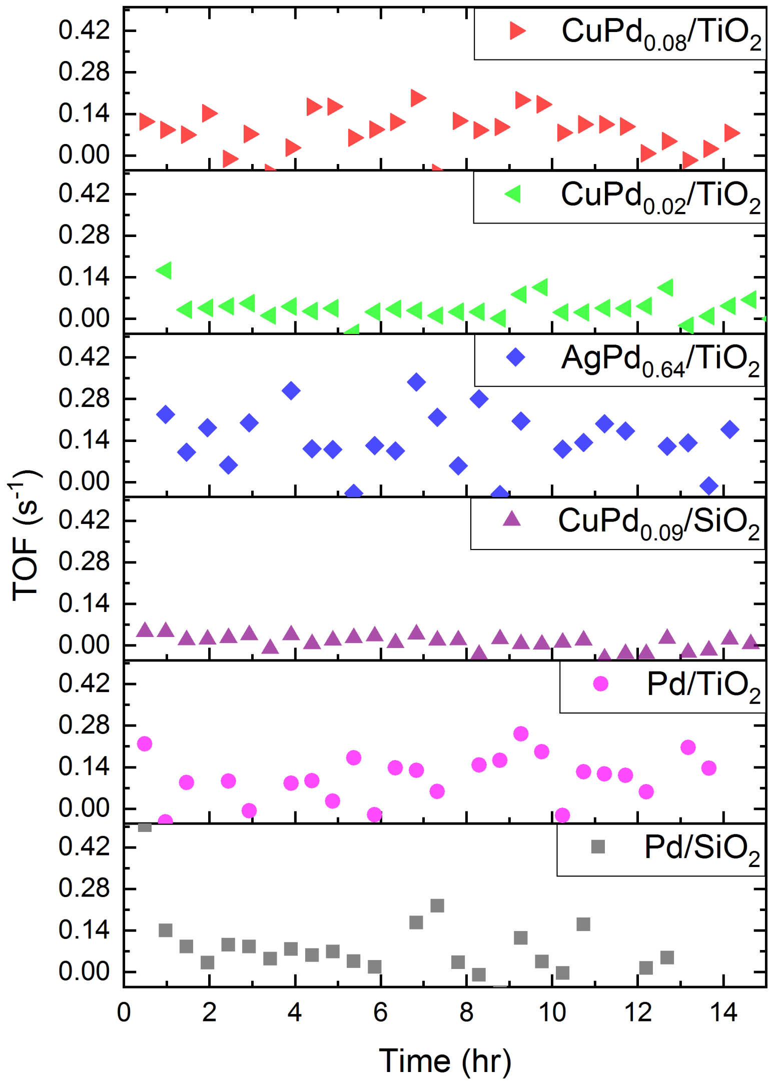

Figure 5.9. The acetylene conversion turnover frequency as a function of time on stream for the CuPd, AgPd and Pd catalysts. Reaction conditions: 313 K, 1 atm, 150 sccm, feed composition: 1% C_2H_2, 25% C_2H_4, 25% H_2, balance He. Sites were counted by CO adsorption using stoichiometry of 1 CO:1 Pd.

The rate of acetylene conversion and ethane production per gram of Pd are shown in Figure 5.8B. The monometallic catalysts have higher rates of ethane production (shown in red) than the bimetallic catalysts, although for all catalysts, the ethane production rate is much lower than the acetylene consumption rate (shown in black). The highest rates of acetylene consumption per gram of Pd are observed on the CuPd/TiO_2 catalysts, and both the $CuPd_{0.08}/TiO_2$ and $CuPd_{0.02}/TiO_2$ catalysts have approximately the same rate. The rates of acetylene conversion over the AgPd/TiO_2 catalysts are at least 2 times lower than the rate over the CuPd/TiO_2 catalysts. We hypothesize that this difference in activity between the bimetallic compositions may be due to the relative contributions of Cu and Ag to the hydrogenation activity. In both cases, although acetylene and ethylene adsorb on Pd, these species can also potentially adsorb on Cu and Ag. The binding energy of ethylene is weaker on Ag than on Cu, with DFT-calculated ethylene binding energies of -0.35 eV on Ag(110) and -0.63 eV on Cu(110).[55] Therefore, Ag may not interact sufficiently strongly with ethylene and acetylene to contribute to the overall conversion. We note that from the FTIR spectra of the reaction mixture over the Cu catalysts, there are not observed spectator species on Cu, however reactive ethylene and acetylene species would be expected to desorb rapidly and therefore would not be detected in the experiments described above. The rate of acetylene conversion per gram of Pd is higher over the TiO_2 supported catalysts than the SiO_2 supported catalysts, which indicates that TiO_2 may be influencing the overall activity. Partially reducible supports have been previously reported to induce partial charge transfer between the support and metal nanoparticle. In this system, electron transfer from the TiO_2 support to the Pd may enhance the overall rate.[56,57]

The turnover frequencies for acetylene consumption (with sites determined by CO adsorption) are shown in Figure 5.7A. The highest turnover frequency is observed for the bimetallic $AgPd_{0.64}/TiO_2$ catalyst. The high ratio of Ag:Pd in this catalyst may facilitate intimate contact in the bulk between the two metals, while the lower dispersion for AgPd compared to the CuPd catalysts may prevent the formation of contiguous Pd sites which bind intermediates more strongly. The $CuPd_{0.08}/TiO_2$ catalyst has a TOF of 83 ks^{-1} followed by $CuPd_{0.02}/TiO_2$ and $CuPd_{0.09}/SiO_2$ with TOFs of 40 ks^{-1} and 25 ks^{-1}, respectively. The decrease in TOF over the CuPd bimetallic catalysts compared to the monometallic Pd catalysts may be due to weakened binding of reactive intermediates on the surface. Although this weakened binding may contribute to the increased selectivity, since ethylene will desorb rather than undergo further hydrogenation, it may also lead to decreased coverage of acetylene. Thus, the improved selectivity achieved on the CuPd bimetallic catalysts comes at a cost of decreased acetylene consumption turnover frequency. A similar decrease in catalytic activity was observed by Leviness et al. for CuPd/Al_2O_3 catalysts.[14]

From the FTIR spectra of adsorbed ethylene and acetylene, a variety of surface species were observed. The peak intensity, however, was much higher on the TiO_2 supported catalysts than on the SiO_2 supported catalysts suggesting different coverages of spectator species. Since the activities of these bimetallic catalysts are not orders of magnitude different, this indicates that the sites that are occupied by spectator species are likely not the same sites as those sites occupied by reactive intermediates. Additionally, we determined that the ethylene selectivity over the CuPd/TiO_2 and CuPd/SiO_2 catalysts are similar. The EDS analysis determined that the nanoparticle composition distribution for these catalysts are different – the TiO_2 supported samples having a broad distribution of nanoparticle compositions including monometallic Pd particles and the SiO_2 supported sample having a uniform nanoparticle composition distribution without monometallic Pd particles. From FTIR analysis of adsorbed CO, we determined that isolated Pd species are on the catalyst surface in the presence of CO but the ethylene adsorption spectra indicate that contiguous Pd species are likely present under those conditions. Therefore, it can be concluded that isolated Pd sites are not required to achieve high ethylene selectivity, as was the case for hydrodechlorination (Chapter 4). In the CuPd catalysts studied in this work, the surface Pd distribution is highly dependent on the conditions and adsorbates present. Therefore, the enhanced selectivity and activity achieved over bimetallic AgPd and CuPd catalysts can be attributed to predominantly electronic interactions between the metals rather than geometric effects. The role of electronic effects in the enhanced selectivity over bimetallic catalysts compared to monometallic Pd catalysts is supported in the literature by reports of a shifted *d*-band in Pd alloys.[12]

5.3 Conclusions

In this work, an improved selectivity towards ethylene has been demonstrated during acetylene hydrogenation over CuPd and AgPd catalysts, compared to monometallic Pd catalysts. The CuPd bimetallic catalysts are more than 99% selective for the desired hydrogenation of ethylene, while monometallic Pd catalysts were less than 95% selective to ethylene. CuPd/TiO_2 catalysts give the highest rate on a per Pd basis, while the bimetallic AgPd catalyst gives the highest TOF. Thus, the change in the Pd surface structure achieved by forming bimetallic CuPd nanoparticles improves the selectivity to ethane and improves the dispersion of Pd, but the rate per surface Pd is decreased. FTIR spectra of adsorbed CO indicate that Pd is isolated from other Pd species on the CuPd nanoparticle surfaces; however, the spectra of adsorbed ethylene indicate a di-σ binding configuration which requires neighboring Pd atoms. Because of the potential for adsorbate induced surface reconstruction, additional characterization is necessary to better understand the bimetallic catalyst surface under reaction conditions. FTIR spectra of the catalysts after exposure to reaction conditions suggest that electronic effects dominate the enhanced selectivity for AgPd and CuPd catalysts for selective hydrogenation of acetylene.

5.4 Materials and Methods

5.4.1 Catalyst Synthesis

The parent Ag/TiO_2 catalyst was synthesized using deposition precipitation and the parent Cu/TiO_2 and Cu/SiO_2 catalysts were synthesized using ion exchange as described in Section 2.1.3. The bimetallic AgPd and CuPd catalysts were synthesized by controlled surface reactions, described in Section 2.1.4. For comparison, monometallic Pd/TiO_2 and Pd/SiO_2 catalysts with a loading of 0.5 wt% Pd were synthesized using incipient wetness impregnation, described in Section 2.1.2.

5.4.2 Characterization

Adsorption measurements

Surface Ag and Cu sites were measured using N_2O titration, following the methods of Seyedmonir et al.[58] and Evans et al.[59], respectively, and described in Section 2.2.2.

Surface Pd sites were measured using CO chemisorption, described in Section 2.2.1. The catalyst samples were first reduced at 473 K in H_2 for 6 h (heating rate 0.75 K/min) and then evacuated to 10^{-5} Torr. Adsorption of CO was carried out at 293 K and the catalyst sample was evacuated for 30 minutes between collection of the first and second isotherms.

Fourier transform infrared spectroscopy

Fourier transform infrared spectroscopy of adsorbed species on the catalyst samples was carried out as described in Section 2.2.3. Prior to analysis, the samples were reduced in H_2 for 4h at 473 K (heating rate 5 K/min). For all experiments, spectra were collected with a resolution of 4 cm^{-1} spectra were normalized by the pellet area density (pellet area/pellet mass).

For CO adsorption experiments, the cell was evacuated to 10^{-5} Torr after reduction and then a background spectrum was collected at room temperature under vacuum. Then, 300 Torr of 1% CO (Airgas) was introduced to the cell and equilibrated for 10 minutes. The cell was then cooled to 103 K and equilibrated for an additional 10 minutes. The cell was evacuated to remove weakly adsorbed CO and spectra were collected at the desired temperature as the cell was allowed to warm.

For ethylene adsorption experiments, the cell was held at 308 K and purged with Ar after reduction. A background was collected and then ethylene (2.5 Grade, Praxair) was flowed through the cell for 30 minutes. Then, the cell was purged with Ar and spectra were collected.

For in situ experiments under reaction conditions, the cell was purged with Ar (UHP, Airgas) after reduction and the cell was cooled to 313 K. A background was collect in Ar and then the reaction mixture of 0.083 bar C_2H_4, 0.003 bar C_2H_2 (Airgas), 0.083 bar H_2 (Airgas), and balance Ar was fed to the cell. After collecting spectra for 2+ hours, the acetylene flow was stopped. After collecting spectra for an additional 2+ hours under C_2H_4, H_2, and Ar flow, the ethylene flow was stopped. Spectra were collected under H_2 and Ar flow, and then under Ar only.

For all FTIR spectra, comparisons between Pd containing catalysts were made with spectra normalized by the Pd site density in addition to the catalyst pellet areal density.

5.4.3 Reaction Kinetics Measurements

Catalysts were diluted in silica gel (Davisil Grade 636, 35-60 mesh, Sigma-Aldrich) then loaded into a ½-inch outer diameter, 304 stainless steel reactor between quartz wool (Ohio Valley Specialty) and silica chips (Sigma-Aldrich) for activity testing. The reactor was heated with a furnace (Applied Test Systems) and aluminum blocks were placed around the reactor to ensure isothermal operation. The temperature was controlled using a PID controller (Love Controls) with a K-type thermocouple placed between the aluminum block and used for temperature control. He (Industrial Grade, Airgas), H_2 (Industrial Grade, Airgas), C_2H_4 (CP Grade, Airgas), and C_2H_2 (Industrial Grade, Airgas) were delivered by mass flow controller (Brooks 5890E) and used without further purification. Prior to reaction, the catalyst bed was calcined in air (Breathing Air, Airgas) at 723 K for 90 minutes (heating rate 10 K/min) and then reduced in H_2 (Industrial Grade, Airgas) at 473 K for 3 hours. The reactor was purged with inert gas at 473 K for 30 minutes then cooled to reaction temperature (typically 313 K). Reactant and product analysis was performed by Shimadzu GC-2014 with He carrier gas using an FID detector and an RT Alumina Bond column for analysis of ethane, ethylene, and acetylene. All measurements were carried out at an acetylene conversion of less than 2% and rate and selectivity values represent averages over 10 hours time on stream. The carbon balance for all reactions was >99%.

5.5 Acknowledgements

This material is based upon work supported by the US Department of Energy, Office of Basic Energy Sciences (DE-SC0014058). The authors gratefully acknowledge use of facilities and instrumentation at the UW-Madison Wisconsin Centers for Nanoscale Technology (wcnt.wisc.edu) partially supported by the NSF through the University of Wisconsin Materials Research Science and Engineering Center (DMR-1720415).

5.6 References

(1) Guo, Z.; Liu, Y. Y.; Liu, Y. Y.; Chu, W. *Appl. Surf. Sci.* **2018**, *442*, 736–741.

(2) Derrien, M. L. *Selective Hydrogenation Applied to the Refining of Petrochemical Raw Materials Produced by Steam Cracking*; Elsevier Science Publishers B.V., 1986; Vol. 27.

(3) Nguyen Thanh, C.; Didillon, B.; Sarrazin, P.; Cameron, C. Selective hydrogenation catalyst and a process using that catalyst. 6054409, 2000.

(4) Borodziński, A.; Bond, G. C. *Catal. Rev.* **2006**, *48*, 91–144.

(5) Gannon, R. E.; Manyik, R. M.; Dietz, C. M.; Sargent, H. B.; Thribolet, R. O.; Schaffer, R. P. In *Kirk-Othmer Encyclopedia of Chemical Technology*; John Wiley & Sons, Inc.: Hoboken, NJ, USA, 2003.

(6) Pei, G. X.; Liu, X. Y.; Yang, X.; Zhang, L.; Wang, A.; Li, L.; Wang, H.; Wang, X.; Zhang, T. *ACS Catal.* **2017**, *7*, 1491–1500.

(7) Mei, D.; Neurock, M.; Smith, C. M. *J. Catal.* **2009**, *268*, 181–195.

(8) Borodziński, A.; Bond, G. C. *Catal. Rev.* **2008**, *50*, 379–469.

(9) McCue, A. J.; Anderson, J. A. *Front. Chem. Sci. Eng.* **2015**, *9*, 142–153.

(10) Bos, A. N. R.; Westerterp, K. R. *Chem. Eng. Process. Process Intensif.* **1993**, *32*, 1–7.

(11) Sheth, P. A.; Neurock, M.; Smith, C. M. *J. Phys. Chem. B* **2005**, *109*, 12449–12466.

(12) Zhao, Z.; Zhao, J.; Chang, X.; Zha, S.; Zeng, L.; Gong, J. *AIChE J.* **2018**, *65*, aic.16492.

(13) Tsapina, A. M.; Tsyrulnikov, P. G.; Glyzdova, D. V.; Shlyapin, D. A.; Vedyagin, A. A.; Kaichev, V. V.; Trenikhin, M. V.; Trigub, A. L.; Lavrenov, A. V. *Appl. Catal. A Gen.* **2018**, *563*, 18–27.

(14) Leviness, S.; Nair, V.; Weiss, A. H.; Schay, Z.; Guczi, L. *J. Mol. Catal.* **1984**, *25*, 131–140.

(15) Feng, Q.; Zhao, S.; Wang, Y.; Dong, J.; Chen, W.; He, D.; Wang, D.; Yang, J.; Zhu, Y.; Zhu, H.; Gu, L.; Li, Z.; Liu, Y.; Yu, R.; Li, J.; Li, Y. *J. Am. Chem. Soc.* **2017**, *139*, 7294–7301.

(16) Studt, F.; Abild-Pedersen, F.; Bligaard, T.; Sorensen, R. Z.; Christensen, C. H.; Norskov, J. K. *Science* **2008**, *320*, 1320–1322.

(17) Sheth, P. A.; Neurock, M.; Smith, C. M. *J. Phys. Chem. B* **2003**, *107*, 2009–2017.

(18) Gates, J. A.; Kesmodel, L. L. *J. Chem. Phys.* **1982**, *76*, 4281–4286.

(19) Kesmodel, L. L.; Gates, J. A. *J. Electron Spectros. Relat. Phenomena* **1983**, *29*, 307–312.

(20) Kesmodel, L. L.; Waddill, G. D.; Gates, J. A. *Surf. Sci.* **1984**, *138*, 464–474.

(21) Gates, J. A.; Kesmodel, L. L. *Surf. Sci. Lett.* **1982**, *120*, L461–L467.

(22) Ormerod, R. M.; Lambert, R. M.; Hoffmann, H.; Zaera, F.; Wang, L. P.; Bennett, D. W.; Tysoe, W. T. *J. Phys. Chem.* **1994**, *98*, 2134–2138.

(23) Azad, S.; Kaltchev, M.; Stacchiola, D.; Wu, G.; Tysoe, W. T. *J. Phys. Chem. B* **2000**, *104*, 3107–3115.

(24) Clotet, A.; Ricart, J. M.; Pacchioni, G. *J. Mol. Struct. Theochem* **1998**, *458*, 123–129.

(25) Clotet, A.; Pacchioni, G. *Surf. Sci.* **1996**, *346*, 91–107.

(26) Krooswyk, J. D.; Waluyo, I.; Trenary, M. *ACS Catal.* **2015**, *5*, 4725–4733.

(27) Ball, M. R.; Rivera-Dones, K. R.; Stangland, E.; Mavrikakis, M.; Dumesic, J. A. *J. Catal.* **2019**, *370*, 241–250.

(28) Ruban, A. V.; Skriver, H. L.; Nørskov, J. K. *Phys. Rev. B - Condens. Matter Mater. Phys.* **1999**, *59*, 15990–16000.

(29) van Spronsen, M. A.; Daunmu, K.; O’Connor, C. R.; Egle, T.; Kersell, H.; Oliver-Meseguer, J.; Salmeron, M. B.; Madix, R. J.; Sautet, P.; Friend, C. M. *J. Phys. Chem. C* **2018**, *123*, acs.jpcc.8b08849.

(30) Gao, F.; Wang, Y.; Goodman, D. W. *J. Am. Chem. Soc.* **2009**, *131*, 5734–5735.

(31) Soto-Verdugo, V.; Metiu, H. *Surf. Sci.* **2007**, *601*, 5332–5339.

(32) Ro, I.; Liu, Y.; Ball, M. R.; Jackson, D. H. K.; Chada, J. P.; Sener, C.; Kuech, T. F.; Madon, R. J.; Huber, G. W.; Dumesic, J. A. *ACS Catal.* **2016**, *6*, 7040–7050.

(33) Xu, X.; Goodman, D. W. *J. Phys. Chem.* **2005**, *97*, 683–689.

(34) Rebelli, J.; Rodriguez, A. A.; Ma, S.; Williams, C. T.; Monnier, J. R. *Catal. Today* **2011**, *160*, 170–178.

(35) Gao, F.; Goodman, D. W. *Chem. Soc. Rev.* **2012**, *41*, 8009.

(36) Giorgi, J. B.; Schroeder, T.; Bäumer, M.; Freund, H.-J. *Surf. Sci.* **2002**, *498*, L71–L77.

(37) Yudanov, I. V.; Sahnoun, R.; Neyman, K. M.; Rösch, N.; Hoffmann, J.; Schauermann, S.; Johánek, V.; Unterhalt, H.; Rupprechter, G.; Libuda, J.; Freund, H. J. *J. Phys. Chem. B* **2003**, *107*, 255–264.

(38) Loffreda, D.; Simon, D.; Sautet, P. *Surf. Sci.* **1999**, *425*, 68–80.

(39) Primet, M.; Mathieu, M. V.; Sachtler, W. M. H. *J. Catal.* **1976**, *44*, 324–327.

(40) Greeley, J.; Mavrikakis, M. *J. Catal.* **2002**, *208*, 291–300.

(41) Martin, N. M.; Van Den Bossche, M.; Grönbeck, H.; Hakanoglu, C.; Zhang, F.; Li, T.; Gustafson, J.; Weaver, J. F.; Lundgren, E. *J. Phys. Chem. C* **2014**, *118*, 1118–1128.

(42) Xu, L.; Stangland, E. E.; Mavrikakis, M. *J. Catal.* **2018**, *362*, 18–24.

(43) Hill, J. M.; Shen, J.; Watwe, R. M.; Dumesic, J. A. *Langmuir* **2000**, *16*, 2213–2219.

(44) Sheppard, N.; De La Cruz, C. *Adv. Catal.* **1996**, *41*, 1–112.

(45) Deiana, C.; Fois, E.; Coluccia, S.; Martra, G. *J. Phys. Chem. C* **2010**, *114*, 21531–21538.

(46) Zhuravlev, L. T. *Colloids Surfaces A Physicochem. Eng. Asp.* **2000**, *173*, 1–38.

(47) Love, A. M.; Carrero, C. A.; Chieregato, A.; Grant, J. T.; Conrad, S.; Verel, R.; Hermans, I. *Chem. Mater.* **2016**, *28*, 5495–5504.

(48) Mei, D.; Sheth, P.; Neurock, M.; Smith, C. *J. Catal.* **2006**, *242*, 1–15.

(49) Beebe, T. P.; Yates, J. T. *J. Phys. Chem.* **2005**, *91*, 254–257.

(50) Liu, Y.; He, Y.; Zhou, D.; Feng, J.; Li, D. *Catal. Sci. Technol.* **2016**, *6*, 3027–3037.

(51) Vignola, E.; Steinmann, S. N.; Al Farra, A.; Vandegehuchte, B. D.; Curulla, D.; Sautet, P. *ACS Catal.* **2018**, *8*, 1662–1671.

(52) Takht Ravanchi, M.; Sahebdelfar, S. *Appl. Catal. A Gen.* **2016**, *525*, 197–203.

(53) Sárkány, A.; Guczi, L.; Weiss, A. H. *Appl. Catal.* **1984**, *10*, 369–388.

(54) Kang, J. H.; Shin, E. W.; Kim, W. J.; Park, J. D.; Moon, S. H. *J. Catal.* **2002**, *208*, 310–320.

(55) Bernardo, C. G. P. M.; Gomes, J. A. N. F. *J. Mol. Struct. THEOCHEM* **2002**, *582*, 159–169.

(56) González, C. A.; Bartoszek, M.; Martin, A.; De Correa, C. M. *Ind. Eng. Chem. Res.* **2009**, *48*, 2826–2835.

(57) Kumar, J. V.; Pasha, N.; Babu, N. S.; Lingaiah, N.; Prasad, P. S. S. *Catal. Today* **2008**, *141*, 120–124.

(58) Seyedmonir, S. R.; Strohmayer, D. E.; Geoffroy, G. L.; Vannice, M. A.; Young, H. W.; Linowski, J. W. *J. Catal.* **1984**, *87*, 424–436.

(59) Evans, J. W.; Wainwright, M. S.; Bridgewater, A. J.; Young, D. J. *Appl. Catal.* **1983**, *7*, 75–83.

Chapter 6. Summary and Future Directions

6.1 Research Summary

Fundamental studies of heterogeneous catalysts are needed in order to understand the relationships between structure and catalyst performance. By understanding the active site structure for a given catalyst and reaction system, rational design of novel and improved catalysts can occur. As synthetic techniques become more advanced and a wider range of stable structures are accessible, structure-activity and structure-selectivity relationships will guide the target catalyst structures. Furthermore, these studies can guide the development of catalysts for chemical transformations that are currently unselective or not economically feasible. Improving a variety of catalytic processes will be necessary to meet the chemical, energy, and environmental challenges of modern society.

In this work, bimetallic catalysts were synthesized using a controlled surface reaction approach. This technique allows for the deposition of small amounts of one metal onto a parent catalyst of another metal – in this case, Pd deposited onto either Au, Ag, or Cu. During the synthesis process, the deposition is monitored to identify conditions where Pd deposition is selective to the parent metal and not to the catalyst support. Although the cyclopentadienyl Pd allyl precursor used in these studies interacts with the titania, silica, and carbon supports to varying extents, it was determined that deposition of the precursor onto the support decreases with decreasing solution concentration. Additionally, the uptake on the precursor increases in the presence of the parent metal, indicating that Pd deposition onto the parent metal is preferred over the oxide support. Thus, bimetallic catalysts with a uniform distribution of nanoparticle size and composition are synthesized.

To determine the surface and bulk structure of the resulting catalysts, a variety of catalyst characterization techniques were applied. Chemisorption techniques were used to measure the palladium dispersion and quantify the distribution of Pd between the surface and bulk of nanoparticles. Infrared spectroscopy of adsorbed molecules was used to determine how the formation of bimetallic particles modifies adsorption onto Pd sites as compared to monometallic Pd catalysts. Both geometric and electronic changes are observed, indicating the possible role of both effects on catalytic activity. Electron microscopy and energy dispersive X-ray spectroscopy as well as X-ray absorption spectroscopy were used to determine the degree to which the nanoparticles are uniform across the catalyst. This combined characterization approach provides a variety of information about the catalyst structure which can be used in understanding and interpreting catalyst activity and selectivity measurements.

This work investigated three catalyst systems and three reaction systems: AuPd, AgPd, and CuPd used for hexanol amination, hydrodechlorination of 1,2-dichloroethane, and selective hydrogenation of acetylene. Across these systems, the same controlled surface reaction technique was used to deposit Pd during catalyst synthesis and similar characterization studies were used to investigate the resulting structures. For each reaction system, the Pd alloy was chosen based on literature precedent, however it is expected that the other Pd-Group IB metal systems would also be active and could provide additional insight into the structure-performance relationships for these materials.

In Chapter 3, the gas-phase amination of 1-hexanol using ammonia was studied over $AuPd/TiO_2$ catalysts. The bimetallic active sites for these catalysts have been characterized using CO chemisorption and XAS techniques, and the absence of monometallic Pd species in the AuPd catalysts was confirmed using UV-vis and STEM-EDS analysis. The bimetallic catalysts exhibit synergy between Au and Pd, as the rate of hexanol conversion increases from 8.7 μmol ks^{-1} (μmol total $Pd)^{-1}$ over Pd/TiO_2 to up to 42 μmol ks^{-1} (μmol total $Pd)^{-1}$ over $AuPd/TiO_2$ with a Pd/Au atomic ratio of 0.06. The rate of hexanol conversion is also enhanced with respect to Au content, with a 5-fold increase in the total Au-normalized rate from Au/TiO_2 to $AuPd_{0.67}/TiO_2$. As Pd is added to Au/TiO_2 in increasing quantities, the production rate of primary species (i.e., hexylamine and hexanenitrile) is preferentially increased. The rate of dihexylamine production increases to a lesser extent, while trihexylamine formation remains relatively constant across Pd loadings. Moreover, trihexylamine, which cannot be formed via the condensation of dihexylamine and hexanol, is shown to be produced via the secondary aldimine, *N*-hexylidene hexylamine. The AuPd bimetallic catalysts also exhibit reduced hydrogenolysis activity compared to monometallic Pd/TiO_2.

In Chapter 4, the hydrodechlorination of 1,2-dichloroethane to form ethane, ethylene, and chloroethane was investigated over AgPd catalysts. AgPd catalysts were synthesized on SiO_2, TiO_2, and carbon supports using controlled surface reactions to form well defined active site structures. The formation of bimetallic AgPd structures is most effective for AgPd/TiO_2, followed by AgPd/C and then AgPd/SiO_2 catalysts. FTIR spectra of adsorbed CO suggest that Pd is well dispersed on the Ag nanoparticles for the TiO_2-supported catalyst, while more contiguous Pd sites are present on the SiO_2-supported catalyst. Ethylene selectivities of up to 97% and 82% are achieved on AgPd/TiO_2 and AgPd/C catalysts, respectively. The AgPd/SiO_2 catalyst is 91% selective to ethane. These results indicate that the well dispersed Pd achieved at low Pd loadings on TiO_2 and carbon is selective to ethylene, while the contiguous Pd species formed on SiO_2 are selective to ethane. Furthermore, increased reactivity is correlated to high ethylene selectivity.

In Chapter 5, the selective hydrogenation of acetylene in ethylene-rich streams was investigated over AgPd and CuPd catalysts on SiO_2 and TiO_2 supports. STEM-EDS analysis of the CuPd catalysts indicates that the composition of the CuPd/SiO_2 nanoparticles are more uniform than the CuPd/TiO_2 nanoparticles. FTIR spectra of adsorbed CO on these catalysts indicate that Pd is primarily present on the surface isolated from other Pd species, however, spectra of adsorbed ethylene suggest a di-σ binding configuration which requires neighboring Pd atoms. These adsorption studies indicate the dynamic nature of the catalyst surface dependent on interactions with adsorbates and the importance of in-situ characterization in identifying active sites. The AgPd catalyst has the highest acetylene conversion turnover frequency (150 ks^{-1}), while the CuPd/TiO_2 and monometallic Pd/TiO_2 catalysts have TOFs between 40 and 85 ks^{-1}. All of the titania supported bimetallic catalysts have ethylene selectivities above 98% while the monometallic Pd/TiO_2 catalyst has an ethylene selectivity of 95%. This increased ethane production over the monometallic Pd/TiO_2 catalyst corresponds to a more than 6x increase in the rate of ethane production per gram of Pd. The change in surface Pd structure that results from the formation of CuPd nanoparticles improves the ethylene selectivity and Pd dispersion while decreasing the rate per surface Pd. Ongoing work aims to further elucidate the differences observed in catalyst structure, reactivity, and selectivity between the AgPd and CuPd systems, as well as between the SiO_2 and TiO_2 supported catalysts.

6.2 Future Directions

In the work described in this thesis, controlled surface reactions have been used as an approach to synthesize uniform bimetallic catalysts. The importance of the interaction between the Pd precursor and catalyst support has been identified and it was determined that the effectiveness of bimetallic formation differs across supports. The Pd surface structure was determined to change with the Pd loading, offering a way through which to tune the types of Pd sites. This study provides detailed information about structure activity and structure-selectivity relationships for different reactions over Pd-based bimetallic catalysts.

However, there are additional areas in which there are open questions regarding controlling catalyst structure via synthesis parameters. Future work to deconvolute the support effect and the metal system effect in the formation of uniform bimetallic particles will be useful in detailed understanding of the structure-performance relationships. In the hydrodechlorination study, the AgPd/SiO_2 catalyst was less selective to ethylene than the AgPd/TiO_2 catalyst, indicating monometallic Pd structures which were confirmed by FTIR studies. In the acetylene hydrogenation work, however, the difference in ethylene selectivity between CuPd/SiO_2 and CuPd/TiO_2 is much smaller, suggesting that the surface structures are more similar. Furthermore, from XAS studies, the AgPd/TiO_2 catalyst has effective mixing of the Ag and Pd, while the CuPd/TiO_2 catalyst has a broad distribution of CuPd nanoparticle mixing, from STEM-EDS analysis. XAS analysis of the CuPd catalysts, on both TiO_2 and SiO_2 supports will provide information about the bulk mixing of the metals.

From control experiments of Cp(Pd)allyl deposition onto TiO_2 and SiO_2 supports, the concentration dependence on the uptake onto the support is similar between the two supports, shown in Figure 6.1. This result suggests that the differences in the resulting bimetallic catalysts on the two supports is caused by some factor other than the interaction between the Pd and support.

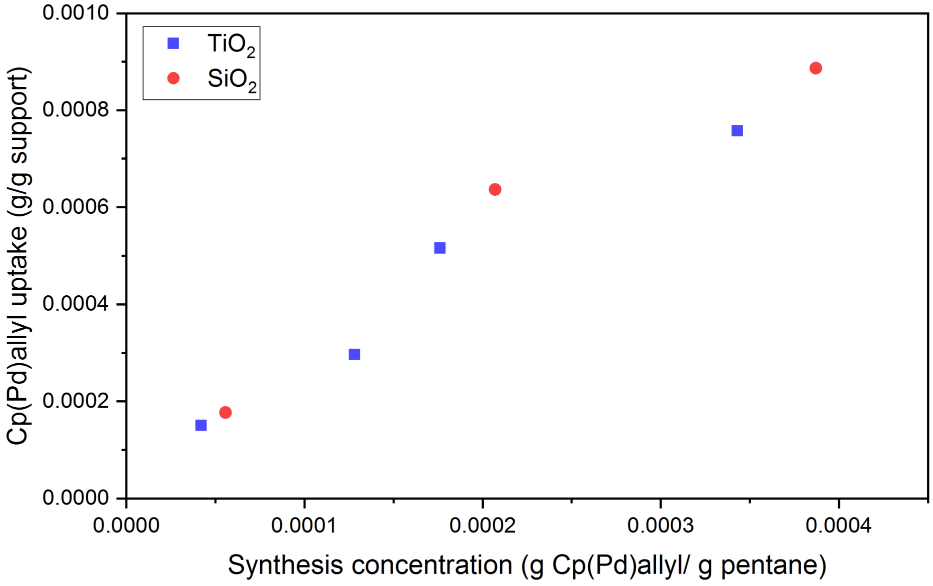

Figure 6.1. Uptake of Cp(Pd)allyl (g/g support) as a function of the synthesis concentration (g Cp(Pd)allyl/g pentane) for both TiO_2 and SiO_2.

The surface area between the TiO_2 and SiO_2 supports are quite different (45 and 280 m^2/g, respectively) and therefore the uptake of Pd onto the support may be more complex. Studies of Cp(Pd)allyl uptake onto a high surface area TiO_2 (typically 100-300 m^2/g) could help elucidate whether uptake is truly agnostic to the support identity, or whether the current results are obscured by the differences in surface area. Differences in Pd uptake on the different supports could explain the different composition distributions obtained by STEM-EDS analysis for $CuPd/TiO_2$ and $CuPd/SiO_2$.

Also, in the work discussed above, the Pd was added as the second metal to facilitate its dispersion and minimize the formation of monometallic Pd structures. However, for the acetylene hydrogenation study, although the bimetallic catalysts are more selective, the monometallic Pd catalysts still achieve high ethylene selectivity. Therefore, in this system, the presence of contiguous Pd ensembles is not as detrimental to the desired selectivity as it is for the hydrodechlorination of 1,2-dichloroethane. Accessing a wider range of catalysts structures and compositions could help inform what the desired and undesired active site structures are. One approach to the synthesis of catalysts ranging from 100% Cu to 100% Pd would be to carry out controlled surface reactions using a Pd parent and depositing Cu (an example precursor would be bis(dimethylamino-2-propoxy)copper). In this manner, it would be feasible to maintain small nanoparticle size while decreasing the Cu fraction and increasing the Pd fraction of the nanoparticles.

Additionally, the investigation of multiple metal systems for acetylene hydrogenation would help elucidate the relative contributions of geometric and electronic effects in the bimetallic system. The geometry of the surface Pd species can be determined using FTIR of adsorbed CO, and it is hypothesized that at similar molar ratios of M:Pd, the surface Pd should be in similar geometric configurations. When comparing different parent metals, however, it is expected that the electron transfer between Pd and either Au, Ag, or Cu would differ. Therefore, the adsorption strength of CO, ethylene, and/or acetylene would be expected to change across the metal systems. By quantifying the adsorption strength of these species through TPD experiments as the parent metal is changed and comparing adsorption strength with acetylene conversion rate, the optimal binding strength can be estimated. From this study of AuPd, AgPd, and CuPd catalysts, it can be determined what additional promoters might further enhance reactivity and selectivity.

Furthermore, there are additional reaction studies that can improve understanding of the acetylene hydrogenation reaction over AgPd and CuPd catalysts. It was observed that calcination in air prior to reaction was required to decrease the activation time of the catalyst; when the fresh catalyst was only reduced prior to reaction, more than 24 hours time-on-stream were required for the activity to increase to the steady state value. When the calcination was conducted prior to reduction, the catalysts did not exhibit this long activation period under reactive conditions. X-ray photoelectron spectroscopy and XAS studies of the catalysts at varied points during the pretreatment could be used to elucidate the changes in metal oxidation state and metal coordination to determine what surface changes lead to the decreased activation period under reaction conditions.

Additionally, reaction kinetics studies will be useful in understanding the role of the second metal on the Pd activity for acetylene hydrogenation. It has previously been reported that the activation barrier for ethylene hydrogenation in the presence of acetylene decreases for a AgPd catalyst compared to a Pd catalyst, but without acetylene, the activation barriers for AgPd and Pd are similar.[1] The activation energy for acetylene hydrogenation has also been reported to decrease for a AgPd catalyst compared to Pd Measuring the activation energies for both acetylene and ethylene hydrogenation can help elucidate the role of the Group IB metal in improving the ethylene selectivity. Comparing the reaction orders over both monometallic Pd and bimetallic catalysts can complement the in situ infrared spectroscopy studies to determine the role of surface species. Since Pd catalysts are known to be highly covered under acetylene hydrogenation conditions, measuring the acetylene order can provide information about the strength of intermediate binding and the role of vacant sites. It has been suggested that the more negative the C_2H_2 reaction order the more strongly adsorbed the C_2H_2 or its formed isomers are on the catalyst surface.[2] Typically, for Pd catalysts, H_2 orders have been measured to be between 1 and 1.4, indicating weak adsorption on the Pd surface.[3,4] Measuring the reaction orders can provide insight into the nature of changes to adsorption of reactive and spectator species between monometallic catalysts and the different bimetallic systems.

Additionally, ongoing work in our group is investigating these Pd based catalysts using steady state isotopic transient kinetic analysis for acetylene hydrogenation. This work aims to determine the surface coverage under reaction conditions and determine how the Group IB metal influences the catalyst surface. A combination of additional catalyst synthesis studies and reaction studies for acetylene hydrogenation over bimetallic Pd-Group IB catalysts can improve our understanding of the active sites for hydrogenation and related chemistry.

6.3 References

(1) Zea, H.; Lester, K.; Datye, A. K.; Rightor, E.; Gulotty, R.; Waterman, W.; Smith, M. *Appl. Catal. A Gen.* **2005**, *282*, 237–245.

(2) Zhang, Y.; Diao, W.; Williams, C. T.; Monnier, J. R. *Appl. Catal. A Gen.* **2014**, *469*, 419–426.

(3) Molero, H.; Bartlett, B. F.; Tysoe, W. T. *J. Catal.* **1999**, *181*, 49–56.

(4) Borodziński, A.; Bond, G. C. *Catal. Rev.* **2006**, *48*, 91–144.

Appendices

Appendix A. Supplemental Information for Chapters 2 & 3

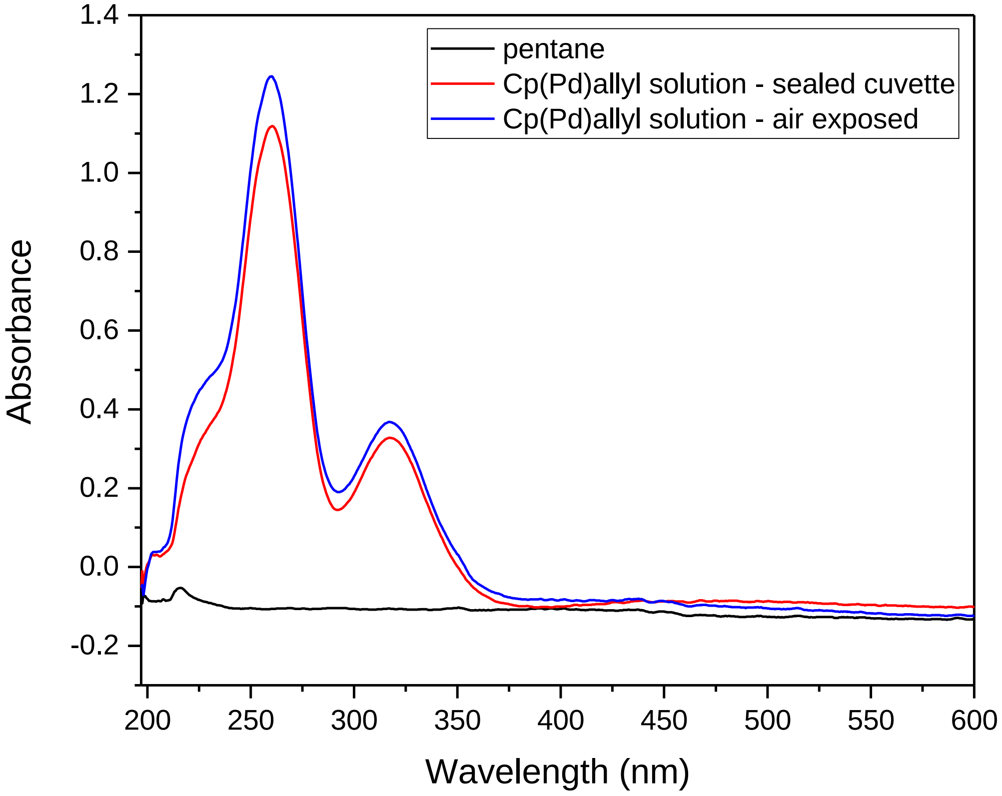

Figure A.1. UV vis spectra of Cp(Pd)allyl in anhydrous pentane prepared in an inert atmosphere and sealed in a cuvette in the glove box and kept under inert gas for analysis (red), and transferred to a cuvette in air for analysis (blue).

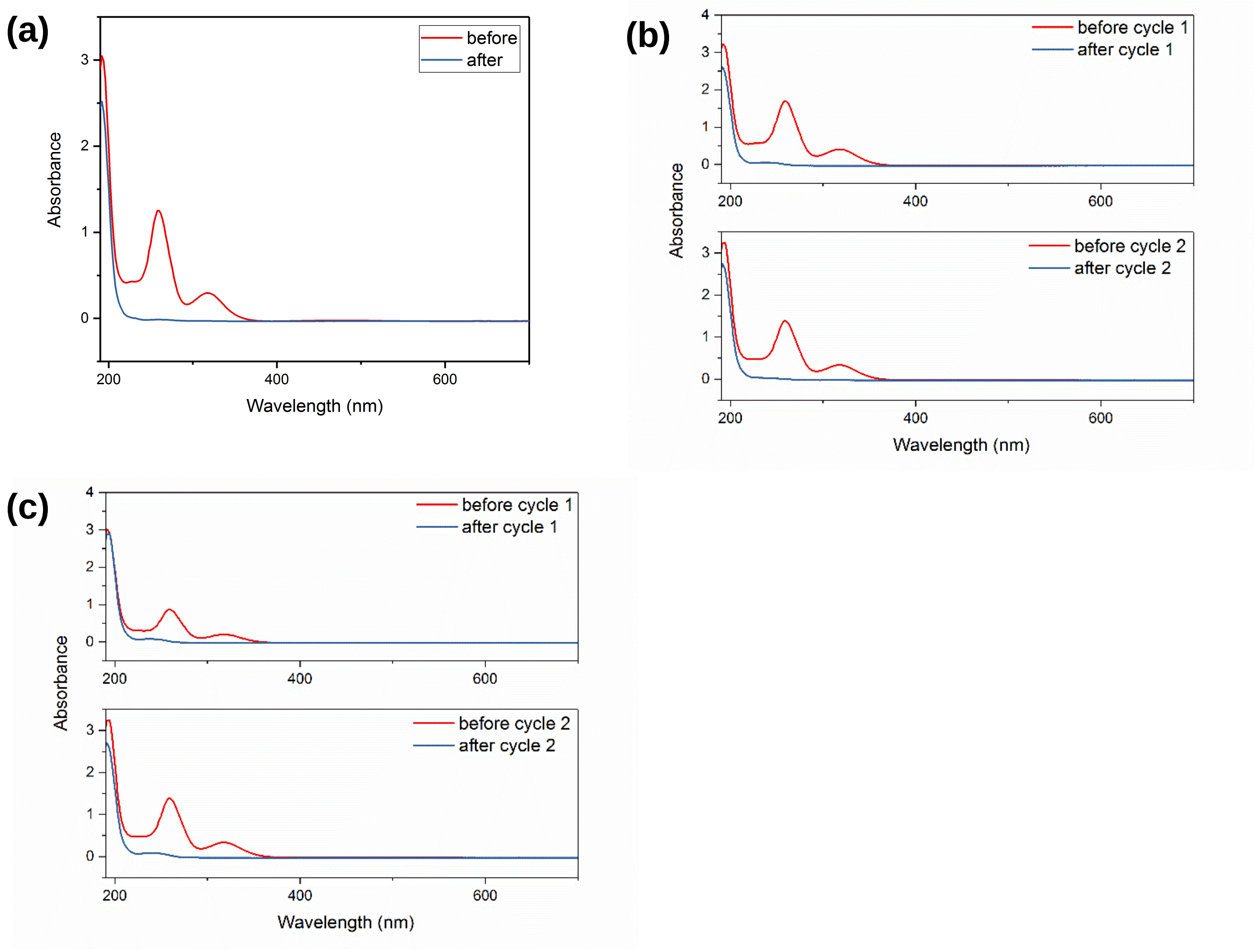

Figure A.2. UV Vis Spectra of Cp(Pd)allyl solution before and after contact with Au/TiO_2 catalyst during synthesis of (a) $AuPd_{0.06}/TiO_2$, (b) $AuPd_{0.55}/TiO_2$, and (c) $AuPd_{0.67}/TiO_2$

Table A.1. Site density and dispersion from CO chemisorption experiments using different pretreatment conditions to determine the extent of strong metal support interaction effects

Catalyst	Pretreatment	Site density (μmol/g)	Dispersion (%)
$AuPd_{0.55}/TiO_2$	Red. 533 K	2.0	7.0
	Calc. 673K, Red. 533 K	1.1	3.8
Pd/TiO_2	Red. 533 K	7.3	15
	Red. 673 K	5.7	13

Table A.2. Equilibrium constants for various steps in the amination of hexanol with ammonia, calculated from gas phase Gaussian calculations. The coupled cluster ccsd(t)/cc-pvtz method was used. Species were approximated by their two-carbon analogs (i.e. ethanol, ethanenitrile, diethylamine, etc.).

			K_{eq}
Hexanol +H_2	⇌	Hexane + H_2O	$6.4\text{x}10^{9}$
Hexanol	⇌	Hexanal + H_2O	$1.1\text{x}10^{-1}$
Hexanal + NH_3	⇌	Hexylimine + H_2O	$4.7\text{x}10^{-3}$
Hexylimine	⇌	Hexanenitrile + H_2	$1.7\text{x}10^{3}$
Hexylimine + H_2	⇌	Hexylamine	$1.0\text{x}10^{3}$
Hexylamine + Hexanal	⇌	N-hexylidene hexylamine + H_2O	$1.4\text{x}10^{-3}$
N-hexylidene hexylamine + H_2O	⇌	Dihexylamine	$2.1\text{x}10^{4}$
N-hexylidene hexylamine + hexanal +$2H_2$	⇌	Trihexylamine + H_2O	$6.2\text{x}10^{6}$

Using PBE+D3 and m062x/def2tzvp methods, it was confirmed that Gibbs free energy changes for the reaction steps approximated using C2 species were equivalent to the Gibbs free energy changes calculated for C6 species. The Gibbs free energy changes are shown for hexanenitrile + H_2 <-> hexylamine.

Method	**2C**	**6C**
PBE ΔG	0.06	0.05
MO6 ΔG	0.27	0.27

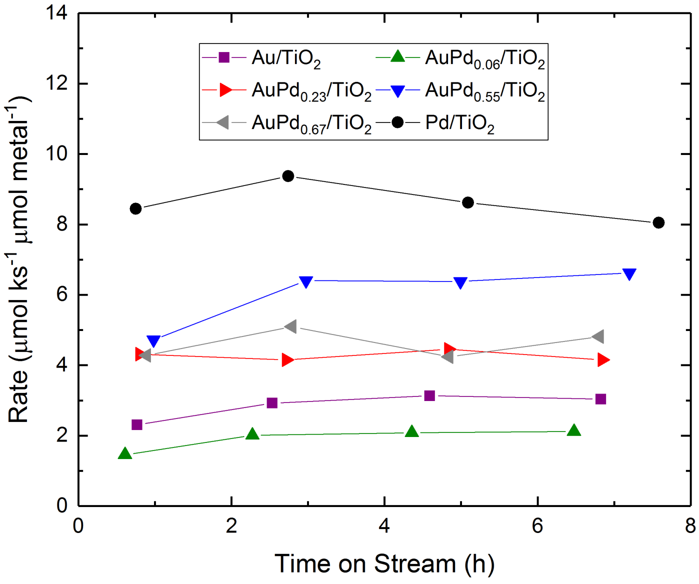

Figure A.3. Hexanol conversion rates, based on product formation (weighted by the number of moles of hexanol required to form one mole of product), for the various catalysts versus time-on-stream. Conditions: 503 K, 1 atm (0.07 kPa hexanol, 2.5 kPa NH_3, 51 kPa H_2, and balance He), 16-24% hexanol conversion.

Appendix B. Supplemental Information for Chapter 4

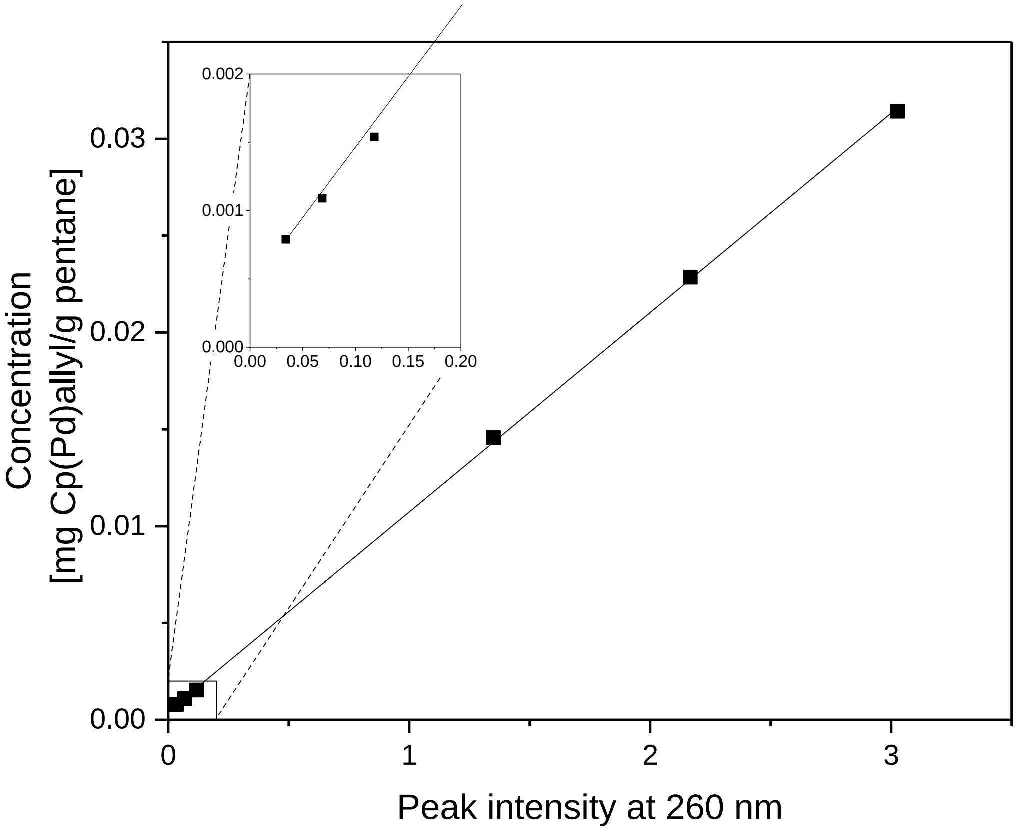

Figure B.1. Calibration curve for concentration of Cp(Pd)allyl in pentane as a function of UV vis peak intensity at 260 nm. The absorbance is linear with respect to Cp(Pd)allyl concentration up to an absorbance of 3.

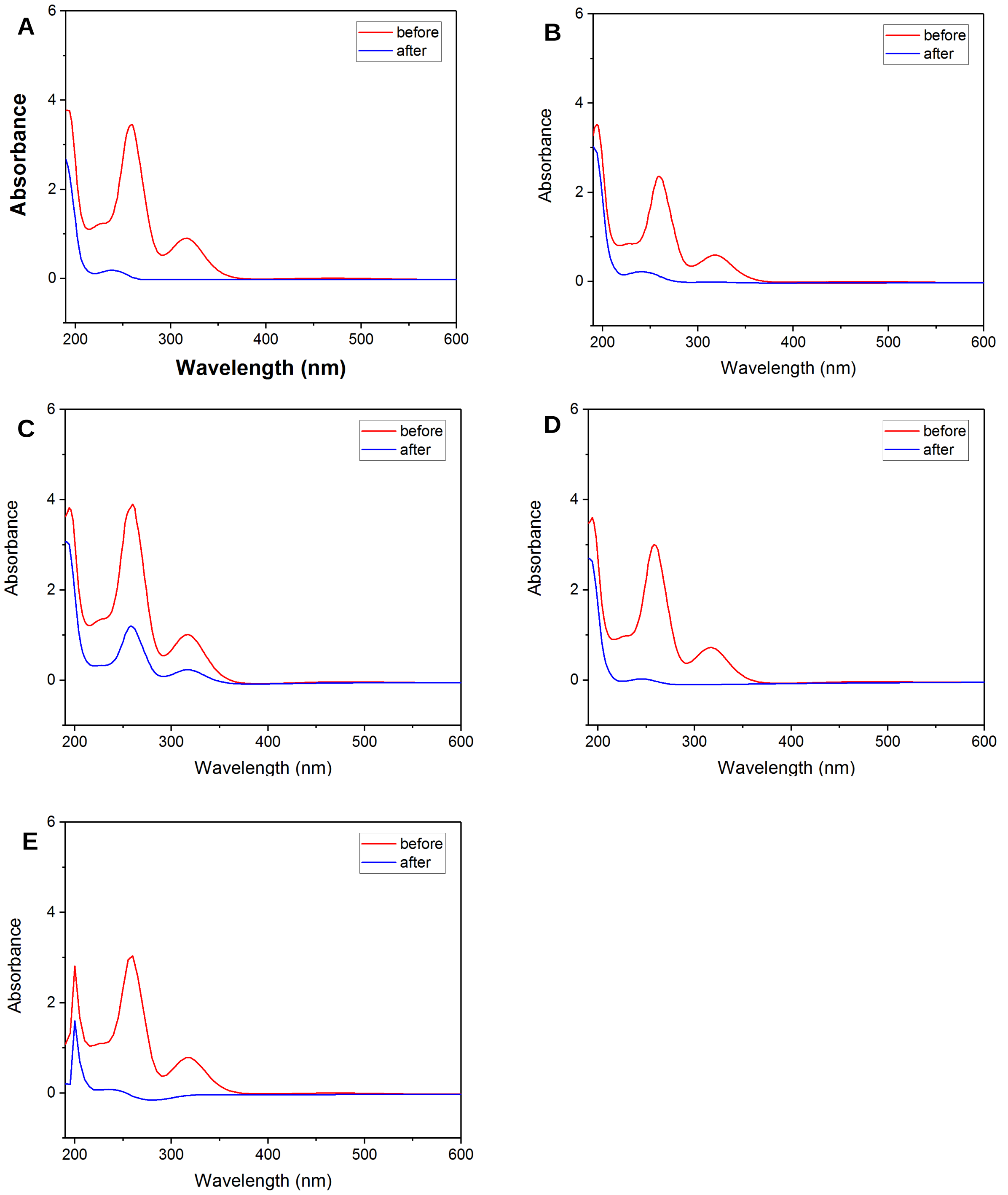

Figure B.2. UV vis spectra of cyclopentadienyl palladium allyl in n-pentane before and after mixing with (a) TiO_2 at a concentration of 1.8 mg/g n-pentane, (b) TiO_2 at a concentration of 3.8 mg/g n-pentane, (c) high temperature treated carbon, (d) untreated carbon, and (e) SiO_2. Solutions were diluted and calibration curves were used to calculate the uptake of the Cp(Pd)allyl by the support.

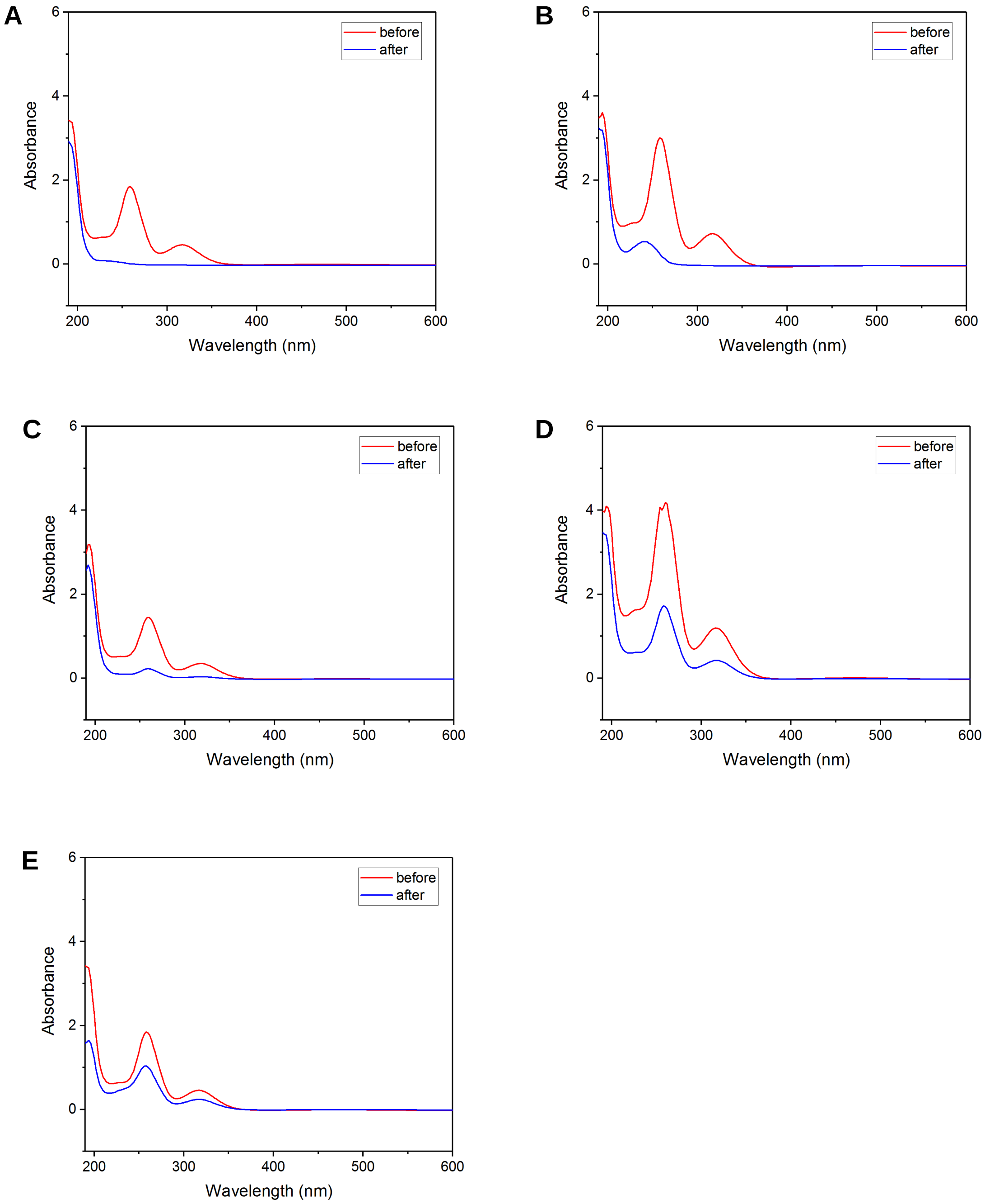

Figure B.3. UV vis spectra of Cp(Pd)allyl in pentane before and after mixing with Ag parent catalysts in the synthesis of (a) $AgPd_{0.5}/TiO_2$, (b) $AgPd_2/TiO_2$, (c) $AgPd_{0.35}/TiO_2$, (d) $AgPd_{0.6}/C$, and (e) $AgPd_{1.3}/SiO_2$. Solutions were diluted and calibration curves were used to calculate the uptake of the Cp(Pd)allyl by the Ag parent catalyst.

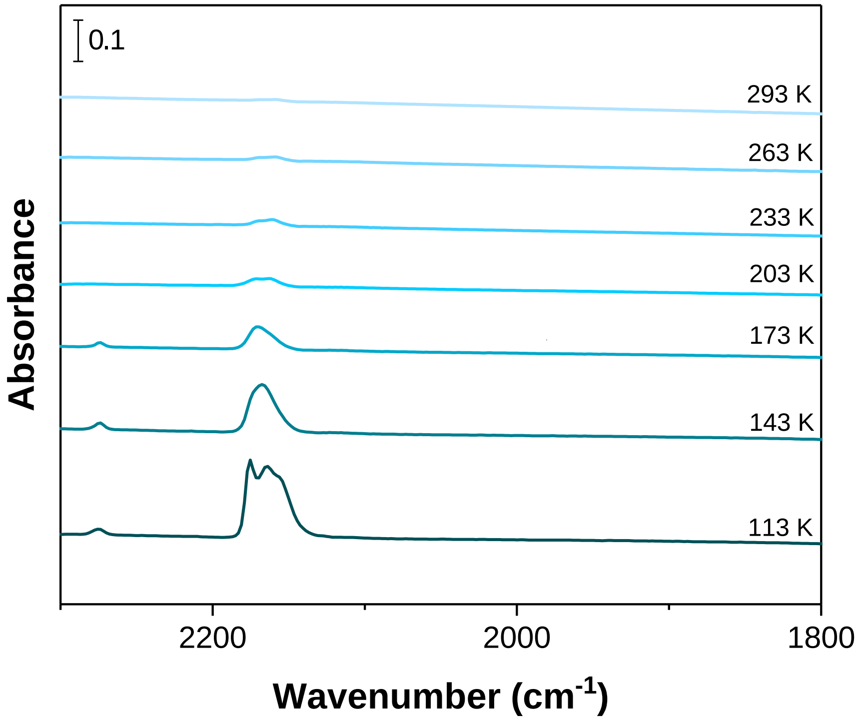

Figure B.4. FTIR spectra of adsorbed CO on Ag/TiO_2. The catalyst was first reduced in H_2 at 473 K then the catalyst was cooled under vacuum to 223 K. 50 Torr of 1% CO was introduced to the catalyst and the sample was then cooled further to 113 K. Spectra were collected as the sample was warmed to room temperature. No adsorbed CO was observed on the Ag, and CO adsorbed on the TiO_2 desorbed by 263 K.

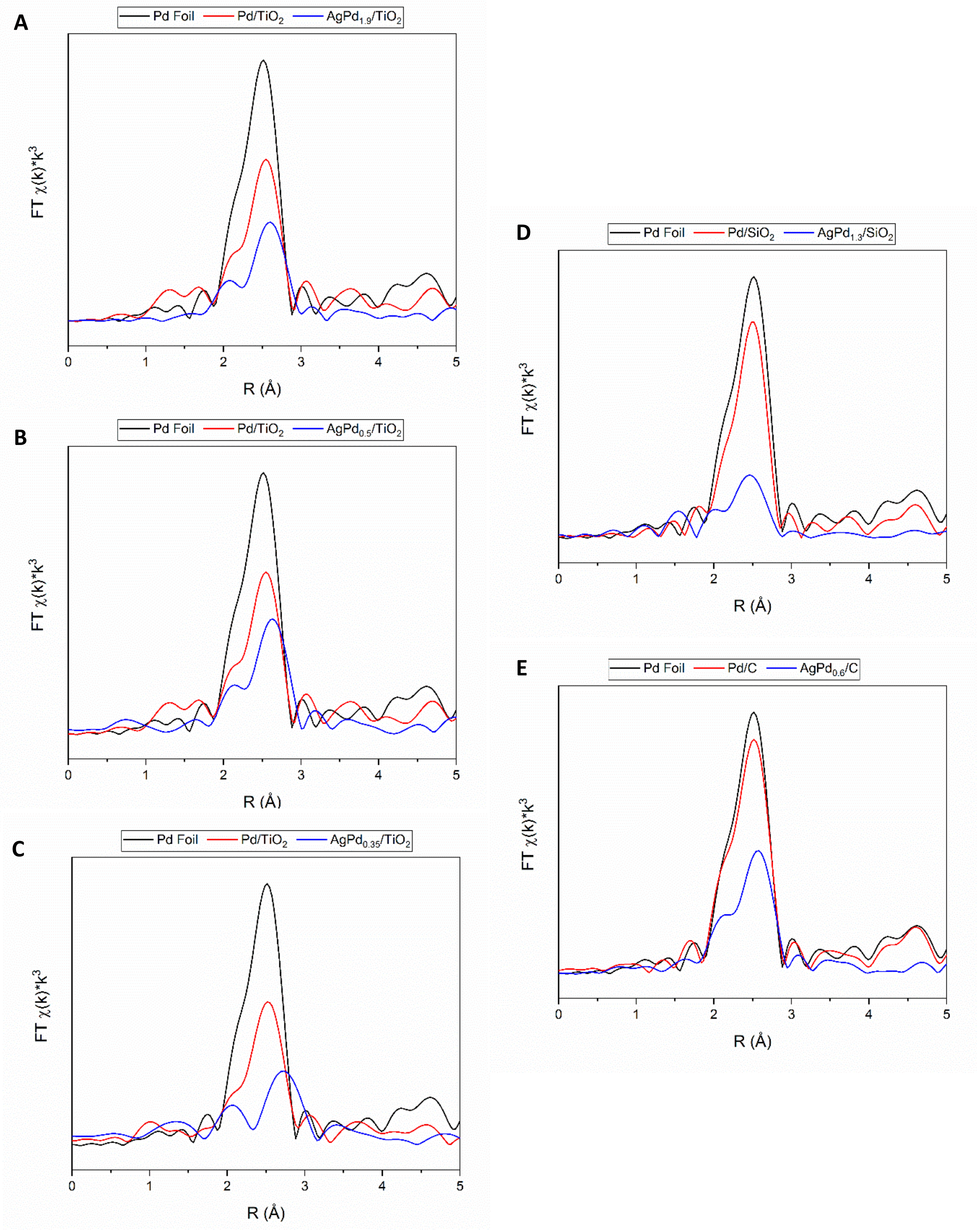

Figure B.5. Fourier transform of the k^3 weighted EXAFS at the Pd-K edge (24350 eV) of (a) $AgPd_{1.9}/TiO_2$, (b) $AgPd_{0.5}/TiO_2$, (c) $AgPd_{0.35}/TiO_2$, (d) $AgPd_{1.3}/SiO_2$, and (e) $AgPd_{0.6}/C$ along with the Pd foil and monometallic Pd catalysts on the corresponding supports. Catalysts were pretreated under H_2 at 473 K and analyzed under inert gas flow, except for $AgPd_{0.35}/TiO_2$ which was analyzed under inert gas without pretreatment.

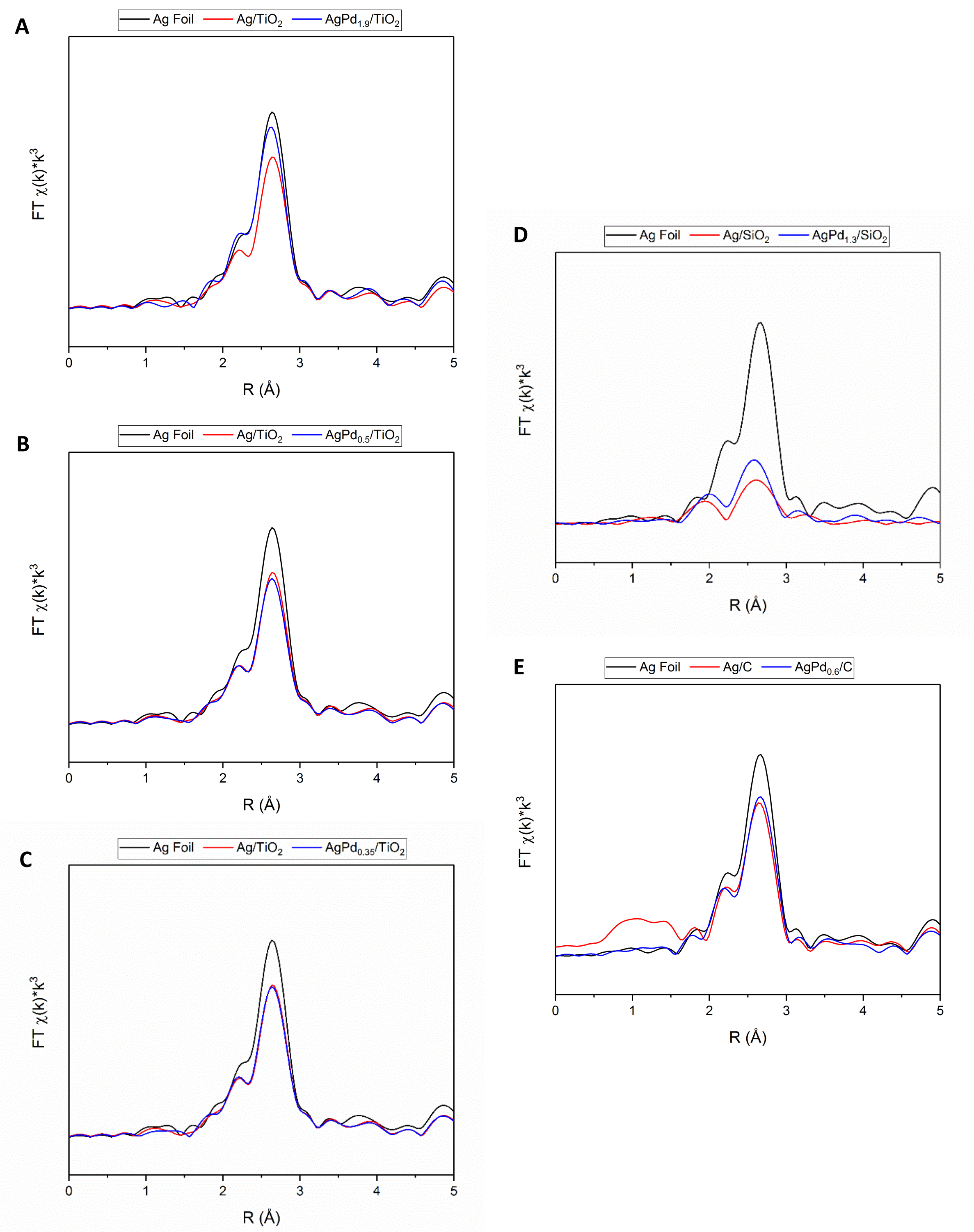

Figure B.6. Fourier transform of the k^3 weighted EXAFS at the Ag-K edge (25514 eV) of (a) AgPd$_{1.9}$/TiO$_2$, (b) AgPd$_{0.5}$/TiO$_2$, (c) AgPd$_{0.35}$/TiO$_2$, (d) AgPd$_{1.3}$/SiO$_2$, and (e) AgPd$_{0.6}$/C along with the Ag foil and monometallic Ag catalysts on the corresponding supports. Catalysts were pretreated under H_2 at 473 K and analyzed under inert gas flow, except for AgPd$_{0.35}$/TiO$_2$ which was analyzed under inert gas without pretreatment.

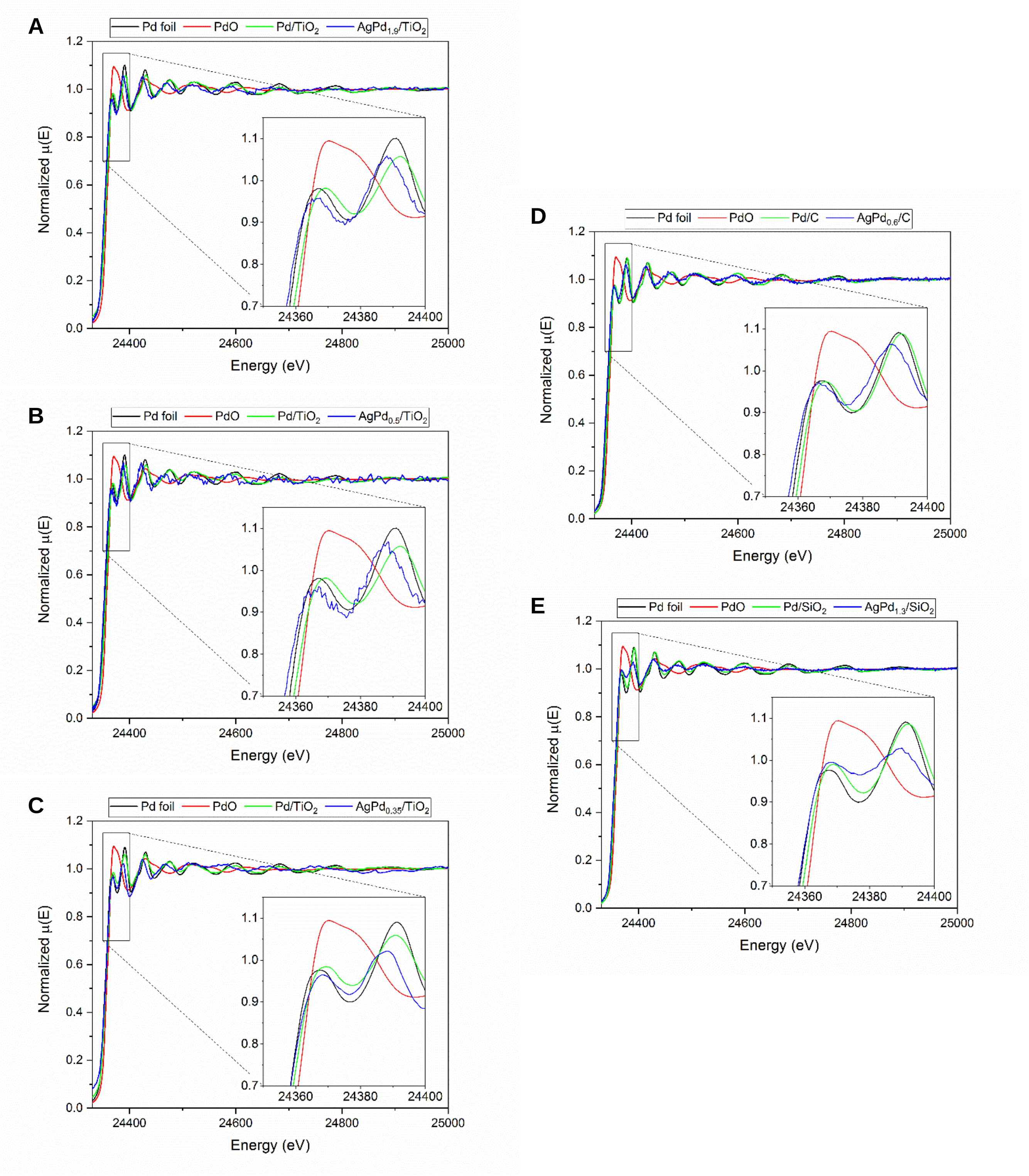

Figure B.7. Normalized Pd-K edge XANES spectra of (a) AgPd$_{1.9}$/TiO$_2$, (b) AgPd$_{0.5}$/TiO$_2$, (c) AgPd$_{0.35}$/TiO$_2$, (d) AgPd$_{1.3}$/SiO$_2$, and (e) AgPd$_{0.6}$/C catalysts pretreated under H$_2$ at 473 K along with the corresponding monometallic Pd catalyst, Pd foil, and PdO standard. The AgPd$_{0.35}$/TiO$_2$ and Pd/TiO$_2$ catalysts with spectra in (c) were not reduced prior to analysis.

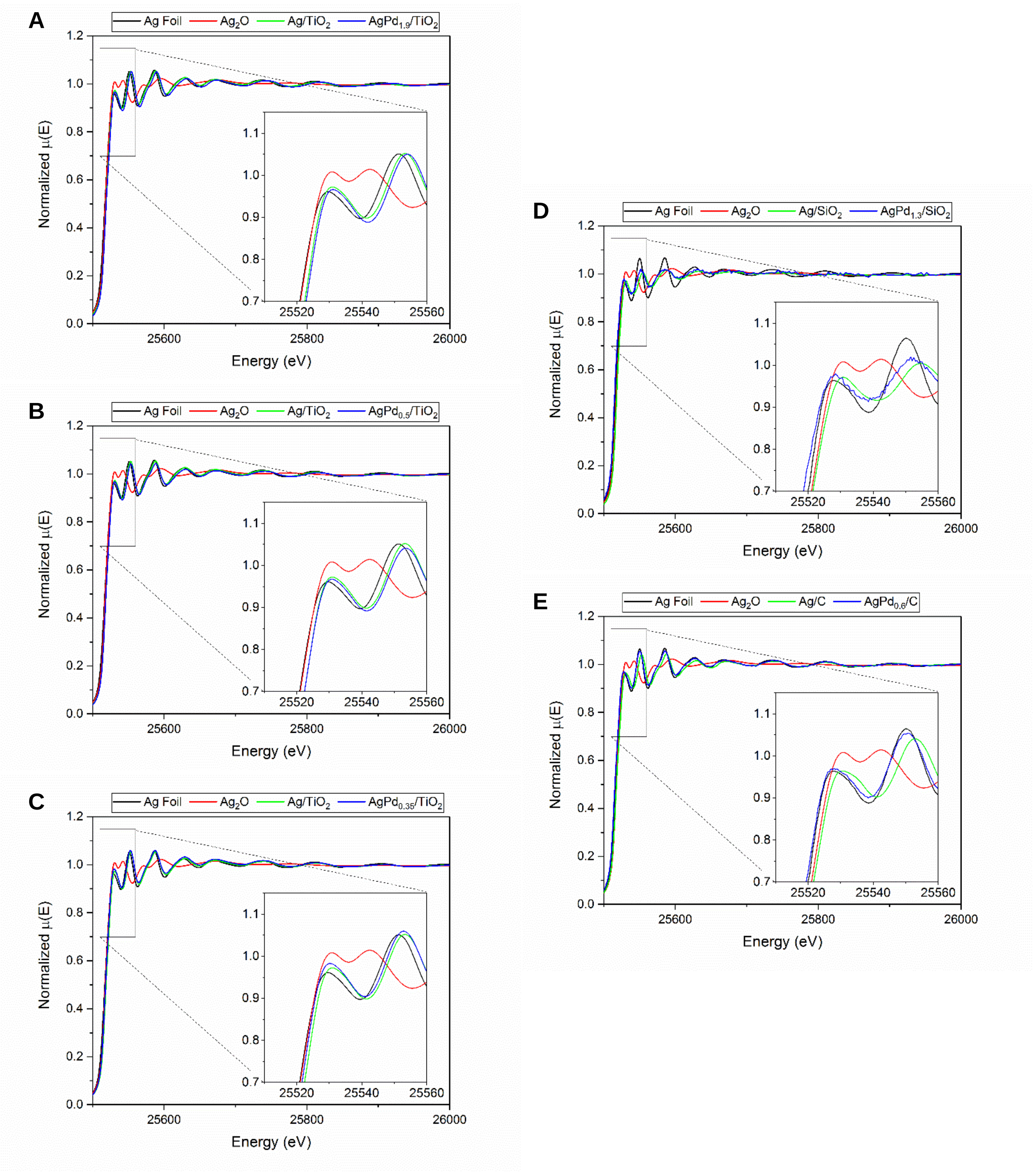

Figure B.8. Normalized Ag-K edge XANES spectra of (a) $AgPd_{1.9}/TiO_2$, (b) $AgPd_{0.5}/TiO_2$, (c) $AgPd_{0.35}/TiO_2$, (d) $AgPd_{1.3}/SiO_2$, and (e) $AgPd_{0.6}/C$ catalysts pretreated under H_2 at 473 K along with the corresponding monometallic Ag catalyst, Ag foil, and Ag_2O standard. The $AgPd_{0.35}/TiO_2$ catalyst was not reduced prior to analysis.

Table B.1. Conversion and selectivity results for Pd and AgPd catalysts for hydrodechlorination of 1,2-dichloroethane Conditions: 443 K, 15 psig, 0.2 Bar H_2, 0.18 Bar 1,2-DCA, total flow rate 36 sccm. All measurements were carried out at a H_2 conversion of <10% and are averaged over 4 hours time on stream.

		Selectivity		
Catalyst	**1,2-DCA Conversion @ 170 °C**	**Ethane**	**Ethylene**	**Chloroethane**
Pd/TiO_2	0.09	66.41	2.47	31.12
$AgPd_{1.9}/TiO_2$	1.25	98.13	1.06	0.81
$AgPd_{0.5}/TiO_2$	1.92	10.17	89.64	0.18
$AgPd_{0.35}/TiO_2$	0.21	1.95	97.32	0.73
Pd/SiO_2	0.08	69.88	0.7	29.42
$AgPd_{1.3}/SiO_2$	0.33	90.92	0.02	9.06
Pd/C	0.12	86.33	3.81	9.86
$AgPd_{0.6}/C$	0.05	17.97	82.03	0

Table B.2. Turnover frequency and rates for consumption of 1,2-dichloroethane and production of ethane and ethylene. Conditions: 443 K, 15 psig, 0.2 Bar H_2, 0.18 Bar 1,2-DCA, total flow rate 36 sccm. All measurements were carried out at a H_2 conversion of <10% and are averaged over 4 hours time on stream.

	TOF (1/ks)			Rate (umol/g-Pd/s)			
Catalyst	**1,2-DCE**	**Ethane**	**Ethylene**	**1,2-DCE**	**Ethane**	**Ethylene**	**Total Product**
Pd/TiO_2	15.90	10.50	0.39	16.10	10.70	0.40	11.10
$AgPd_{1.9}/TiO_2$	17.80	17.47	0.19	20.57	20.19	0.22	20.41
$AgPd_{0.5}/TiO_2$	34.99	3.57	31.35	56.87	5.81	50.96	56.77
$AgPd_{0.35}/TiO_2$	276.23	5.38	268.83	28.29	0.55	27.54	28.09
Pd/SiO_2	20.90	14.60	0.14	12.96	9.05	0.09	9.14
$AgPd_{1.3}/SiO_2$	13.97	12.70	0.00	35.83	32.58	0.01	32.58
Pd/C	19.01	16.41	0.73	5.81	5.01	0.22	5.23
$AgPd_{0.6}/C$	19.40	3.49	15.90	16.80	3.02	13.78	16.80

Heat and mass transfer calculations

The absence of mass and heat transfer gradients during the reaction testing were assessed by calculation. To assess isothermal operation, Mears' criterion[1] for the worst case of significant wall heat transfer resistance was evaluated at typical feed (15% v/v), conversion (<5%), and selectivity (~90%) conditions. The absence of heat transfer resistance is validated for the following inequality:

$$1 < \left\{ \frac{1.6 k_{re} R T_w^2}{\Delta H_{rxn} \frac{r_{obs}}{(1 + w_i)} \rho_b D_i^2 E_{app} \left(1 + \frac{8 k_{re}}{D_i h_w}\right)} = 3.08 \right\}$$

For the evaluation of these catalysts, the following parameters were estimated and used from correlation, yielding the final test results:

Effective radial thermal conductivity, k_{re} = 0.0002654 cal/cm-s-K

University gas constant, R = 1.987 cal/mol-K

Temperature of the reactor wall, T_w = 190°C

Heat of reaction, ΔH_{rxn} = -27.7 kcal/mol for 90% selectivity to ethylene

Observed rate, r_{obs} = 1.3e-6 mol/gcat-s

Ratio of dilution mass to catalyst mass in bed, w_i = 0.5

Apparent catalyst bed bulk density, ρ_b = 0.97 g/cm^3

Reactor internal diameter, D_i = 0.4 cm

Apparent activation energy, E_{app} = 15.0 kcal/mol

Wall heat transfer coefficient, h_w = 0.068 cal/cm^2-s-K

The absence of external mass transfer gradient was validated using the standard Chilton-Colburn j_D factor for packed beds (for this work a calculated mass transfer coefficient of 183 cm/s was obtained), while internal mass transfer gradients was similarly evaluated and satisfied using Weisz-Prater criterion:

$$0.3 > \left\{ \frac{r_{obs} \frac{\rho_b}{(1 - e)} L^2}{C_s D_{eff}} \right\} = 0.0003$$

Bed void fraction, e = 0.4

Surface concentration of EDC, C_s = 5.3e-6 mol/cm^3

Effective diffusivity, D_{eff} = 0.001 cm^2/s

Characteristic catalyst particle length equal to geometric volume divided by surface area, L = 8.3e-4 cm

Appendix C. Supplemental Information for Chapter 5

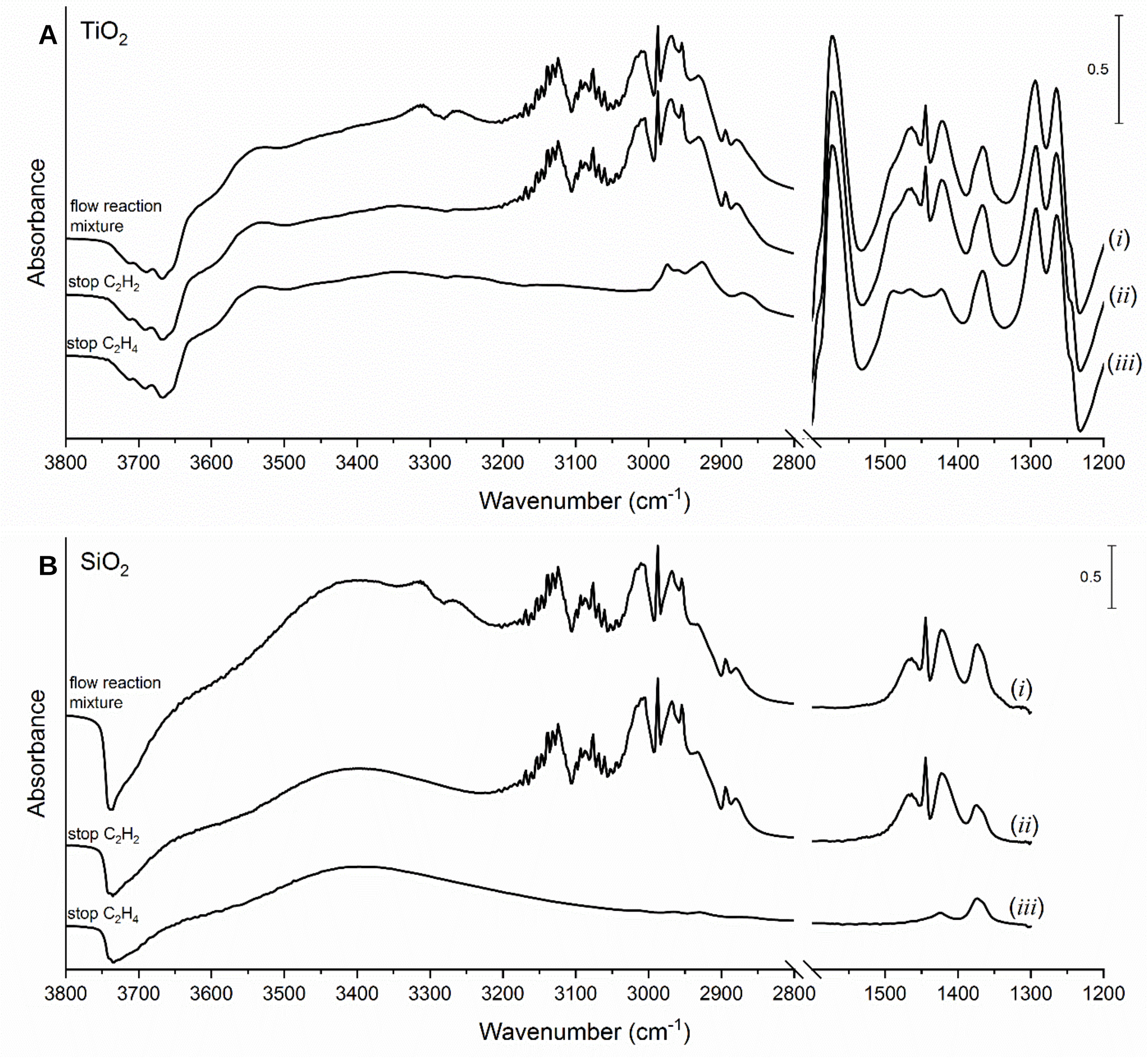

Figure C.1. FTIR spectra of TiO_2 (A) and SiO_2 (B) at 313 K under (i) the dilute reaction mixture (0.083 bar C_2H_4, 0.003 bar C_2H_2, 0.083 bar H_2, balance Ar) (ii) after the removal of C_2H_2 from the reaction mixture, and (iii) after removal of C_2H_2 and C_2H_4 from the reaction mixture. The catalysts were reduced for 2 h at 473 K under H_2 prior to exposure to reaction gases. Spectra have been normalized by the catalyst pellet areal density.

References

(1) Mears, D. *J. Catal.* **1971**, *20*, 127–131.